Novel Miniaturized Tunable Filters with Optical Control

Paul Leshauris

Thèse de doctorat

UNIVERSITE DE LIMOGES

ECOLE DOCTORALE N°521

Sciences et Ingénierie pour l'information

Laboratoire Xlim, Faculté des Sciences et Techniques de Limoges

Thèse

pour obtenir le grade de

DOCTEUR DE L'UNIVERSITÉ DE LIMOGES

Discipline / Spécialité : Electronique des hautes fréquences,

Optoélectronique et Photonique

présentée et soutenue par

Paul LESHAURIS

Le 27 octobre 2016

[Novel Miniaturized Tunable Filters With Optical Control]

Thèse dirigée par Nicolas DELHOTE, Langis ROY, Serge VERDEYME

JURY :

Président du jury

M. Bernard Jarry, Professeur, Laboratoire Xlim, Université de Limoges

Rapporteurs

M. Cédric Quendo, Professeur, Lab-STICC, Université de Bretagne Occidentale

Mme. Valérie Vigneras, Professeur, Laboratoire IMS, Bordeaux INP

Examinateurs

M. Langis Roy, Professeur, Département d'Electronique, Université de Carleton

M. Steven McGarry, Professeur, Département d'Electronique, Université de Carleton

M. Jim Wight, Professeur, Département d'Electronique, Université de Carleton

M. Thierry Monédière, Professeur, Laboratoire Xlim, Université de Limoges

M. Nicolas Delhote, Maître de Conférences, Laboratoire Xlim, Université de Limoges

Invité

M. Serge Verdeyme, Professeur, Laboratoire Xlim, Université de Limoges

Université de Limoges

« La science donne à celui qui y consacre son travail et ses recherches beaucoup de satisfaction, à celui qui en apprend les résultats, fort peu. Mais comme peu à peu toutes les vérités importantes de la science deviennent ordinaires et communes, même ce peu de satisfaction cesse d'exister : de même que nous avons depuis longtemps cessé de prendre plaisir à connaître l'admirable Deux fois deux font quatre. Or, si la science procure par elle-même toujours de moins en moins de plaisir, et en ôte toujours de plus en plus, en rendant suspects la métaphysique, la religion et l'art consolateurs : il en résulte que se tarit cette grande source du plaisir, à laquelle l'homme doit presque toute son humanité. C'est pourquoi une culture supérieure doit donner à l'homme un cerveau double, quelque chose comme deux compartiments du cerveau, pour sentir, d'un côté, la science, de l'autre, ce qui n'est pas la science : existant côte à côte, sans confusion, séparables, étanches : c'est là une condition de santé. Dans un domaine est la source de force, dans l'autre le régulateur : les illusions, les préjugés, les passions doivent servir à échauffer, l'aide de la science qui connaît doit servir à éviter les conséquences mauvaises et dangereuses d'une surexcitation. — Si l'on ne satisfait point à cette condition de la culture supérieure, on peut prédire presque avec certitude le cours ultérieur de l'évolution humaine : l'intérêt pris à la vérité cessera à mesure qu'elle garantira moins de plaisir ; l'illusion, l'erreur, la fantaisie, reconquerront pas à pas, parce qu'il s'y attache du plaisir, leur territoire auparavant occupé : la ruine des sciences, la rechute dans la barbarie est la conséquence prochaine ; de nouveau l'humanité devra recommencer à tisser sa toile, après l'avoir, comme Pénélope, détruite pendant la nuit. Mais qui nous est garant qu'elle en retrouvera toujours la force ? »

Friedrich Nietzsche

« Hâte-toi lentement »

Aknowledgements

Tout d'abord, je tiens à remercier mes encadrants, Nicolas Delhote (Maître de Conférences à l'Université de Limoges), Langis Roy (Professeur à l'Institut Technologique de l'Université de l'Ontario) et Steven McGarry (Maître de Conférences au Département Electronique de l'Université de Carleton) pour leurs judicieux conseils, leur gentillesse ainsi que leur soutien durant ces années de thèse. Merci de m'avoir fait confiance dans cette aventure exceptionnelle qui m'a permis de découvrir une autre culture, un autre pays et de progresser sur un plan scientifique et humain.

Je remercie également Madame Valérie Vigneras (Professeur au laboratoire IMS de Bordeaux) et Monsieur Cédric Quendo (Professeur au Lab-STICC en Bretagne) d'avoir accepté aimablement d'être mes rapporteurs et pour leur intérêt porté à mes travaux.

Je remercie aussi mes collègues du laboratoire Xlim de Limoges pour leur soutien et toutes les connaissances qu'ils ont pu me transmettre : Aurélien Périgaud, Oliver Tantot ainsi que tous les membres de l'équipe MACAO. Merci aussi à Damien Passerieux pour son expertise, sa disponibilité et pour toutes les mesures faites au sein du laboratoire Xlim. Merci aussi à Marie-Laure Guillat et Marie-Claude Lerouge pour leur gentillesse et leur aide précieuse.

I would like to thank the members of department of Electronic of Carleton University. Thanks, Blazenka, Sylvie and Anna for all the help that you gave me during my Canadian experience. I also thank Nagui for his kindness, availability and his advices. A special thanks for Behzad for his knowledges and his friendship, for my personal Moroccan teacher Aziz who welcomed me like a brother, Shicheng, Nathan and Rob. I would like to thank as well Professor Jim Wight who reviewed my thesis for Carleton University.

Cette thèse a pu se faire grâce à l'immense et constant soutien de mes parents, Marc et Patricia, de mon frère Germain (et sa petite famille : Marie-Line, Adam et Alix) et de ma famille. Ils m'ont encouragé et soutenu dans les moments difficiles. Je leur dois en partie la réussite de ma thèse.

Je remercie aussi mes proches amis limougeauds : Nico, Yoann, Arnaud, Karthik, Etienne Johann, Samuel, Carlos, Emilien (président de SigmadocX), Philou, Titou, Khalil, Christophe, Clément, Aymen, Ahmad. Une pensée aussi à mes belles rencontres canadiennes : Pierre, Anthony, Josée, Mireille, Thomas, Yvonne, Clélia et Alexandra.

Bien sûr je n'oublie pas le Gang : Alex, NikX, Kara, Mathias, Nanardogg, Laura, Le Coach, Antoine H., Antoine L., Antoine G. (et son pied gauche), Julie, Cidou, la vie, GaetGaet, Charlotte, Damien, Emilie, le Squash, Thomas H, Geo, Anaïs et Alex C., Luc, Simon le fils, Malou et les bretons de « Malades ». Aux autres de Louis Pons : Quentin et Thomas A. ainsi que Coercition (groupe mythique) : Toinou, Clément et Noël (Maître Coulaud).

Droits d’auteurs

List of figures

Introduction----------

Chapter 1----------

Chapter 2----------

Chapter 3----------

Chapter 4----------

General introduction

Telecommunications systems have increased their complexity with the emergence of microwave devices operating at multiple frequency bands and standards. Therefore, the circuits carrying out the same purpose but at different frequencies bring about a growth of the size of the whole communication system. To avoid this issue, many researchers have demonstrated over the last decade the importance of tunable circuits, especially those involving passive elements such as filters or antennas which occupy most of the space in a telecommunication chain.

Tunability in microwave presents enormous advantages such as: component count reduction in multi-standard systems, and thus reduction of cost, weight and power consumption; in-situ adjustment of systems in order to compensate for fabrication errors; adaptability of terminals to new standards or to the instantaneous number of users; addition of new features to terminals; etc. Reconfiguring an electronic component consists in modifying its behavior by an external action. It may involve the variation of operating frequency, bandwidth, radiation pattern, etc. Current tunable methods are often based on the use of electric or magnetic source(s) applied to semiconductor or MEMS components, liquid crystal, ferroelectric or ferromagnetic materials, involving the integration of the actuation system (routing parts, magnet…) close to the main elements. One interesting investigation that has potential to increase the performance-to-cost ratio is the optical control of reconfigurable components. Here, an optically sensitive material (i.e. whose dielectric constant varies with light) may be applied to certain areas of the microwave component to achieve *direct optical control*; or alternatively, an optically controlled device (i.e. photosensitive diode or switch) may be inserted into the structure of the microwave component to achieve reconfigurability via *indirect optical control*. Such a solution potentially simplifies the design, the realization and the complexity of tunable RF devices, because the control signal (optical) is uncorrelated with the information signal (electromagnetic), removing the need for disruptive DC bias circuits in the RF part. The optical feeding could even be delocalized from the RF part, since no contact may be needed.

The goal of this thesis is to develop a system interesting in terms of implementation of highly miniaturized but with high performance tuning devices. A possible way to achieve this result is depicted in Figure 1. The idea is to create a generic and flexible platform with an original stackable (“Lego” like) technique for indirect optical control. The different parts of

the reconfigurable component can be plugged together allowing complete packaging of the structure. The main difference with the now well-established, multilayer approach is that the different levels in this figure correspond to a separate function which can be designed independently, thereby facilitating the design of the whole module. The specific function of each level shown in Figure 1 is:

- Level 1 consists of the core RF part (resonator or filter) implemented in an SIW regime.
- Level 2 contains all the optically switchable tuning elements, i.e. optically controlled RF switches connected to SMT capacitance banks.
- Level 3 includes the appropriately positioned optical fibers which carry the optical control signal to the optically reconfigurable elements.

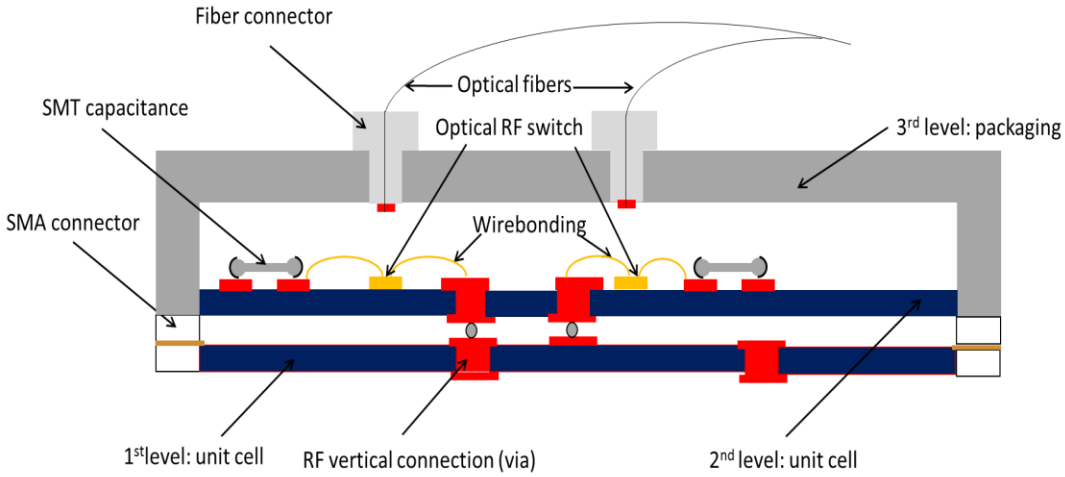

Figure 1: 3D assembly of the different parts of the optically reconfigurable components using indirect optical control

The chapter 1 of this thesis illustrates the main features of a filter/resonator, the need of tunability and the current technologies used to make a passive microwave component such as an antenna or tunable filter thanks to varactor diodes, ferroelectric and ferromagnetic materials, Micro Electro Mechanical Systems (MEMS) or with a Microfluidic method. Some characteristics of these tunability methods will be give, as well as their advantages and disadvantages.

The chapter 2 is focused on the elementary cell (level 1 from Figure 1) based on Substrate Integrated Waveguide technology. Given the SIW's technology integrability with planar structures, this technology lends itself well to the development of "system-on--package" solutions involving layered integration of other device technologies (i.e., semiconductor, MEMS, optical, …) as it may be required to achieve tunability. Therefore, after reviewing the current methods to tune microwave filters and antennas, a SIW resonator based on a metamaterial effect is investigated to reach high performance with a good compactness.

To fulfill the purpose of the level 1, another elementary cell is studied in the chapter 3 but based on another technology namely the loaded cavity effect. This structure is made with Stereolithography process with Alumina material in order to obtain a low resolution for manufacturing high microwave performance structure with a good compactness. In this chapter, the principle of cavity and loaded effect are explained as well as the understanding for the novel tunable resonator thus created. On top of that a comparison between the structures from the chapter 2 and 3 is made with others from literature. Some perspectives are depicted based on the investigated elementary cell for higher order filters.

After explaining the role of the developed resonators, chapter 4 focuses on direct and indirect optical control. A zero-bias optically controlled RF switch based on a standard CMOS technology is designed and measured. Moreover, an enhancement of its intrinsic performance is investigated. A new whole structure, which combines a resonator from the chapter 3 and the indirect optically tunable method, is investigated to create a novel miniaturized tunable filter with optical control.

The thesis ends with the general conclusions and perspectives of this work.

Chapter 1:

Tunable filters

1.1 Introduction

In recent years, a great effort has been performed in electronically tunable microwave components for wireless front-end applications such as antennas, oscillators, phase shifters and bandpass or bandstop filters. Indeed, the electromagnetic environment has become very dense in terms of applications and frequency bands and that is why frequency agility and narrow operating bandwidth are becoming highly required for different components in RF front-ends. On the other hand, tunable wideband microwave devices are essential in military applications and long distance communications [1] for electronic support measuring receivers. Great developments in filters were made during the World War II and the invention of the radar as well as improvements on tunable narrow-band filters. Electronically tunable devices are found in scanning receivers for instance and are commonly used in microwave test equipment as well.

Nowadays, a trend in microwave systems is to create communication systems which are adaptable and dynamically reconfigurable such as cognitive radio (a radio that accordingly changes its transmission or reception parameters) which provides immunity to jamming, narrow-band interferers and multi path finding.

The use of wireless devices has increased considerably over the last decade and therefore has caused a need for more efficiency devices with more and more functionalities. The main features for wireless devices are the reliability, a good power efficiency, a low cost fabrication and it has to be compatible with different communications protocol and capable of operating over a wide frequency range. Besides, the development of low cost and miniaturized tunable circuits with high performances is fundamental to enable the integration of those devices in wireless systems which tend to be more and more compact.

Most of the wireless communication systems used in cellular, radar, GPS and so on are made up of tunable RF circuits. The latter play a crucial role in determining the sensitivity, size, power consumption and overall signal quality of mobile wireless devices. This is why tunable circuits are designed to respond optimally when functioning at a specific frequency, power level or impedance. Moreover, the tunable circuits can be adjusted to function optimally as conditions change (they do not remain constant and could be very changeable

depending on the location). The result may be saving in costs, improved battery life, better performance and reduction in size.

There are for example different cell phone standards where the frequencies are different from each other. On top of that these standards differ depending on the country of use. It is also desirable for a modern mobile device to adapt itself to geographic boundaries to the communication protocols and different standards such as WAN, WLAN networks, Bluetooth and so on. At the same time, the buyers want all these functionalities with an interesting cost and great performances. A number of such devices have appeared on the market with tri-band or quad-band handhelds that incorporate multiple cellular modes as well as Wi-Fi or/and Bluetooth. For each band, a circuit is designed which implies an increase of the size, weight and cost. In opposition, a tunable circuit can perform the function of several parallel circuits with a simple change of the useful frequency thanks to a tunability technology. The Figure 1 illustrates this situation for the case of duplexers in a tri-band system where a single tunable duplexer can replace three fixed duplexers

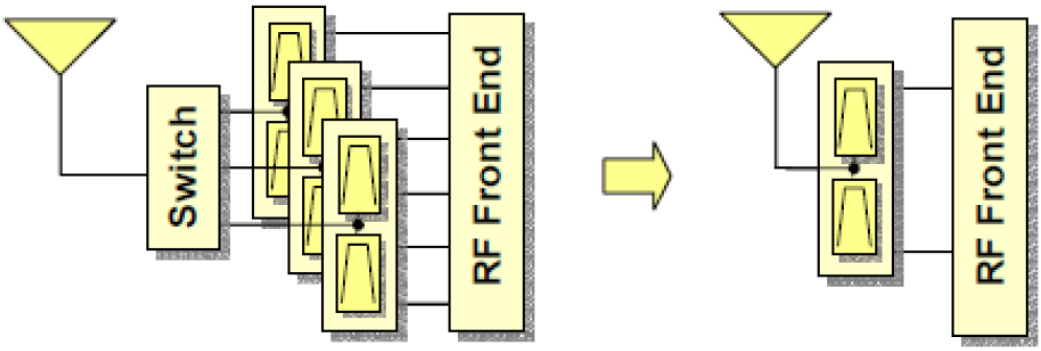

Figure 1 : Tri-band system with three fixed duplexers and with a single tunable duplexer

A receiver or a transmitter is made of different devices as illustrated in by a satellite front-end receiver Figure 2. This reception chain is composed of an antenna followed by an RF filter and a low noise amplifier (LNA). The useful signal is filtered again and amplified at RF frequencies. Then this signal is down converted by a mixer connected to local oscillator and filtered again by an IF filter. The last steps of the chain are an IF amplification and an analog to digital conversion. Most of these elements can be tunable to operate at different frequencies.

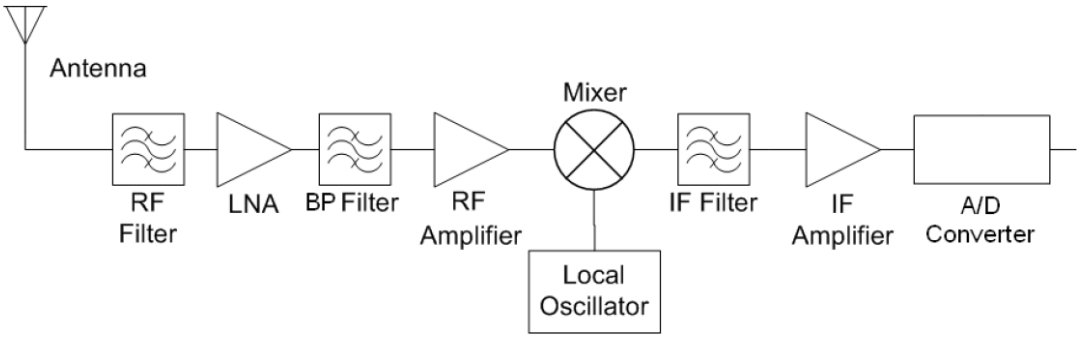

Figure 2 : Satellite front-end receiver block diagram

This thesis is focused on filters and more particularly on bandpass filters (BPF).

Tunable filters are essential components for multifunctional radio frequency systems. The need for such components has been increased over the years in order to provide good solutions with the lowest possible cost for frequency agile circuits and particularly for wireless applications. Indeed, tunable filters are useful for covering multiple frequency bands by using a single element of front-end hardware. It is essentially to grant the multiple bandwidths and frequencies to fulfil several requirements in a short time period.

The tunability of filtering devices shows the ability of a filter to change its frequency and/or bandwidth thanks to an external control. In some cases, they can adapt themselves to operate in a changing environment. Beyond the frequency changing, the main issue of those filters is the control of the different couplings for each state of the filter. The tunability can be then continuous or discrete depending on the technology used.

1.2 Parameters of a filter

Physical parameters have to be taken into account during the design of a filter to optimize the integration in a global system as well as the integration with the environment. The main features are the weight, the size, the cost, the consumption and so on.

Electrical parameters are useful to set the specifications of a filter:

- The centre frequency f_0
- The bandwidth (BW)

- Tuning range
- Ripple
- Spurious
- Return loss
- Unloaded quality factor of a single resonator
- Insertion loss
- Linearity

Several types of losses exist in a given microwave resonator: the radiation loss, the metallic loss, external loss and the dielectric loss.

The radiation losses P_{rad} are created by the EM field inside such environment. However, those leakages can be prevented thanks to a metallic shield. Thus, the field is restricted and therefore cancels this type of loss.

The metallic part of a resonator (the resonator itself and/or its housing) has a finite conductivity σ and therefore the field is not totally reflected but absorbed by the electrical wall and produces heating losses which degrade the quality factor Q. This type of loss is called metallic loss P_m. For a resonant device the heating could expand through the metallic wall and as a consequence could shift the resonant frequency. This phenomenon is from the interaction with the magnetic field H and those walls.

The external losses P_{ext} are created by the access couplings. Indeed, the cavity is partially opened in order to set the field inside. This is why it is important to design apertures such as coaxial accesses, iris or waveguide to induce a coupling with the field in the cavity. Access couplings are critical because the RF response (for a filter) is directly related to those.

The dielectric losses P_{diel} are defined by the loss tangent of the dielectric material which is the quantification of the interaction between the electric field and the said material. Lower the loss tangent, better the quality factor.

The total losses are the addition of the previous ones:

$$P_{tot}=P_{rad}+P_m+P_{ext}+P_{diel} \quad (1)$$

By definition, the quality factor is given by:

$$Q_i = 2\pi \frac{Energy\ Stored}{Energy\ dissipated\ per\ cycle} = 2\pi \frac{W_i}{P_i} \qquad (2)$$

For a structure with an input and output coupling, the total quality factor is the following:

$$\frac{1}{Q_l} = \frac{1}{Q_m} + \frac{1}{Q_{diel}} + \frac{1}{Q_{rad}} + \frac{1}{Q_{extI}} + \frac{1}{Q_{extO}} \qquad (3) \quad , \qquad \frac{1}{Q_0} = \frac{1}{Q_m} + \frac{1}{Q_{diel}} + \frac{1}{Q_{rad}} \qquad (4)$$

The total quality factor also known as the loaded quality factor is limited by the smallest quality coefficients namely Q_m, Q_{diel} and Q_{rad}. The latter define the unloaded quality factor Q_0 which is one of the most important criteria during the design of a filter. Indeed, this one is related to the losses and to the selectivity of the filter. Higher Q_0 (4), higher the selectivity. The value of this factor depends on the technology used. However, only costly technologies can reach very high quality factor; so, a trade-off has to be made. The Figure 3 illustrates the typical value of Q according to the technology used.

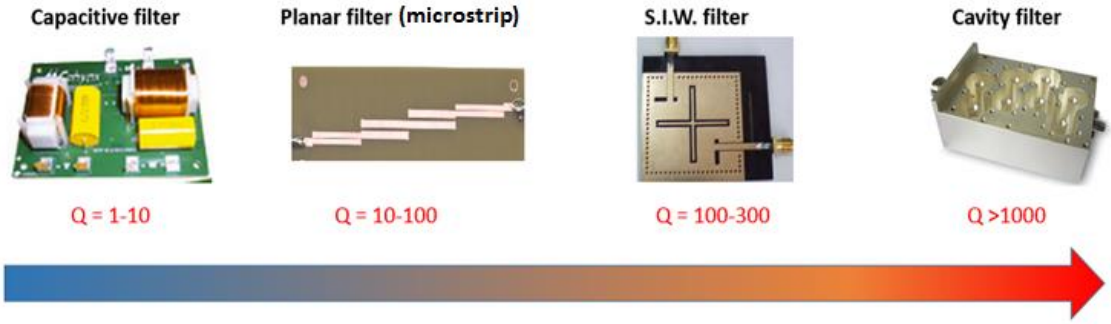

Figure 3 : Evolution of the quality factor dependings on the technology used

Throughout this thesis the quality factor of a filter will be an essential parameter to optimize filter itself as well as the tunability methods. The next part introduces the main technologies which provide a good tuning range for RF filters while keeping them compact for the S and L frequency bands.

1.3 Technology and Tunability

Reducing the costs, the complexity and the foot print for Microwave/RF components are the main challenges for researchers without downgrading the overall performances. Therefore, tunable components, systems and subsystems are mainly investigated to overcome these challenges and increase functionality.

In many situations, due to high sensitivity of the microwave structures a post fabrication tuning of the fabricated device is needed to reduce the difference between the device's operating frequency and the desired one. Moreover tunable structures offer a better isolation than multiple frequency devices which are more sensitive to the crosstalk from neighboring bands. So there are three main reasons why tuning of microwave components could be useful:

- More standards/services can be covered by the same devices
- Post fabrication fine-tuning of the devices becomes possible
- Better isolation can be achieved while covering more bands

In the following sections a review of different tuning technologies is made for passive device components and particularly for filters.

Tunable components can be designed using different types of technologies such micro-electromechanical system (MEMS), solid state varactor diode, ferroelectric material, liquid crystal and many others.

1.3.1 Micro Electro Mechanical systems (MEMS)

MEMS encompasses several distinct types of devices including RF switches, delays, resonators, varactors and inductors. This technology is now widespread because of a wide range of applications for example all type of wireless communications, radar, satellites, military radio and so on. This technology offers significant benefits compared to conventional RF components, including lower power consumption, lower insertion loss and smaller form factor. As a consequence, this technology has become quite popular over the last decade and for RF switch based tunable systems.

MEMS technology is a combination of micromachining and IC technology. This technology allows the fabrication of mechanical structures with very small dimensions. MEMS devices used in RF applications are also known as RF MEMS. As semi-conductor technologies offer the advantages of low power consumption (near zero), low insertion loss and high isolation. Aside from offering a good integration and miniaturization potential, the RF MEMS devices are interesting to provide reconfigurability and tunability for multi-band and multi-standard operations. Even though the resistance of the ON state is low, this technology is very costly and the related design to implement such components could be more complex.

However, the RF MEMS technology offers a range of variable components such as variable capacitor [2][3], variable inductor [4] and switch [5][6].

1.3.1.1 Tunable RF planar filters with MEMS

A lot of systems can change the value of the capacitance (discrete or continuous) and modify the couplings within the filter thanks to the ON state or OFF state given by such components as MEMS switches or varactors (this technology will be discussed in the next part).

The filter in [7] shows a two poles band-pass filter at 5 GHz with a tuning range of 9% and a constant bandwidth thanks to a control of inter resonator coupling provided (changing of 8%) by MEMS (Figure 4). A same type of filter [8] with U shape resonators whose the electrical coupling changes by the action of MEMS provides a constant bandwidth of 65 MHz from 0.69 GHz to 1.13 GHz.

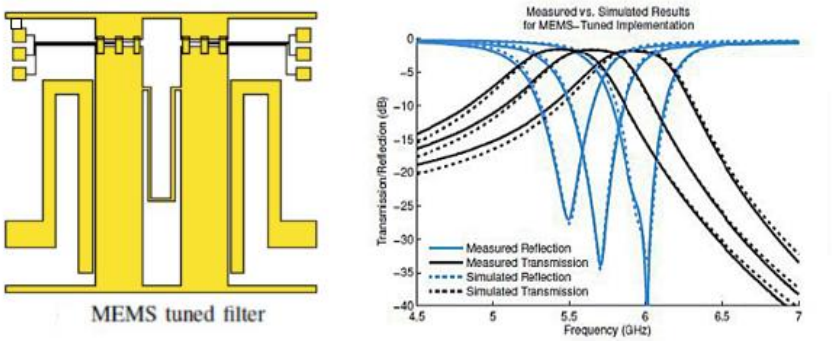

Figure 4 : MEMS tuned filter and its parameter S [7]

In [9] a four pole bandstop filter based on the combination of the split ring resonators (SRRs) and RF MEMS switches for X frequency band is shown. A microstrip line loaded with four pairs of SRRs enable to exhibit four different resonance frequencies. By adding two capacitive ON/OFF switches and a numerical command the frequency response can change by activating or not each SRR independently (Figure 5).

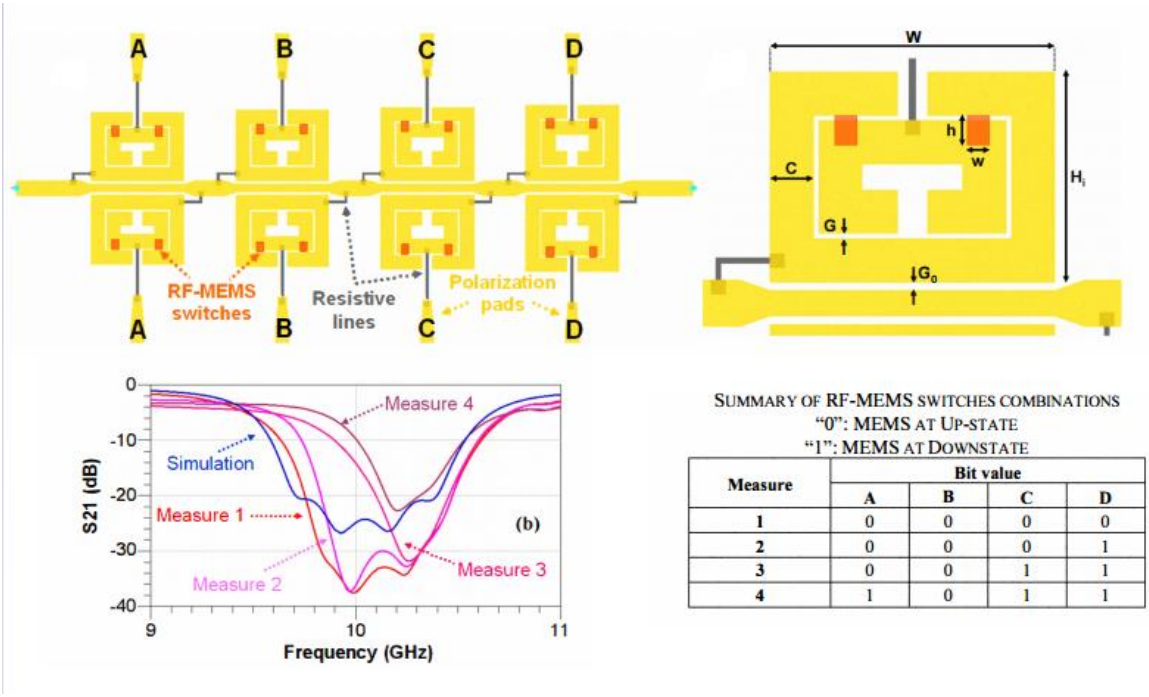

SUMMARY OF RF-MEMS SWITCHES COMBINATIONS
"0": MEMS AT UP-STATE
"1": MEMS AT DOWNSTATE

Measure	Bit value			
	A	B	C	D
1	0	0	0	0
2	0	0	0	1
3	0	0	1	1
4	1	0	1	1

Figure 5 : Four pole bandstop filter based on RF-MEMS-loaded Split Ring Resonators [10]

Other examples of RF-MEMS tunable filters in which the value of continuous capacitance change can be found in [11][12].

The previous articles are related to tunable RF planar filters but MEMS are also applied for filters with higher Q.

1.3.1.2 High Q filters using MEMS

Metallic cavity, dielectric resonators or evanescent cavity are widely used for designing high Q filters. The following examples will introduce some high Q tunable filters with MEMS technology.

The system in [13] is a evanescent tunable combline passband filter based on electronic tuning using RF MEMS capacitor bank. This structure consists of combline resonators with capacitive loading (Figure 6). As a result, the center frequency can change by using RF-MEMS switched capacitor banks which are assembled on the top of the lid. The MEMS switches are turned on and off in a way that the two capacitor banks have the same capacitance value and the two resonators are tuned synchronously. The two pole bandpass filter has an f_0 at 2.5 GHz with a bandwidth of 22 MHz and tuning range of 110 MHz. The quality factor is from 1300 to 374 over the tuning range.

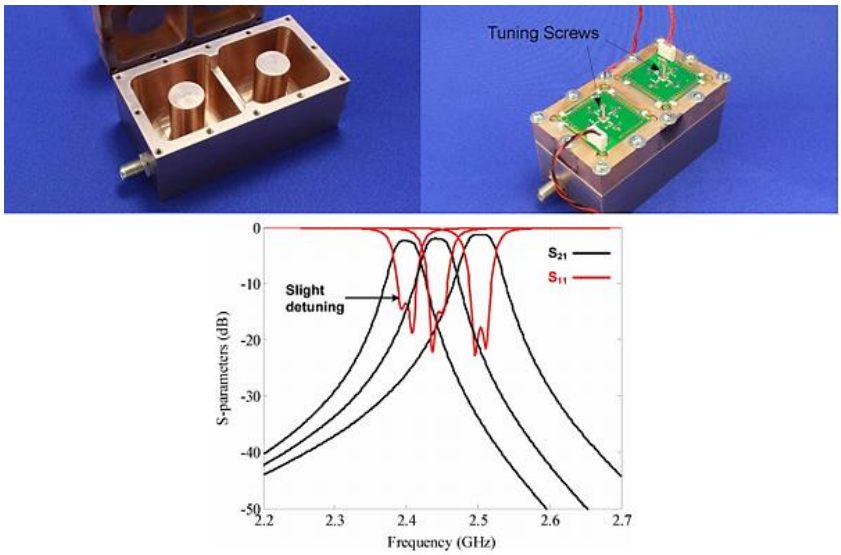

Figure 6 : Two pole bandpasse filter loaded by switched capacitive bank [13]

The next filter [14] is based on evanescent mode cavity and two 4-bit RF MEMS capacitance networks, placed on the metal posts inside an evanescent-mode cavity (Figure 7). This network is mounted on a quartz substrate (due to its low dielectric loss compared to the glass one) which is placed close to a capacitive post. So, the MEMS capacitance network can add a capacitive effect and as a result change the resonant frequency of the filter.

This filter has a frequency coverage of 4.07 GHz -5.58 GHz and a bandwidth of 17.8-41.1 MHz respectively. The unloaded quality factor Q_0 is from 300-500 over the tuning range.

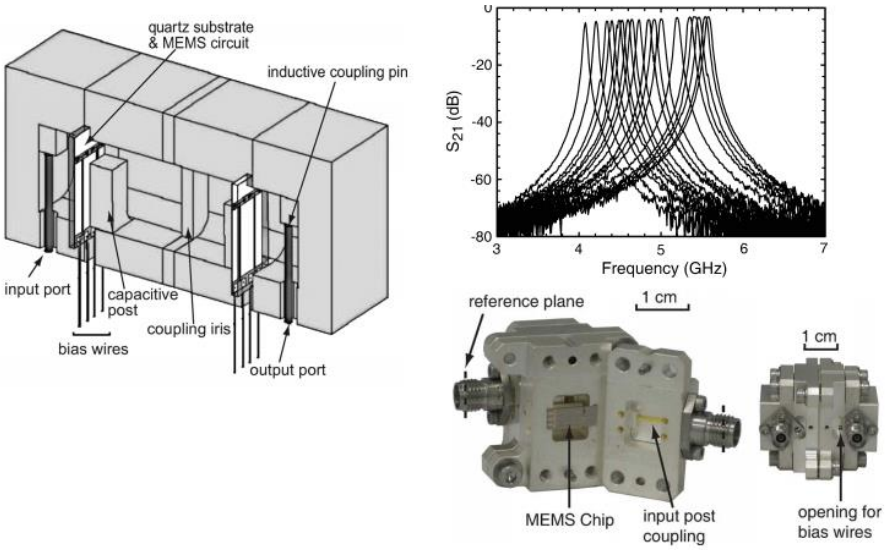

Figure 7 : Two pole evanescent mode cavity filter [14]

A final example of a dielectric resonator filter using MEMS is shown in [15]. There is a hole inside this cylindrical resonator in which three pieces of a line are bounded together by MEMS. So there are three states (three different lengths) depending on the OFF or the ON state of the MEMS. The disturbance created by the lines changes the resonance mode of the dielectric and therefore the frequency increased from 4.65 GHz to 4.82 GHz with a quality factor of 510.

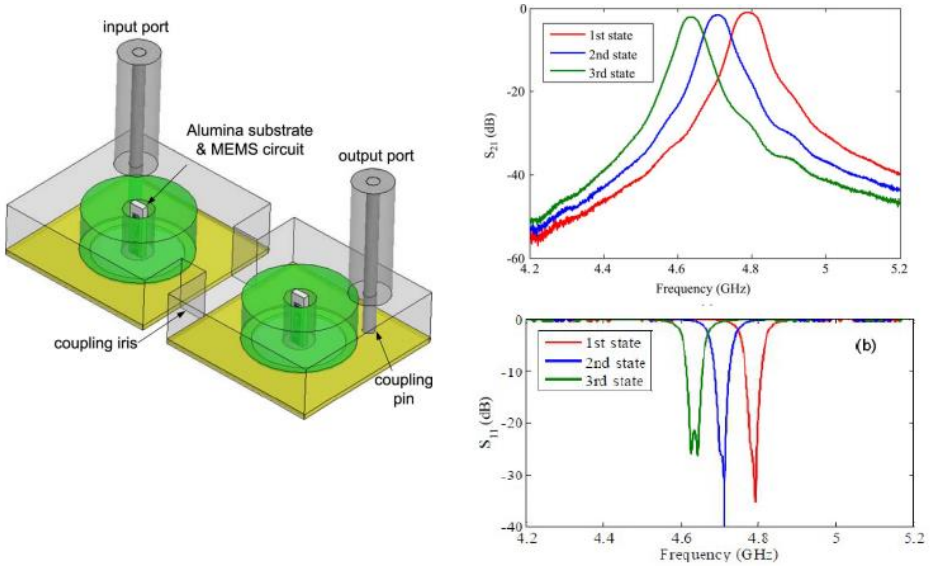

Figure 8 : High Q tunable dielectric resonator filter

In conclusion, MEMS appear to be a good candidate for tunable RF microwave devices but the need for large bias voltages makes the design more complex and the cost of the MEMS themselves do not match with our goal, namely the implementation of an inexpensive tunable system that is easily designed.

1.3.2 Varactor diodes

The varactor diode is one of the simplest and most common choice for creating tunable components. Varactor diodes are semi-conductor devices are widely used in the electronic industry and applications where a voltage controlled variable capacitance is required.

A varactor diode is a P-N junction diode in reverse bias so no current flows. The value of the capacitance and the series resistance of the diode changes according to the reverse bias applied. The thickness of the depletion zone varies with the applied bias voltage and so impact to the value of the capacitance. This one is controlled by the method of doping in the depletion layer. Typical values are from tenth to hundreds of picofarads. The ability of this type of diode to achieve changing to this capacitance is very useful to change the phase of an electrical circuit or to shift the resonant frequency for a device such as a filter. A model of a packaged varactor diode is shown in Figure 9.

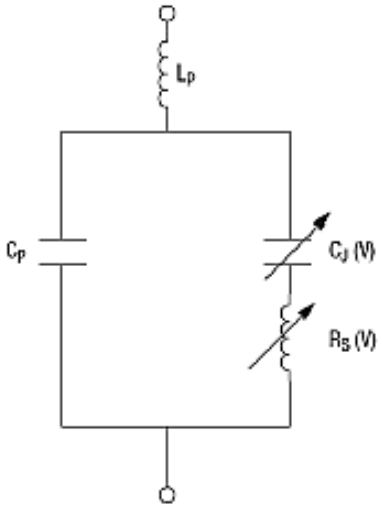

Figure 9 : Model of a packaged varactor

With:

- $C_j(V)$ = the variable junction capacitance of the diode.
- $R_s(V)$ = Variable series resistance of the diode.
- C_p = the fixed parasitic capacitance.
- L_p = the parasitic inductance.

The quality factor for a varicap is an important parameter since it determines the frequency limit applicability for the diode.

Some simple examples of tunable bandstop filter with tunable center frequency can be found in [16], [17]. The first one has a tunable center frequency between 1.04 GHz and 3.13 GHz (Figure 10) whereas the second one has a tunable center frequency from 1.2 GHz and 1.6 GHz and a bandwidth between 70 MHz to 140 MHz.

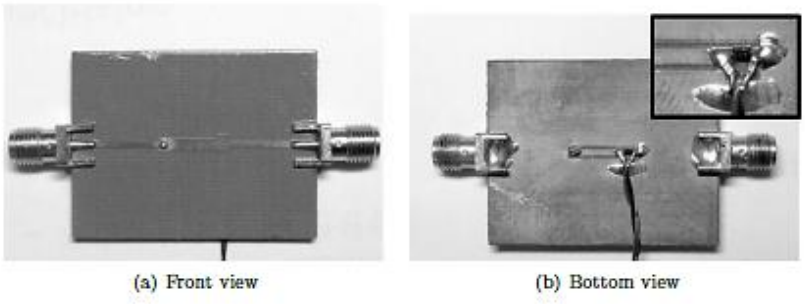

Figure 10 : Fabricated tunable bandstop filter based on varactor diodes [16]

As well many bandpass filters are in the literature and some of them with an original way of tunability will be explained and illustrated.

In the first bandpass filter [18] the varactor diodes are used to tune the center frequency of a 4 pole filter as well as the transmission zeros at the same time. As a result its selectivity can change. The varactor diodes are used as a loading capacitor and as coupling capacitor between each combline resonator. The f_0 is tuned from 1.25 to 2.1 GHz and the two transmission zeros are either in the upper band or in the lower band (Figure 11). This method brings a good tuning flexibility on f_0 and a good zero coupling with high isolation. The selectivity of each band can also change.

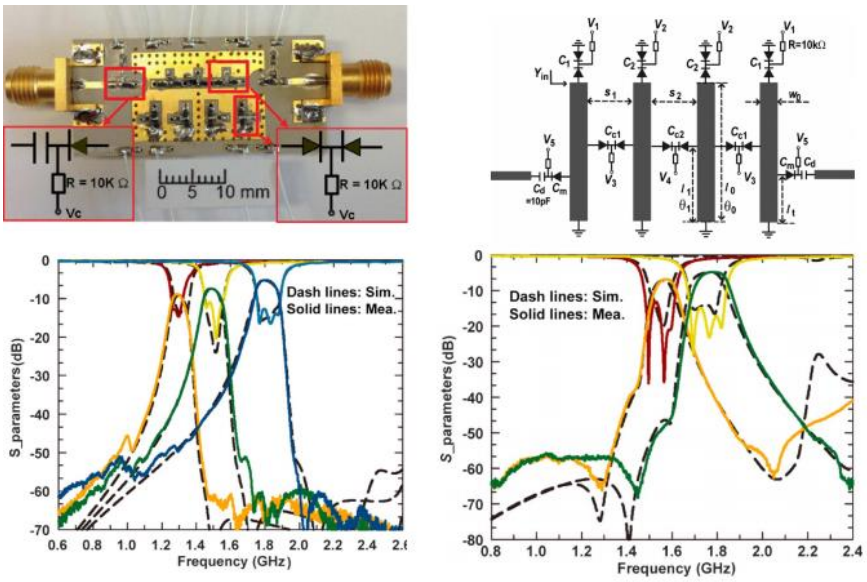

Figure 11 : Tunable 1.25-2.51 GHz 4-pole Bandpass filter with intrinsic transmission zero tuning-upper band (left)-lower band (right) [18]

The same research team has developed other types of filters based on the variation of the intrinsic magnetic or electric coupling such as [19] and [20]. This first article presents a tunable 2 and 4 pole bandpass filter with a wide tuning range providing by a zero value coupling effect (the magnetic coupling and the electrical coupling cancel each other) thanks to a coupled line with two coupling path loaded by coupling capacitances (varactor diodes). As a result both the frequency and the bandwidth are tuned. On top of that dual zero value couplings can eliminate the high band or the low band of the dual band filter The 2 pole filter has insertion loss of 2.9-4.7 dB with a tuning range from 0.75-1.09GHz (lower band) and 1.70-2.18 GHz (high band) respectively. The S parameters of the 2 pole filter are in (Figure 12) and each color represents a specific value of capacitance.

The second article highlights another tunable planar bandpass filter with transmission line resonator loaded by two varactors with asymmetrical capacitances and can turn into a bandstop filter by activating RF MEMS switch. The bandpass mode has a center frequency tuning of 0.7-1.10 GHz with a tunable 1-dB bandwidth of 68-120 MHz at 0.95 GHz.

A more detailed bibliography was written about RF/microwave reconfigurable bandpass planar filter in [21].

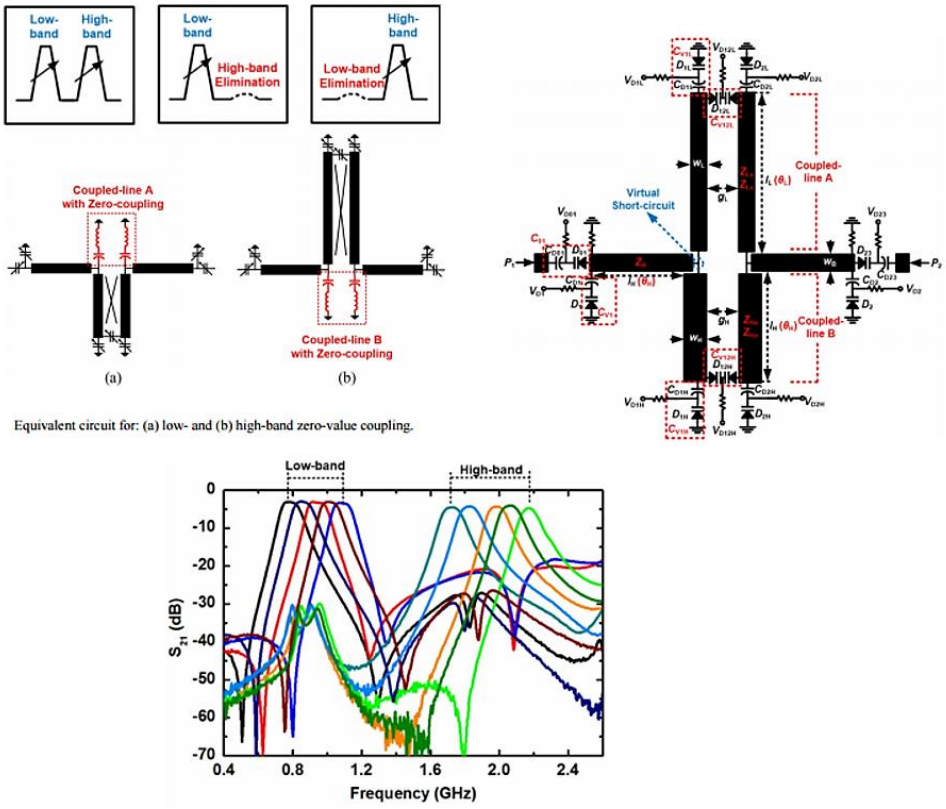

Figure 12 : Tunable 2 pole filter 0.7-2.1 GHz bandpass filter based on dual zero-value couplings [21]

The previous papers exhibit good tuning range, flexibility implementation but by the nature itself of the filter (planar) the quality factor cannot reach high value (<100). The following part introduces higher Q filter with the varactor technology.

One example is [22], where a cylindrical cavity loaded by a metallic post is connected to the top of this cavity in order to create a RLC resonator. Then, a circular pattern is etched on the metallized surface located on the top of the structure. Thus the created gap is loaded by varactor to modify the whole effective capacitance and the resonance frequency of the system (Figure 13). All type of elements with a changing capacitance can be used in this structure. The results are shown by a 2-pole filter with a tuning range from 0.5 to 1.1 GHz and insertion loss between 4.46-1.67 dB respectively and a return from dB to 27.8 dB. The quality factor changes from 84 to 206. An improvement is suggested in [23] in which a control of the couplings is achieved and integrated in the same way than the previous article. Therefore this

filter offers a continuous control of the resonance frequency and the bandwidth. The f_0 varies from 0.55 GHz to 1.13 GHz and the bandwidth from 34 to 40 MHz.

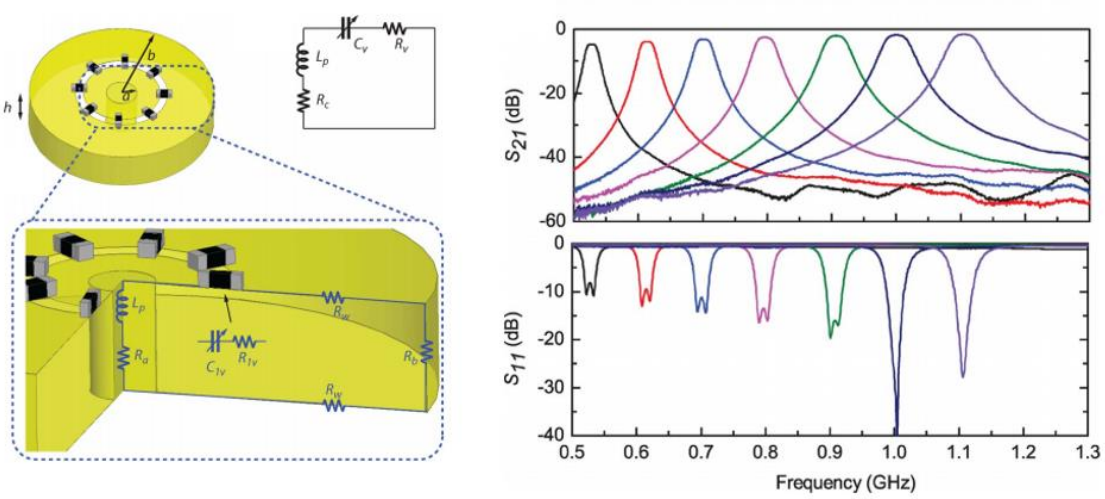

Figure 13 : two pole bandpass filter loaded by varactor

Here the cylindrical cavity is created thanks to electrical vias which permit to create a substrate integrated waveguide (SIW) resonator. This type of structure is widely used jointly with varactors to create High Q reconfigurable filter. This technology is explained with more details in the next chapter with examples of tunable SIW structures.

In spite of the attractive features of varactor diodes, these tuning devices require bias circuits that may limit the bandwidth and Q-factor performance.

1.3.3 Ferroelectric materials

Ferroelectric materials have become more attractive for the designs of tunable microwave systems for frequency agile application like filters thanks to the development of low-cost fabrication processes for making ferroelectric thin films. Besides, the power capability and fast tuning speed of this type of device are very appealing but such materials have high dielectric loss and low tunability. The varactors made up with ferroelectric material are capable of out-performing solid-state varactors at microwave frequencies due to their very high dielectric constant (>300) and lower parasitic series resistance which lead to a higher Q factor up to 160 according to [24]. Contrary to conventional varactors based on p-n junctions,

Schottky diodes and MOS varactors, the characteristics of ferroelectric capacitors do not depend on substrate semiconductor features such as doping density. Besides, these elements can be easily integrated on many substrates such as silicon carbide, GaN and GaAs. This is why this type of capacitor is widely used for tunable high-frequency circuit applications. A ferroelectric capacitor is shown in Figure 14.

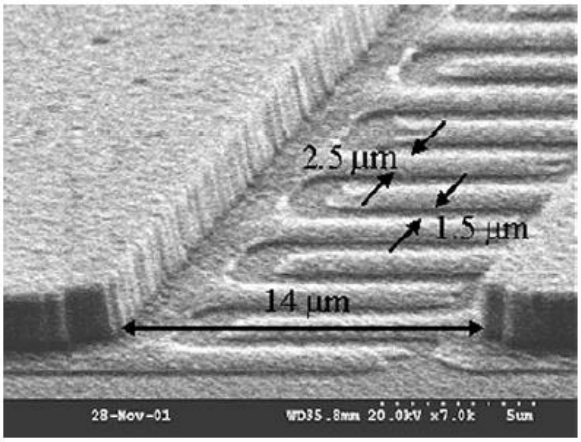

Figure 14 : SEM photograph of a fabricated ferroelectric capacitor[25]

Although ferroelectric materials can provide great changes depending on the electric field applied, they have some drawbacks to be used as tunable dielectric materials. Indeed the ferroelectric effect is strongly temperature dependent. This type of material needs to be monocrystalline in structure which makes them more expensive and difficult to use. There are also some limitations on the field strength of the microwave signals and where and how they can be used because of their electrical tunability.

Mostly a bandpass filter is combined with a barium strontium titanate (BST) lumped element to make this filter tunable. The following papers give examples of ferroelectric tunable bandpass filter.

The paper [26] presents a second-order quasi-elliptic ferroelectric BPF for Ka band based on epitaxial BSR on sapphire technology. The filter is designed with coupled-line coplanar waveguide (CPW) to reach good compactness and a good loss level. Four CPW quarter-wavelength resonators are loaded by BST tunable capacitors (one capacitor for each resonator) and when a tuning voltage is applied on a ferroelectric material the value of the capacitances changes as well as the frequency response. So the BPF has a frequency tuning of

2.4 GHz (33.6-36 GHz) at biasing levels (<30 V) which is low compared to [27][28] (>100V) with a loss of 6.2-74 dB respectively. The topology of the filter and its frequency response are illustrated in Figure 15.

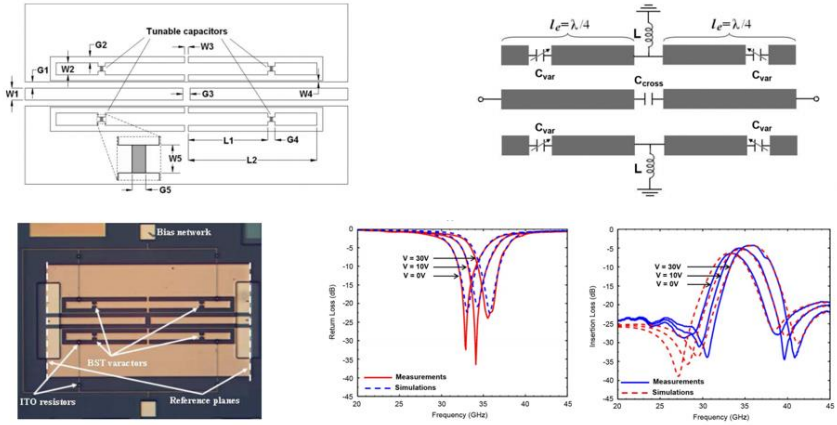

Figure 15 : Ka-Band tunable filter Bandpass filters using ferroelectric capacitors [26]

Another filter is presented in [29] with the use of BST capacitors and MEMS switches in order to control simultaneously the frequency and bandwidth. Like the previous the BPF is based on CPW resonator loaded by BST capacitors. Those ones effectively increase the electrical lengths of the resonator to shift the frequency in the resonant poles. The tuning of the bandwidth is achieved by the MEMS switches and a conductive path which can change the coupling between adjacent resonators. This path is either connected or isolated to the ground planes. The BPF created then has a frequency tuning from 30 to 35 GHz with insertion loss from 10 to 2.7 dB. Besides for this two pole filter the fractional bandwidth is about 9.6 % (wideband configuration) and 4.8% (narrowband configuration).

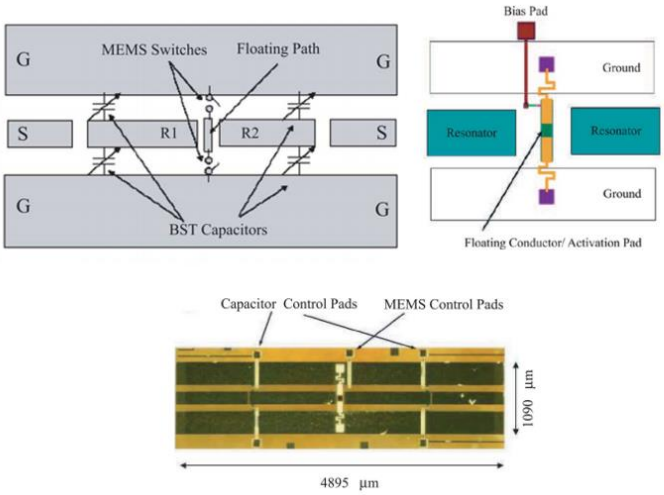

Figure 16 : Two poles filter using MEMS switches and ferroelectric capacitors [29]

1.3.4 Ferromagnetic materials

This type of material is often used to accomplish functions such as phase tuning, circulation, isolation and attenuation. Even with the enhancement in passive integration technologies, inductors for VHF application (30 MHz-300 MHz) and UHF (300 MHz-3GHz) filters remain large components, inhibiting further miniaturization in different applications. The use of magnetic material is seen as an option to substantially decrease their size. Compared to alternative miniaturization approaches, like lines width reduction and efficient use of mutual inductance in multi-layer and multi-winding inductors, the use of the ferrite might be the unique option in ceramic based LTCC technology for instance. While for the kHz and lower MHz frequency range high permeability is available, new cubic and hexagonal ferrites can reach gyromagnetic resonance frequencies well above 1GHz and can be integrated into LTCC technology.

There is a strong need to address the long standing issues in ferrite phase shifter technology to allow the intrinsic advantages of this technology, such as low insertion loss and high power handling to be used to achieve new capabilities in modern military and commercial applications.

Garnet ferrites, e.g. yttrium iron garnet (YIG), are widely utilized in high frequency devices because of their low dielectric and magnetic losses and moderate saturation magnetization values. Varying the externally applied magnetic field results in variation in the magnetic permeability and the phase velocity and insertion phase.

Unlike cubic garnet ferrites, hexagonal ferrites have high magnetocrystalline anisotropy energy due to the hexagonal crystal structure. A number of different hexagonal ferrites have found applications in electronics, magnetic recording, permanent magnets, as well as high frequency devices. This material has previously been utilized to reduce bias field requirements in phase shifter [30] and circulator [31] devices operating in the millimetre-wave regime.

Magnetoelectric materials have great capability of energy conversion between magnetic field and electric field and can be used in many different domains, such as civil wireless communication systems, military phased array radar and microwave devices like

filters, resonators, isolators, etc. These type of device based on laminated Magnetoelectric materials have less consumption, wide-range frequency tuning by magnetic field higher than 75% and accurate electric tunability as low as 0.5% for an applied electric field of E=10kV/cm[32]. Thus, this dual tunability due to piezoelectric effect and ferromagnetic resonance (FMR) will have wide application prospects.

A specific type of magnetoelectric materials are the ferrite-ferroelectric (FF) heterostructures due to their response to elastic and electromagnetic force field [33]. Such materials have permeability, permittivity and magnetoelectric susceptibility features suitable for reciprocal signal processing devices. Ferrites are used in traditional microwave/millimiter-wave devices in which tunability is realized, through a variation of the bias magnetic field [34]. This magnetic effect could be achieved in a very wide frequency range, but is relatively slow and is associated with large power consumption.

For instance a bandpass filter was designed with yttium iron garnet (YIG) films in [35]. This BPF is a magnetically tunable one. The design is based on a T shaped (to improve the insertion loss) microwave transducer with a compact coupling structure. Then a YIG film is deposited on another substrate made of gadolinium gallium garnet (GCG). The whole structure acts like a BPF filter whose ferromagnetic resonance is tuned via a bias magnetic field. The tuning range is from 190-840 MHz with small bias field of 50-250 Oersted (Oe) and low insertion loss < 2dB. The design of the BFP and its S parameters are shown in Figure 17.

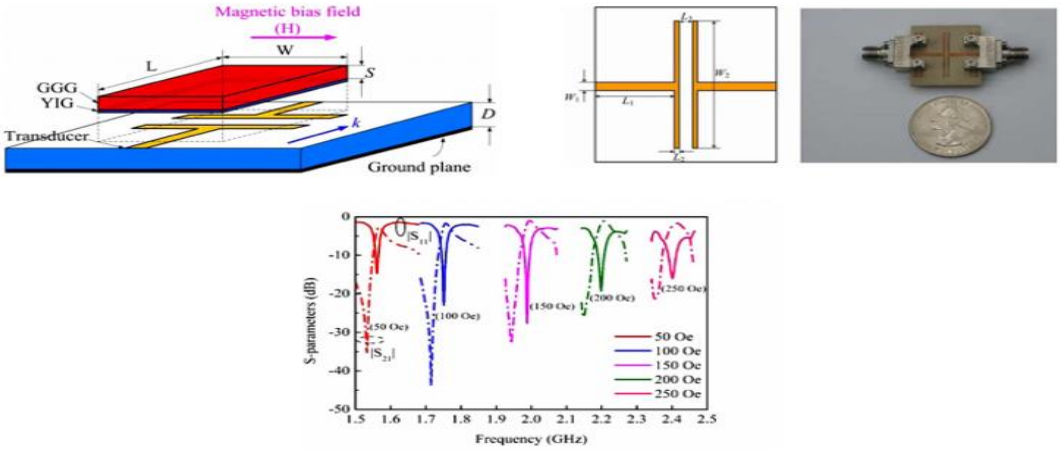

Figure 17 : Low loss magnetically tunable bandpass filter [35]

Ferroelectric and ferromagnetic materials could be a potential solution but these types of materials are not inexpensive and they are associated with a large power consumption and/or large bias field requirements. On top of that the need for elaborate biasing schemes for such an application increases the cost of the whole design.

1.3.5 Microfluidic technology

Microfluidics have become a valuable tool since the last decade to manipulate, analyse and interact with tiny amounts of liquid for biomedical applications such as blood analysis and bio-assays. With the achievement of microfluidic systems, the fluid analysis can be performed on samples of the order of microliters thanks to the monolithic integration of interface and sensing electronics. The cost of such systems is very expansive though and time consuming due to the micrometre-sized encapsulated fluid channels. Microfluidic devices are typically fabricated by using a clean room processing lithographic processes. But alternate fabrication methods can afford a lower cost and rapid production of microfluidic devices such as laser-etched fluidics, craft cut fluidics and wax-impregnated capillary action fluidics on paper [36]–[38]. An example of microfluidic channel is shown in Figure 18.

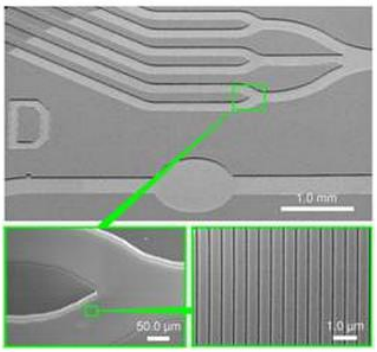

Figure 18 : Open microfluidic channel network [36]

S. cook et al proposed a novel approach [39] for the fabrication and the integration of low-cost microfluidic channels by using multilayer inkjet printing fabrication techniques. This technology offers a rapid and additive process which can deposit a wide variety of materials including metals, dielectric and nanomaterial-based sensors at low cost [40]–[42]. Coupled with a laser which can etch precisely these channels it is possible to produce RF systems such as tunable microfluidic RF capacitors and resonators [39].

At microwave frequencies, fluids exhibit large differences in their electrical parameters:

- Relative permittivity , ε_r
- Conductivity, σ
- Loss tangent , tan δ

So a microwave system in which different fluids are introduced can cause huge changes in the system properties based on field interactions with the fluids. Then, the creation of a fluid tunable microwave system is possible. Mostly in the literature the fluid is considered as a replaceable dielectric for transmission lines microwave resonator or antennas [43]–[47]. The propagation constant of a transmission lines or the resonance of a resonator or antenna can be change by introducing fluids with different constitutive parameters as a dielectric. Nevertheless, this type of device is complex and might utilize large-scale fluidics.

For creating tunable microfluidic bandpass filter, microfluidic varactors are used. They consist of a planar capacitive structure with a gap which is fed by microstrip lines. A fluid cavity is etched and bonded directly over the gap to allow for the delivery of the fluid. Depending on the liquid used, the capacitance is not the same (Figure 19).

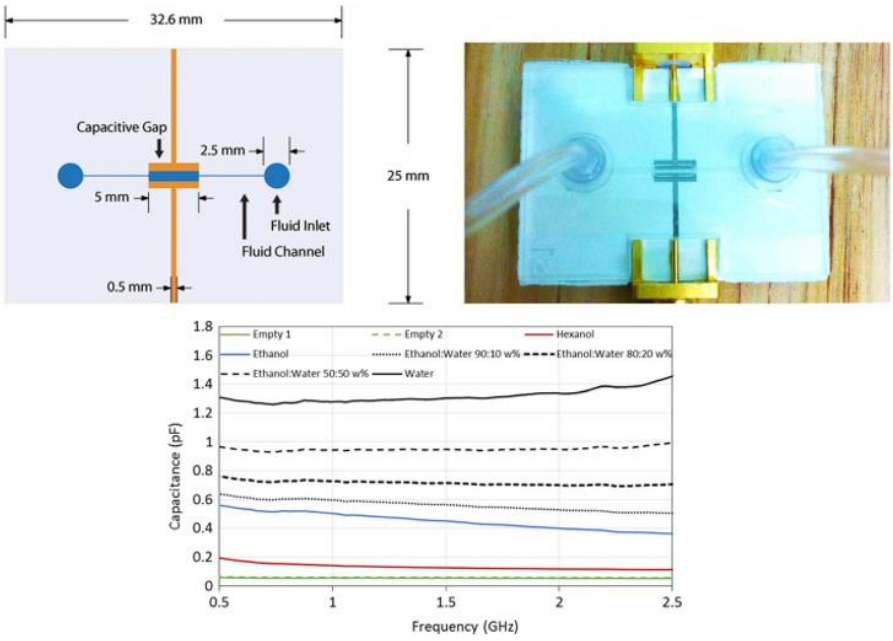

Figure 19 : Microfluidic varactor [39]

Few examples of microfluidic tunable filters exist in the literature such as a bandstop filter [48] and bandpass filters [49][50]. The first one is based on split ring resonators which are modeled as series R-L-C. A microfluidic varactor is created thanks the gap capacitance of the SRRS and when liquids of different permittivity are present over the gap, the value of the capacitance changes due to variations in the displacement field strength. The BSF has a resonant frequency of a 2.4 GHz for an empty cavity and of 1.68 GHz (30% of f_0) for cavity filled with water.

For the BPFs, one is based as well on open loop resonators which are capacitively loaded by metallized glass plates. By using microfluidics, they can be repositioned over the resonators and change the capacitive loading and therefore causes a shift of the resonant frequency. The filter exhibits a 50% tuning range from 1.5 GHz to 0.9 GHz with insertion loss lower than 1.7 dB in the pass band.

The last filter of this part is a BPF is a tunable L-band filter on a liquid crystal polymer (LCP) sitting on a top of a microfluidic channel. The resonant frequency is tuned by changing the fluid inside the channel and therefore the effective dielectric constant. In this case, the liquid (DI water) is replaced by micro pumping action. The measured results show a 33% tuning range from 1GHz to 1.5 GHz with insertion loss of 1.4 dB and 2.5 dB respectively.

Even though the quality factors are not mentioned for the previous filters they are inferior than 100 due to the use of microstrip lines.

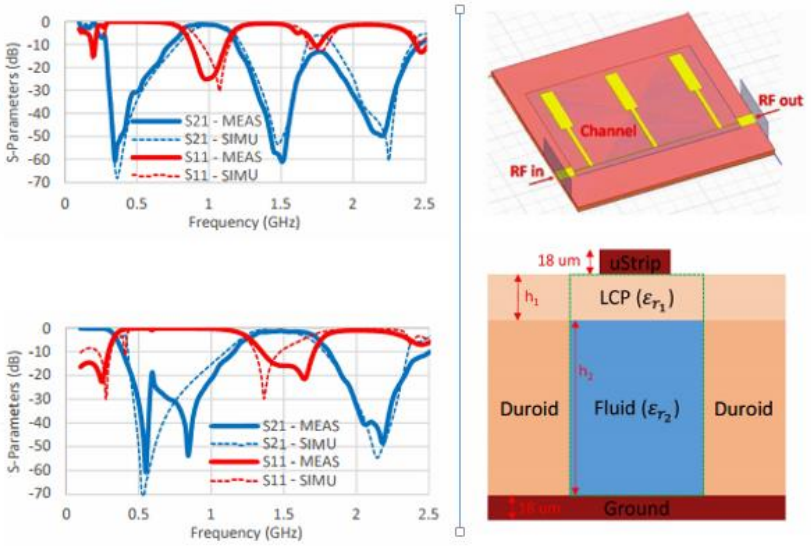

Figure 20 : Tunable microstrip BPF on Multilayer organic substrate [50]

The microfluidic technology provides good tuning range about 50% for the best case [50] the insertion loss measured for the BPFs are lower than 2 dB. This tuning technology is also used in wearable electronics [51], [52] systems for changing the operating frequency of antennas. However, the change of the resonant frequency is discrete and not continuous due to the huge different of the electrical parameters of the fluids and the switching time is not appropriate for applications which need a fast frequency change because the channels have to be clear out before filling them with a new one. Even if the integration of such components are really interesting considering the monolithic integration and lasers able to etched micrometer channels, the design could be quite complex and expansive if a multilayer technology is used to embed microfluidic channels.

1.4 Conclusion

The evolution of telecommunications systems leads to design and fabricate inexpensive devices which offer a better implementation and performances. Therefore, a lot of effort has been performed to develop tunable technology to solve these issues in wireless communications for radar, Wi-Fi or satellite applications.

This part gives an introduction and a general overview of tunable methods and emphasized by examples of bandpass filters using different technology (MEMS, Varactor, etc…). The tunability methods describe previously require an external biasing that can potentially degrade the primary response of the designed circuit such as the unloaded quality factor for the bandpass filters. The other issue is the complexity of the biasing systems for high order filter which limits the enhancements of integration of such structures. This thesis proposes an alternative solution based on optical control. Indeed, optical tunability shows great capabilities to avoid this problem as the optical waves do not interfere with the electromagnetic waves (which contain the information) of the circuit themselves.

The optical tunability is presented in two forms, the indirect optical control and direct optical one later in this thesis. This method is illustrated by two examples of bandpass filters which are a SIW filter and a cavity filter.

1.5 Bibliography

[1] I. C. Hunter, L. Billonet, B. Jarry, and P. Guillon, “Microwave filters-applications and technology,” *IEEE Trans. Microw. Theory Tech.*, vol. 50, no. 3, pp. 794–805, Mar. 2002.

[2] M. Bakri-Kassem and R. R. Mansour, “Linear Bilayer ALD Coated MEMS Varactor With High Tuning Capacitance Ratio,” *J. Microelectromechanical Syst.*, vol. 18, no. 1, pp. 147–153, Feb. 2009.

[3] R. Stefanini, M. Chatras, A. Pothier, J.-C. Orlianges, and P. Blondy, “High Q tunable cavity using dielectric less RF-MEMS varactors,” in *Microwave Integrated Circuits Conference, 2009. EuMIC 2009. European*, 2009, pp. 391–394.

[4] M. Rais-Zadeh, P. A. Kohl, and F. Ayazi, “MEMS Switched Tunable Inductors,” *J. Microelectromechanical Syst.*, vol. 17, no. 1, pp. 78–84, Feb. 2008.

[5] J. B. Muldavin and G. M. Rebeiz, “High-isolation CPW MEMS shunt switches. 2. Design,” *IEEE Trans. Microw. Theory Tech.*, vol. 48, no. 6, pp. 1053–1056, Jun. 2000.

[6] A. Verger, A. Pothie, C. Guines, A. Crunteanu, P. Blondy, J. C. Orlianges, J. Dhennin, F. Courtade, and O. Vendier, “Sub-hundred nanosecond reconfiguration capabilities of nanogap RF MEMS switched capacitor,” in *Microwave Symposium Digest (MTT), 2010 IEEE MTT-S International*, 2010, pp. 1238–1241.

[7] N. Zahirovic, S. Fouladi, R. R. Mansour, and M. Yu, “Tunable suspended substrate stripline filters with constant bandwidth,” in *Microwave Symposium Digest (MTT), 2011 IEEE MTT-S International*, 2011, pp. 1–1.

[8] G. Chaabane, A. Pothier, M. Chatras, C. Guines, V. Madrangeas, and P. Blondy, “A 2-pole RF-MEMS tunable bandpass filter for high-power applications,” in *Microwave Conference (EuMC), 2014 44th European*, 2014, pp. 343–346.

[9] D. Bouyge, A. Crunteanu, A. Pothier, P. O. Martin, P. Blondy, A. Velez, J. Bonache, J. C. Orlianges, and F. Martin, “Reconfigurable 4 pole bandstop filter based on RF-MEMS-loaded split ring resonators,” in *Microwave Symposium Digest (MTT), 2010 IEEE MTT-S International*, 2010, pp. 588–591.

[10] D. Bouyge, A. Crunteanu, A. Pothier, P. O. Martin, P. Blondy, A. Velez, J. Bonache, J. C. Orlianges, and F. Martin, “Reconfigurable 4 pole bandstop filter based on RF-MEMS-loaded split ring resonators,” in *Microwave Symposium Digest (MTT), 2010 IEEE MTT-S International*, 2010, pp. 588–591.

[11] M. A. El-Tanani and G. M. Rebeiz, “High-Performance 1.5 #x2013;2.5-GHz RF-MEMS Tunable Filters for Wireless Applications,” *IEEE Trans. Microw. Theory Tech.*, vol. 58, no. 6, pp. 1629–1637, Jun. 2010.

[12] I. Reines, A. Brown, M. El-Tanani, A. Grichener, and G. Rebeiz, “1.6-2.4 GHz RF MEMS tunable 3-pole suspended combline filter,” in *Microwave Symposium Digest, 2008 IEEE MTT-S International*, 2008, pp. 133–136.

[13] S. Fouladi, F. Huang, W. D. Yan, and R. R. Mansour, “High- Narrowband Tunable Combline Bandpass Filters Using MEMS Capacitor Banks and Piezomotors,” *IEEE Trans. Microw. Theory Tech.*, vol. 61, no. 1, pp. 393–402, Jan. 2013.

[14] S.-J. Park, I. Reines, C. Patel, and G. M. Rebeiz, “High- RF-MEMS 4 #x2013;6-GHz Tunable Evanescent-Mode Cavity Filter,” *IEEE Trans. Microw. Theory Tech.*, vol. 58, no. 2, pp. 381–389, Feb. 2010.

[15] F. Huang, S. Fouladi, and R. R. Mansour, “High- Tunable Dielectric Resonator Filters Using MEMS Technology,” *IEEE Trans. Microw. Theory Tech.*, vol. 59, no. 12, pp. 3401–3409, Dec. 2011.

[16] S.-Y. Lee, W.-G. Lim, W.-S. Jeong, and J. W. Yu, “A tunable bandstop filter design using parallel coupled line resonator with varactor,” in *Microwave Conference, 2008. APMC 2008. Asia-Pacific*, 2008, pp. 1–4.

[17] A. C. Guyette, “Varactor-tuned bandstop filters with tunable center frequency and bandwidth,” in *2010 IEEE International Conference on Wireless Information Technology and Systems (ICWITS)*, 2010, pp. 1–4.

[18] T. Yang and G. M. Rebeiz, “Tunable 1.25 #x2013;2.1-GHz 4-Pole Bandpass Filter With Intrinsic Transmission Zero Tuning,” *IEEE Trans. Microw. Theory Tech.*, vol. 63, no. 5, pp. 1569–1578, May 2015.

[19] Y.-H. Cho and G. M. Rebeiz, “Tunable 4-Pole Noncontiguous 0.7 #x2013;2.1-GHz Bandpass Filters Based on Dual Zero-Value Couplings,” *IEEE Trans. Microw. Theory Tech.*, vol. 63, no. 5, pp. 1579–1586, May 2015.

[20] Y.-H. Cho and G. M. Rebeiz, “Two- and Four-Pole Tunable 0.7 #x2013;1.1-GHz Bandpass-to-Bandstop Filters With Bandwidth Control,” *IEEE Trans. Microw. Theory Tech.*, vol. 62, no. 3, pp. 457–463, Mar. 2014.

[21] R. Gomez-Garcia, M.-A. Sanchez-Soriano, K.-W. Tam, and Q. Xue, “Flexible Filters: Reconfigurable-Bandwidth Bandpass Planar Filters with Ultralarge Tuning Ratio,” *IEEE Microw. Mag.*, vol. 15, no. 5, pp. 43–54, Jul. 2014.

[22] A. Anand, J. Small, D. Peroulis, and X. Liu, “Theory and Design of Octave Tunable Filters With Lumped Tuning Elements,” *IEEE Trans. Microw. Theory Tech.*, vol. 61, no. 12, pp. 4353–4364, Dec. 2013.

[23] A. Anand and X. Liu, “Substrate-integrated coaxial-cavity filter with tunable center frequency and reconfigurable bandwidth,” in *Wireless and Microwave Technology Conference (WAMICON), 2014 IEEE 15th Annual*, 2014, pp. 1–4.

[24] T. S. Kalkur, A. Jamil, and N. Cramer, “Characteristics of Voltage Controlled Oscillators Implemented With Tunable Ferroelectric High-k Capacitors,” in *Applications of ferroelectrics, 2006. isaf ’06. 15th ieee international symposium on the*, 2006, pp. 364–367.

[25] Y.-K. Yoon, D. Kim, M. G. Allen, and J. S. Kenney, “A reduced intermodulation distortion tunable ferroelectric capacitor: architecture and demonstration,” in *Microwave Symposium Digest, 2003 IEEE MTT-S International*, 2003, vol. 3, pp. 1989–1992 vol.3.

[26] H. jiang, B. Lacroix, K. Choi, Y. Wang, A. T. Hunt, and J. Papapolymerou, "- and - Band Tunable Bandpass Filters Using Ferroelectric Capacitors," *IEEE Trans. Microw. Theory Tech.*, vol. 59, no. 12, pp. 3068–3075, Dec. 2011.

[27] G. Subramanyam, A. Zaman, N. Mohsina, F. W. Van Keuls, F. A. Miranda, and R. R. Romanofsky, "A narrow-band ferroelectric tunable bandpass filter for K-band applications," in *Microwave Conference, 2000 Asia-Pacific*, 2000, pp. 938–941.

[28] J. Sigman, C. D. Nordquist, P. G. Clem, G. M. Kraus, and P. S. Finnegan, "Voltage-Controlled Ku-Band and X-Band Tunable Combline Filters Using Barium-Strontium-Titanate," *IEEE Microw. Wirel. Compon. Lett.*, vol. 18, no. 9, pp. 593–595, Sep. 2008.

[29] C. Lugo, G. Wang, J. Papapolymerou, Z. Zhao, X. Wang, and A. T. Hunt, "Frequency and Bandwidth Agile Millimeter-Wave Filter Using Ferroelectric Capacitors and MEMS Cantilevers," *IEEE Trans. Microw. Theory Tech.*, vol. 55, no. 2, pp. 376–382, Feb. 2007.

[30] X. Zuo, P. Shi, S. A. Oliver, and C. Vittoria, "Single crystal hexaferrite phase shifter at Ka band," *J. Appl. Phys.*, vol. 91, no. 10, pp. 7622–7624, May 2002.

[31] P. Shi, H. How, X. Zuo, S. A. Oliver, N. E. McGruer, and C. Vittoria, "Application of single-crystal scandium substituted barium hexaferrite for monolithic millimeter-wavelength circulators," *IEEE Trans. Magn.*, vol. 37, no. 6, pp. 3941–3946, Nov. 2001.

[32] Y. K. Fetisov and G. Srinivasan, "Electric field tuning characteristics of a ferrite-piezoelectric microwave resonator," *Appl. Phys. Lett.*, vol. 88, no. 14, p. 143503, Apr. 2006.

[33] G. Srinivasan, E. T. Rasmussen, J. Gallegos, R. Srinivasan, Y. I. Bokhan, and V. M. Laletin, "Magnetoelectric bilayer and multilayer structures of magnetostrictive and piezoelectric oxides," *Phys. Rev. B*, vol. 64, no. 21, p. 214408, Nov. 2001.

[34] A. Okamoto, "The Invention of Ferrites and Their Contribution to the Miniaturization of Radios," in *2009 IEEE GLOBECOM Workshops*, 2009, pp. 1–6.

[35] G.-M. Yang, J. Wu, J. Lou, M. Liu, and N. X. Sun, “Low-Loss Magnetically Tunable Bandpass Filters With YIG Films,” *IEEE Trans. Magn.*, vol. 49, no. 9, pp. 5063–5068, Sep. 2013.

[36] H. Klank, J. P. Kutter, and O. Geschke, “CO2-laser micromachining and back-end processing for rapid production of PMMA-based microfluidic systems,” *Lab. Chip*, vol. 2, no. 4, pp. 242–246, Nov. 2002.

[37] A. W. Martinez, S. T. Phillips, B. J. Wiley, M. Gupta, and G. M. Whitesides, “FLASH: A rapid method for prototyping paper-based microfluidic devices,” *Lab. Chip*, vol. 8, no. 12, pp. 2146–2150, Dec. 2008.

[38] P. K. Yuen and V. N. Goral, “Low-cost rapid prototyping of flexible microfluidic devices using a desktop digital craft cutter,” *Lab. Chip*, vol. 10, no. 3, pp. 384–387, Feb. 2010.

[39] B. S. Cook, J. R. Cooper, and M. M. Tentzeris, “An Inkjet-Printed Microfluidic RFID-Enabled Platform for Wireless Lab-on-Chip Applications,” *IEEE Trans. Microw. Theory Tech.*, vol. 61, no. 12, pp. 4714–4723, Dec. 2013.

[40] B. S. Cook and A. Shamim, “Inkjet Printing of Novel Wideband and High Gain Antennas on Low-Cost Paper Substrate,” *IEEE Trans. Antennas Propag.*, vol. 60, no. 9, pp. 4148–4156, Sep. 2012.

[41] T. Le, V. Lakafosis, Z. Lin, C. P. Wong, and M. M. Tentzeris, “Inkjet-printed graphene-based wireless gas sensor modules,” in *Electronic Components and Technology Conference (ECTC), 2012 IEEE 62nd*, 2012, pp. 1003–1008.

[42] L. Yang, A. Rida, R. Vyas, and M. M. Tentzeris, “RFID Tag and RF Structures on a Paper Substrate Using Inkjet-Printing Technology,” *IEEE Trans. Microw. Theory Tech.*, vol. 55, no. 12, pp. 2894–2901, Dec. 2007.

[43] J. Mateu, N. Orloff, M. Rinehart, and J. C. Booth, “Broadband Permittivity of Liquids Extracted from Transmission Line Measurements of Microfluidic Channels,” in *Microwave Symposium, 2007. IEEE/MTT-S International*, 2007, pp. 523–526.

[44] K. Grenier, D. Dubuc, P.-E. Poleni, M. Kumemura, H. Toshiyoshi, T. Fujii, and H. Fujita, “New broadband and contact less RF / microfluidic sensor dedicated to bioengineering,” in *Microwave Symposium Digest, 2009. MTT ’09. IEEE MTT-S International*, 2009, pp. 1329–1332.

[45] S. K. Pavuluri, R. Lopez-Villarroya, E. McKeever, G. Goussetis, M. P. Y. Desmulliez, and D. Kavanagh, “Integrated microfluidic capillary in a waveguide resonator for chemical and biomedical sensing,” *J. Phys. Conf. Ser.*, vol. 178, no. 1, p. 12009, Jul. 2009.

[46] T. Chretiennot, D. Dubuc, and K. Grenier, “A Microwave and Microfluidic Planar Resonator for Efficient and Accurate Complex Permittivity Characterization of Aqueous Solutions,” *IEEE Trans. Microw. Theory Tech.*, vol. 61, no. 2, pp. 972–978, Feb. 2013.

[47] M. Hofmann, G. Fischer, R. Weigel, and D. Kissinger, “Microwave-Based Noninvasive Concentration Measurements for Biomedical Applications,” *IEEE Trans. Microw. Theory Tech.*, vol. 61, no. 5, pp. 2195–2204, May 2013.

[48] W. Su, C. Mariotti, B. S. Cook, S. Lim, L. Roselli, and M. M. Tentzeris, “A metamaterial-inspired temperature stable inkjet-printed microfluidic-tunable bandstop filter,” in *Microwave Conference (EuMC), 2014 44th European*, 2014, pp. 9–12.

[49] T. Palomo and G. Mumcu, “Highly reconfigurable bandpass filters using microfluidically controlled metallized glass plates,” in *Microwave Symposium (IMS), 2014 IEEE MTT-S International*, 2014, pp. 1–3.

[50] O. L. Chlieh, W. T. Khan, and J. Papapolymerou, “L-band tunable microstrip bandpass filter on multilayer organic substrate with integrated microfluidic channel,” in *Microwave Symposium (IMS), 2014 IEEE MTT-S International*, 2014, pp. 1–4.

[51] K. Noda, M. Ohkado, B. K. Nguyen, K. Matsumoto, H. Fujikawa, and I. Shimoyama, “Frequency-Tunable Microstrip Antenna With Liquid Actuator Using Gradually Widened Transmission Line,” *IEEE Antennas Wirel. Propag. Lett.*, vol. 14, pp. 551–555, 2015.

[52] M. Jobs, K. Hjort, A. Rydberg, and Z. Wu, “A Tunable Spherical Cap Microfluidic Electrically Small Antenna,” *Small*, vol. 9, no. 19, pp. 3230–3234, Oct. 2013.

Chapter 2: Tunable SIW structures

2.1 Introduction

In the previous chapter a review about different tuning technologies was made for tunable microwave systems and more particularly about microwave filters. The filters illustrated in the last part were planar lines based (coplanar, microstrip, etc...) or volumetric (waveguide, cavity). But in the last 15 years a new technology has made a breakthrough for RF, microwave and millimeter-wave systems called the post-wall waveguide or the substrate integrated waveguide (SIW).

This technology was introduced by Deslandes and Wu [1] in 2001 and allows creating a synthetic rectangular waveguide formed in a substrate by arraying electrical post or metallized via-holes which connect the upper and the lower metallic plates of the substrate. Using this method, a nonplanar rectangular waveguide can be made in a planar form that is compatible with the printed circuit board (PCB) and low temperature cofired ceramic techniques [2]. On top of that SIW is a good candidate for developing planar microwave components with high quality factors. This technology has been applied for different types of microwave devices such as cavity filter[3] [4],antenna [5], leaky-wave antennas[6], oscillators [7] and so on. Devices created using SIW have most of the advantages of classic metallic waveguides [8]:

- Low loss and high quality factor (higher than 100)
- Permanent electrical isolation due to the shielding via posts
- High power handling (can be reduced due to the height of the substrate, the dielectric material and PCB fabrication process)
- Integrability capabilities of SIW structures with all sorts of passive and active components

The SIW structures inherit the integrability of planar structure and the quality factor of three dimensional waveguide structures so it forms a bond between those two technologies.

The high quality factor of this technology is very interesting for designing narrow bandwidth device with a high selectivity. Thanks to all that this technology is a good a candidate to create resonator for the first level of the concept depicted in Figure 1. The following part is a review of different SIW tunable filters with different technologies is made.

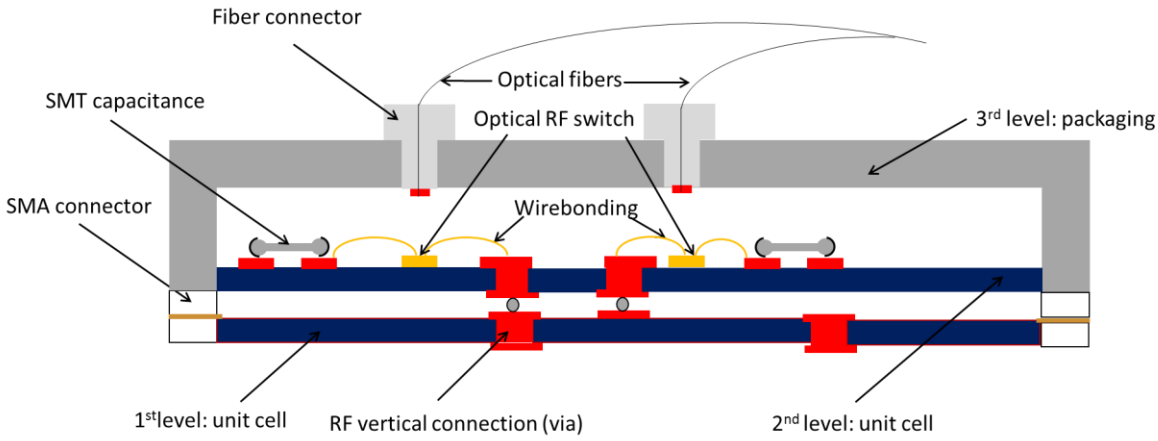

Figure 1: Block diagram for the concept of an optically tunable filter

2.2 SIW tunable filters

The SIW filters are interesting for high performance microwave circuits due to the ease of fabrication, high power handling, high linearity and integrability. But we have to keep in mind that such device with high Q_0 is narrow band and highly selective. It is important therefore to find methods and technologies to tune SIW filters over a wide tuning range while maintaining a high quality factor (Q). However, this is hard to achieve due to the tradeoff between the tuning range and the dropping of the Q of the resonator making the design of this type of filter more challenging.

SIW filters are made out of one, two or more cavity resonators depending on the number of poles needed or the increase of the bandwidth. It is possible to tune such filters by tuning all of the resonators simultaneously. The publication [8] previously quoted points out six different methods existing in the literature to tune SIW structures. Different tuning elements are used such as p-i-n diode, varactor diode, RF-MEMS switch and so on to tune the frequency response of the resonator and the resulting SIW structure.

2.2.1 Method 1

This tuning method was proposed in [9] for a tunable SIW cavity backed antenna oscillator. A varactor diode is coupled to the SIW cavity through an opening in one of the side walls. For tuning the antenna one via of the cavity wall is removed and the diode is connected between the top plane and a radial stub which creates an offset capacitance towards ground

(Figure 2). The varactor bias voltage V_c produces a change in the loaded cavity and as a result modifies the resonance frequency of the structure. The tuning range of this technique is low (2%) because the loading effect occurs in a low distribution E-field area. But the Q_0 of the resonator is not affected significantly (from 299 to 286).

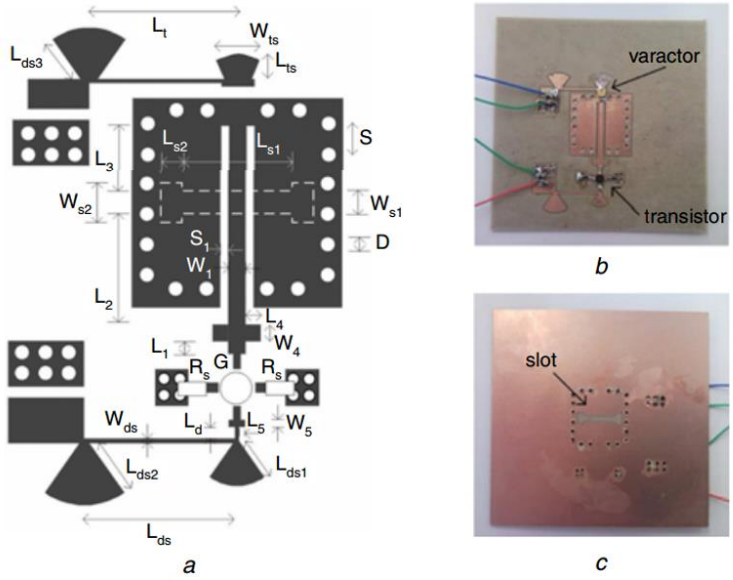

Figure 2: X-band SIW cavity backed antenna oscillator [9] (a) layout (b) top view (c) bottom view

2.2.2 Method 2

This method consists in creating a perturbation of the electric field inside the cavity to change the frequency of the cavity resonator. Armendiz et al.[10] were the first to propose this technique based on loading the said resonator with a via post and then connecting and disconnecting it from the cavity top wall by using a p-i-n diodes. By connecting the via to the top wall the field distribution inside the cavity changes. In the off state the disconnected via post load the resonator capacitively which results in miniaturization of the cavity. To switch each tuning via post on or off with p-i-n diodes a two layer structure is used (Figure 3).

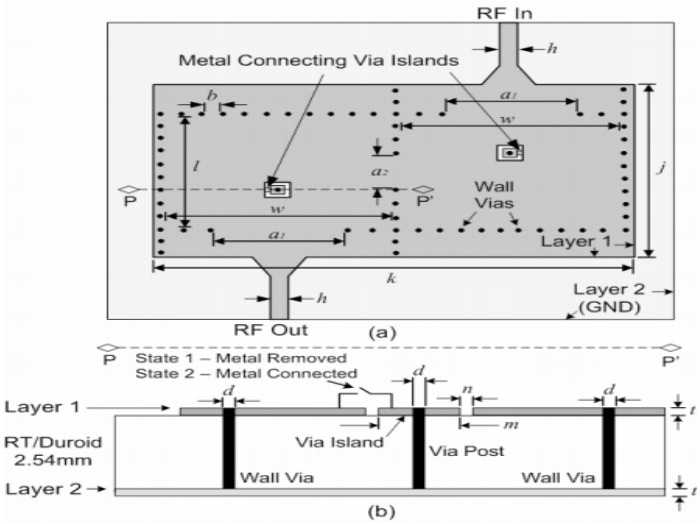

Figure 3: SIW filter layout with perturbing via posts, (a) top view (b) side view [10]

Several numbers of these tuning via posts can be used to achieve a widely tuned resonator. For four of these tuning via posts, the resonators achieves a tuning range of 25 % and the unloaded quality factor Q_0 varies from 130 to 90.

Based on the same technique a two-pole SIW RF MEMS cavity filter was presented in [11] and achieves a tuning range of 28% and a Q_0 from 132 to 93. This filter uses 14 different tuning states with a very fine frequency resolution to behave as a continuous tunable filter. Packaged MEMS are used as switching devices and are directly mounted on the biasing circuit layer of the filter to reduce the parasitic effects.

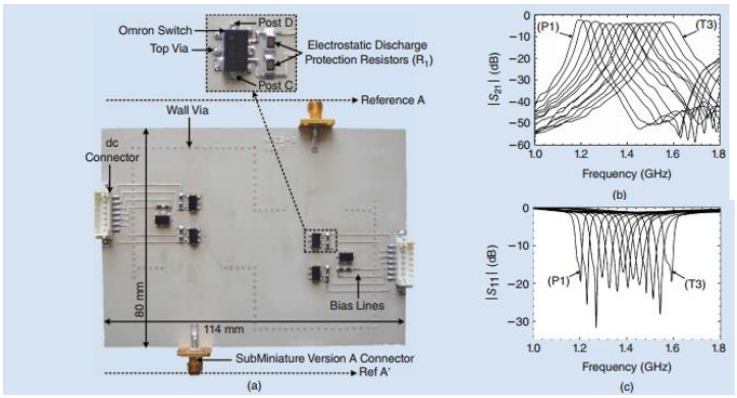

Figure 4 : (a) Tunable SIW filter with MEMS switches, (b) the measured S_{21} and (c) the measure S_{11} [11]

2.2.3 Method 3

A via post is connected to a metal patch on top of the cavity resonator, this technique was introduced by Sirci et al.[12]. A floating metal is used to load the via post with a varactor diode (Figure 5). As a result the electric field inside the cavity is changed as well as the frequency of the resonator. The resonance frequency changes thanks to a bias voltage of the diode which changes the reactive loading effect.

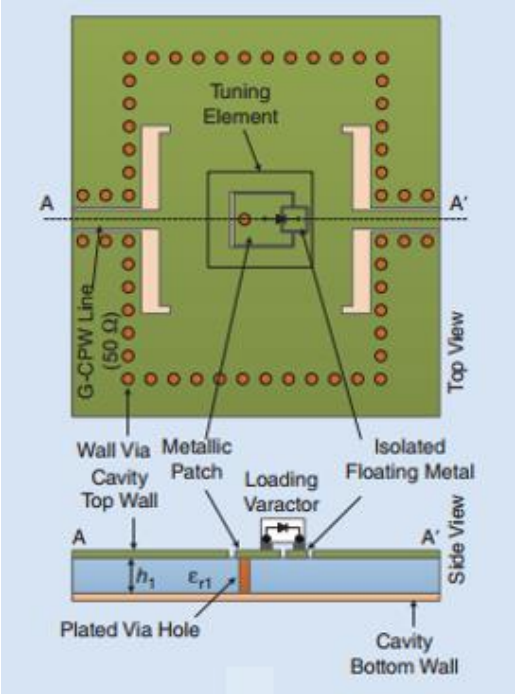

Figure 5: concept of the floating patch diode- loaded SIW cavity [13]

The tuning range of a filter is 18% with a Q_0 from 160-40. This fabrication is a one layer structure which is easiest to fabricate but the floating metal patch occupies a relatively large area so it limits the number of tuning via posts for increasing the tuning range.

Sirci et al. developed a two pole tunable SIW coupled resonator filter based on this technique [14]. This filter has a continuously fine tuning of this resonance frequency without introducing degradation of the in-band performance. The tuning range of the centre frequency is between 2.64 GHz and 2.88 GHz with 1.27 dB and 3.63 dB insertion loss respectively.

2.2.4 Method 4

Magnetic tuning with ferrites was introduced in [15]. Adhikari et al. in [16] does both an electric tuning by placing a varactor diode and capacitors inside the cavity and a magnetic tuning thanks to YIG ferrite slabs to change the external magnetic field. This type of method not only allows for changing the frequency but also optimizes both the return loss and the unloaded quality factor. However, implementing ferrite slabs is quite difficult and therefore increases the complexity of the implementation of such SIW structure.

A ferrite based SIW tunable filters [17] uses this. The electric tuning is achieved by varactor diodes with a total tuning range of 1.3% and up to 7.9% thanks to magnetic tuning and electronic one with a Q_0 of 130. Then, this method is applied for a second order Chebyshev filter bandpass filter. A tuning range of 10% is achieved while maintaining a constant bandwidth of 4.4% or a fixed frequency response with a tunable frequency bandwidth from 3 to 5%.

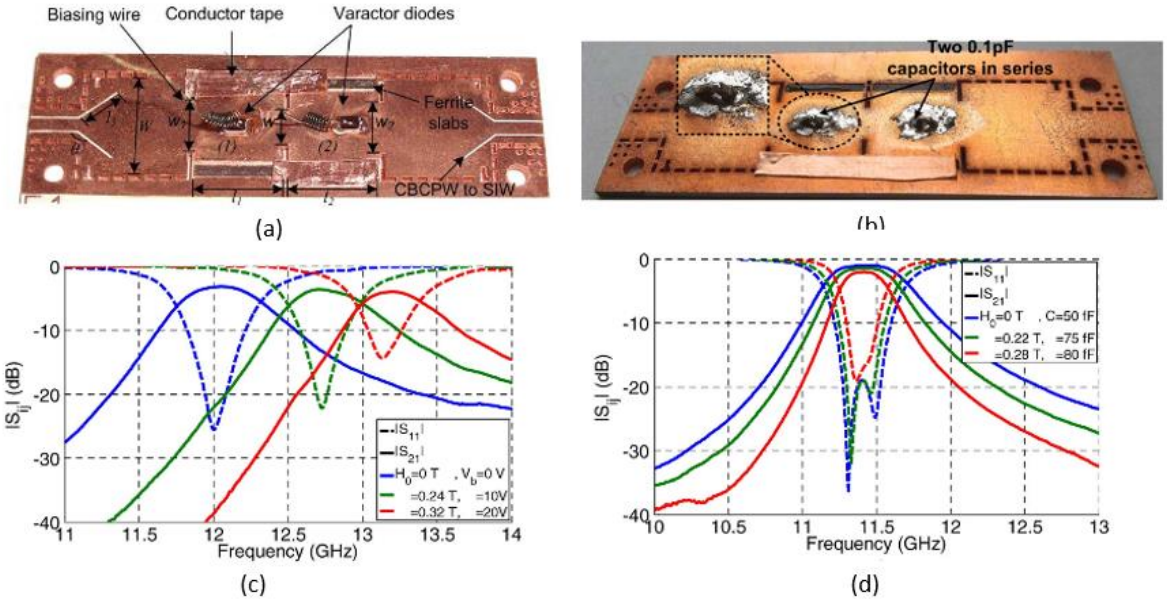

Figure 6 :Second order Chebyshev filter bandpass filter with (a) a top view (varactor diodes) and (b) a bottom view,(c) the S parameter measured for the frequency tunable filter case, and (d) The S parameters measured for the tunable BW case [17].

A method very similar can be found in [18].

2.2.5 Method 5

For this method a mechanically controlled via is used as switching devices to tune an SIW cavity resonator [19]. This via post is connected to a screw which is connected to a flap. To isolate the screw from the cavity top wall Mira et all use an annular ring (Figure 7). If the screw is turned around and stopped at different angles the resonance frequency of the resonator changes due to the variations of E-field distribution.

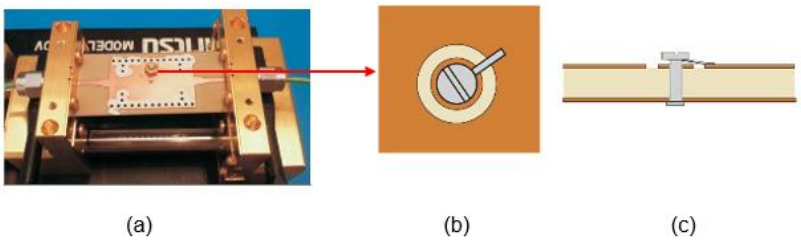

Figure 7 : (a) Fabricated prototype, (b) tuning mechanism top view, (c) side view [19]

This method affords a tuning range of 8% but it can increase up to 22% if a multiple of this tuning mechanism are used. The unloaded qualify factor is about 94 with a few variation since the tuning range is moderate. This method already exists to tune waveguide filters and might be interesting for low cost post processing tuning but it is difficult due to the insertion of the flap connected screw into the via post.

2.2.6 Method 6

This last method consists in loading a surface ring gap with varactor diodes. Indeed, in [20] vertical gap is connected to an etched ring on a cylindrical SIW resonator. This one is extended to connect the top and the bottom walls of the SIW cavity and annular slots are etched around the via post to isolate it from the rest of the cavity's top metallization. In order to tune the resonance frequency, the ring gap is loaded by varactor diode and then it changes the capacitance of the resonator. The tuning range achieved is 55% (1.1GHz-0.5 GHz) with a Q_0 ranging from 214 to 90. In the same publication a two pole filter is designed with the same tuning range and a measured insertion loss of 1.67 dB at 1.1 GHz. This same method is finally applied for a three pole filter with a tuning range of 52% and a measured insertion loss of 2.05 dB. The 3dB fractional bandwidth for both filters is 4%.

	Ref	Tuning Basis	Tuned Mode	Tuning range	Quality factor (Q0)	Linearity	Fabrication	Integration Potential
Method 1	[9]	side-coupled with varactor diode	Electrical (varactor diodes)	Low (2%)	Highest (299-286)	Moderate	Simple	Good
Method 2	[10]	Switchable perturbing via post(s)	Electrical (p-i-n diodes/RF MEMS switches)	High (25%)	High (130-90)	High	Moderate	Excellent but two layer structure
Method 3	[12]	Tunable perturbing via post	Electrical (varactor diodes)	Moderate (18%)	Moderate (160-40)	Moderate	Simple	Good
Method 4	[15]	Ferrite-based tuning+ tunable perturbing via post	Electrical (varactor diodes) + magnetic (ferrite slabs)	Low (8%)	High (130)	moderate	Complex	Poor/magnets are needed to tune the resonator
Method 5	[19]	Mechanically tuned/ via post	Mechanical	Low (8%)	Moderate (94)	Highest	Complex	Poor/the tuning is done manually
Method 6	[20]	Surface ring loaded with varactor diodes	Electrical	Highest (54%)	High (214-90)	Low	Simple	Good

Table 1: Comparison of the six tuning methods applicable to SIW [13]

The tradeoff previously stated between the tuning range and the variation of the quality factor is clearly seen in this table. Methods 1, 4 and 5 are interesting for having tuning range (low) without degrading the $Q_{0.}$ Conversely, the last method can achieve the widest tuning range with a good quality factor, although the latter degrades by 58 % of with tuning. Combining the electrical and magnetic tuning might be interesting to increase the tuning range but in the end the achievable variation is low, the fabrication is not easy and the integration potential is poor. The methods which achieve good performance (good tuning range and high $Q_{0)}$ with a good integration and easy fabrication are the number 2 and 6.

For the tunable SIW filters created throughout this thesis, an electrical tuning method has been chosen based on new optical switches (Method 2) and surface etching loaded with capacitance (surface mounted capacitor). In addition, a novel tunable SIW filter based on metamaterial effect is pursued.

2.3 First generation filter

For fulfilling the level 1 of the concept depicted in, several elementary cells have been investigated. Ideally, the tunable filter has to offer good performance such as high unloaded quality factor (Q_0) and a good tuning range. The first one is based on metamaterial properties which is interesting for miniaturizing the whole structure thanks to a substrate integrated waveguide (SIW) cavity and as a result might offers an interesting Q_0 (>100). The second proposed elementary cell is based on a cavity filter made with alumina to provide higher Q than the previous one.

2.3.1.1 Principle

This filter is based on the work of Y. Dong et al [21] . This generation 1 filter presents metamaterial effect which is interesting in our case for miniaturising the filter while having an interesting unloaded quality factor.

Metamaterials, which are broadly defined as artificial materials, exhibit unusual EM properties that cannot be obtained with traditional materials. They are explained in the general context of periodic structures with a periodicity smaller than the guided wavelength. Their properties include low values or negative ones of permittivity (ε), permeability (μ) and as a result refractive index (n). According to the previous statement a classification can be made about these exotic materials. Metamaterials with simultaneously negative permittivity and permeability are referred to left-handed (LH) materials [22]. Another class is the composite right/left handed (CRLH) structures which is the combination with a traditional materials (right handed) and a LH materials [23]. This classification can be illustrated by the Figure 8. The point A in this diagram represents the intersection of the various types of materials which have a zero-index media. Metamaterials with a refractive index of zero exhibit physical properties such as infinite phase and wavelength. Crafted zero index media material enables distinct forms of interaction with and control of light such as bending, focusing, shaping and cloaking.

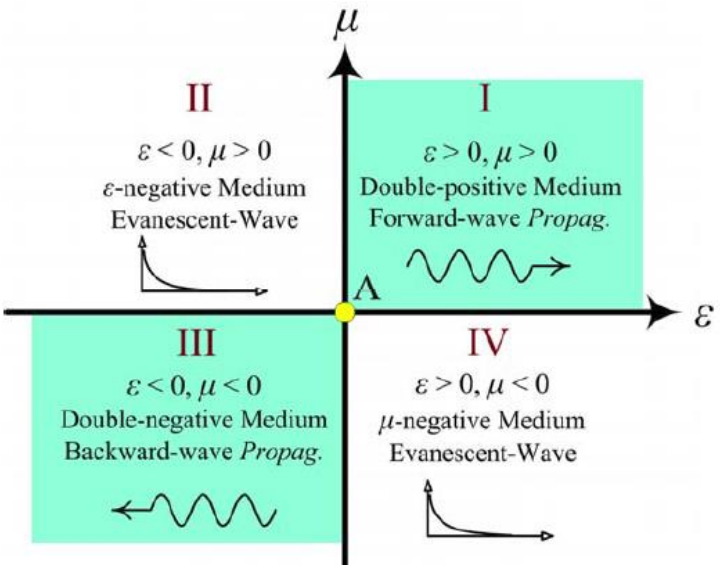

Figure 8: The permittivity-permeability diagram

As depicted in the Figure 8 the wave propagation exists only if the medium is double positive or double negative. The second case for LH material is characterized by anti-parallel phase and group velocities, negative index (NRI), and backward propagation which differs from traditional material.

The filter created in this section is a waveguide loaded by interdigital slots. A waveguide is used to achieve a high factor Q-factor for low loss components and with a good power handling capability. Moreover, such a constituent provides a negative permittivity when operated below the cutoff frequency of the dominant TE mode [24]. According to [25] the dispersion constant for a rectangular waveguide is the following:

$$k = \omega\sqrt{\mu_r \varepsilon_{eff}} \tag{1}$$

$$\varepsilon_{eff} = \varepsilon_r\left(1 - \frac{\omega_0^2}{\omega^2}\right) \tag{2}$$

In which ε_r and μ_r are the relative permeability and permittivity of the substrate within the waveguide, $\omega 0$ is the cutoff frequency for the considered mode. Below the cutoff frequency, ε_{eff} becomes negative and k an imaginary number. As a result the mode is evanescent. So automatically a uniform ε negative material is obtained without introducing any resonant structures.

In order to have a backward propagation with a waveguide a negative permeability is missing in order to simulate a LH behavior. Many possibilities exist introduced in [24] [26] suggesting the use of split ring resonators (SRRs) or complementary split ring resonators (CSRRs) on a waveguide. Another solution is to insert slot dipole etched on the top surface [27] to create an double negative material because slots are considered as magnetic dipoles placed along the H-field direction.

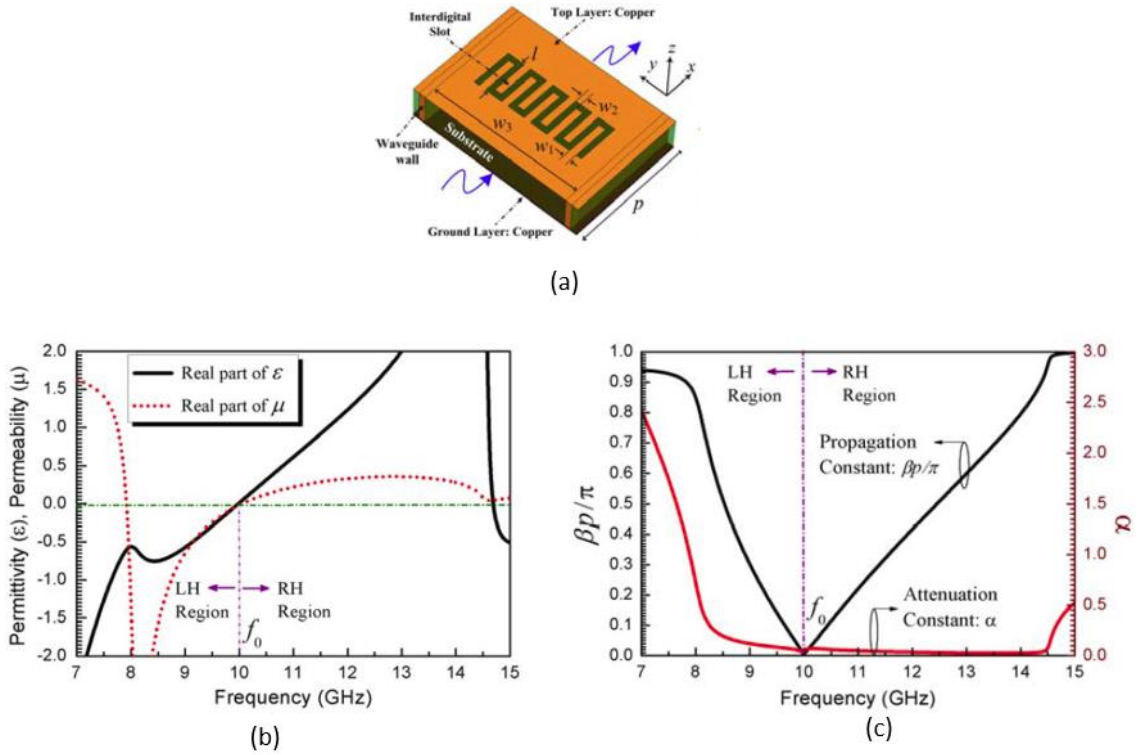

Figure 9:(a) Slot-loaded waveguide, (b) Effective permittivity and permeability (real part), (c) dispersion and attenuation constant [21]

In this example [21] the waveguide has a cutoff frequency f_0 of 10 GHz which represents the border between the LH and RH regions. With the increase of the frequency, the material changes from double-negative medium, to zero-index medium, and finally to double-positive medium. As determined in [23] the cutoff frequency for the LH and RH region are:

$$f_l = \frac{1}{2\pi\sqrt{C_l L_l}} \quad , \quad f_r = \frac{1}{2\pi\sqrt{C_r L_r}} \tag{3}$$

However since waveguides are bulky, heavy and it is very difficult to etch slots on the surface, a good solution to address the problem is the use of SIW structure. The equivalent circuit model for the original SIW is depicted in Figure 10. The metal wire and the ground can be modeled as a two-wire transmission line with distributed shunt capacitance and inductance which are associated with the permittivity and the permeability of the substrate. A via-walls (electric walls) is represented by inductance (L_l). The interdigital slot etched on the surface is represented by the capacitance C_l. They represent the LH contribution. The RH contribution is illustrated by the capacitance C_r from the waveguide and by the inductance L_r from the fingers of the capacitance.

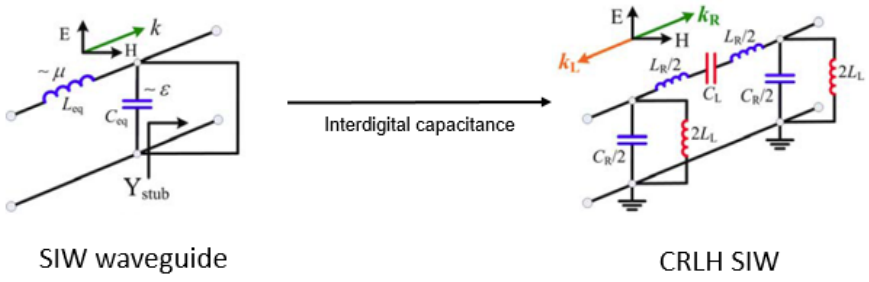

Figure 10: Equivalent circuit model for a SIW waveguide and CRLH SIW

By adding an interdigital slot on a SIW waveguide a CRLH SIW structure is created. The value of the capacitance can be adjusted conveniently, which will determine the position of the LH region. So to make a filter based on this tunable method, the value of C_l has to change by adding another capacitive effect (shunt or series capacitance). The value of an interdigital capacitance designed for that purpose is determined as:

$$C_L(pF) = (\varepsilon r + 1)\frac{l}{w}[(n-3)A1 + A2] \quad (4)$$

With:

- ε_r: relative permittivity of substrate
- **l**: finger's length
- **w**: finger's width
- **n**: number of fingers
- A1(pF)=$8.85.10^{-2}$.w (cm)

- A2(pF)=$9.92.10^{-2}$.w (cm)

2.3.1.2 Design and measurements

The design is designed with HFSS first. With SIW technology some rules have to be respected [28]:

$$b \leq 2D\ ,\quad D < \frac{2\lambda_g}{5} \tag{5}$$

With: b the distance between two via holes' centers; D the diameter of vias and λ_g the guided wavelength.

Thanks to the equivalent circuit model combined with HFSS software a first filter was created and is depicted in Figure 11. The substrate is made of Alumina with a permittivity of 8.65(loss tangent=1×10^{-4}) and a thickness of 0.53mm. However, strictly speaking the SIW structure is not based on a waveguide but on a SIW cavity. Indeed, in order to improve the insertion loss (S_{21} parameter) side via walls were implemented. On top of that the coplanar excitation lines are as long as possible to create a better coupling access to have good insertion loss about 1dB. In this configuration the dominant TE mode (TE_{101}) has a cutoff frequency of 6.4 GHz. The design of the interdigital capacitor gives a resonance frequency (f_0) at 2.41 GHz and the extracted capacitance (4) value is 0.4 pF.

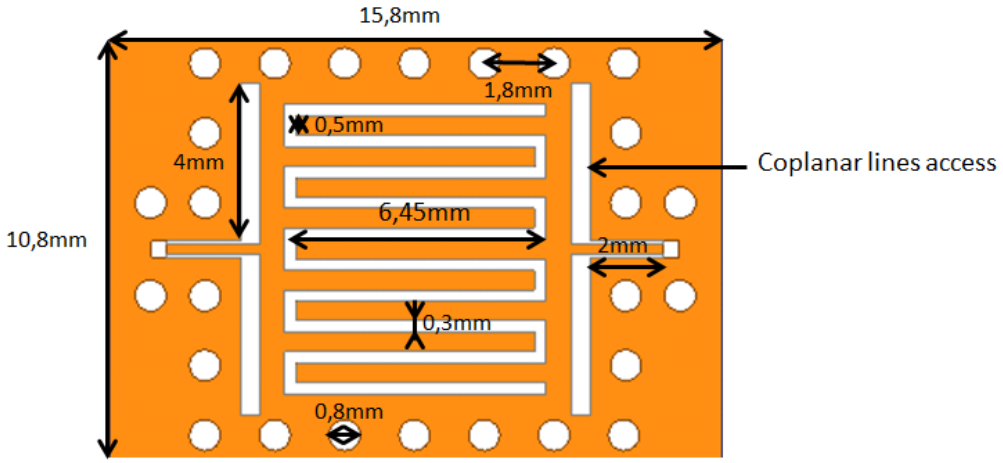

Figure 11: Design of the first generation cell

At the resonance frequency (2.5 GHz) The EM field propagates in the interdigital capacitance and goes though the substrate as seen in Figure 12. The second resonance of the structure is a parasitic frequency which comes from the interdigital capacitance itself.

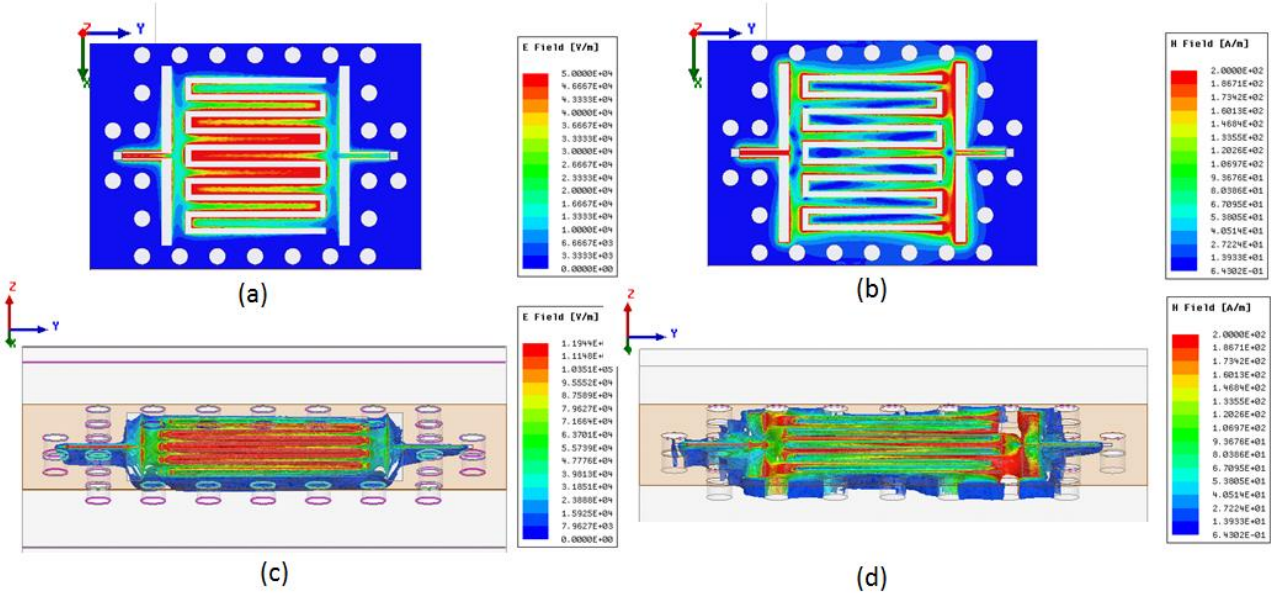

Figure 12: (a) E field in the top view, (b) H field in the top view,(c) E field in the side view,(d) H field in the side view (first resonance)

This SIW resonator was created in XLIM laboratory. The metallization was done with electroless process which is an auto-catalytic copper plating that involves simultaneous chemical reactions in an aqueous solution. The slot, the 50Ω coplanar access line and the via post were made with a laser. The measurement results of this filter are shown in Figure 13. The dimensions of the interdigital capacitance match to have a negative resonance around 2.4 GHz (with insertion loss of 1dB), as can be seen in the Figure 13. However, a parasitic resonance is also seen to exist at 3.5 GHz (with insertion loss of 0.5dB) which is considered too close to the operating frequency for any practical application. This spurious comes from the resonance of the interdigital capacitance itself but as seen in the next part it is possible to increase the resonance frequency of this resonance and therefore improving the isolation.

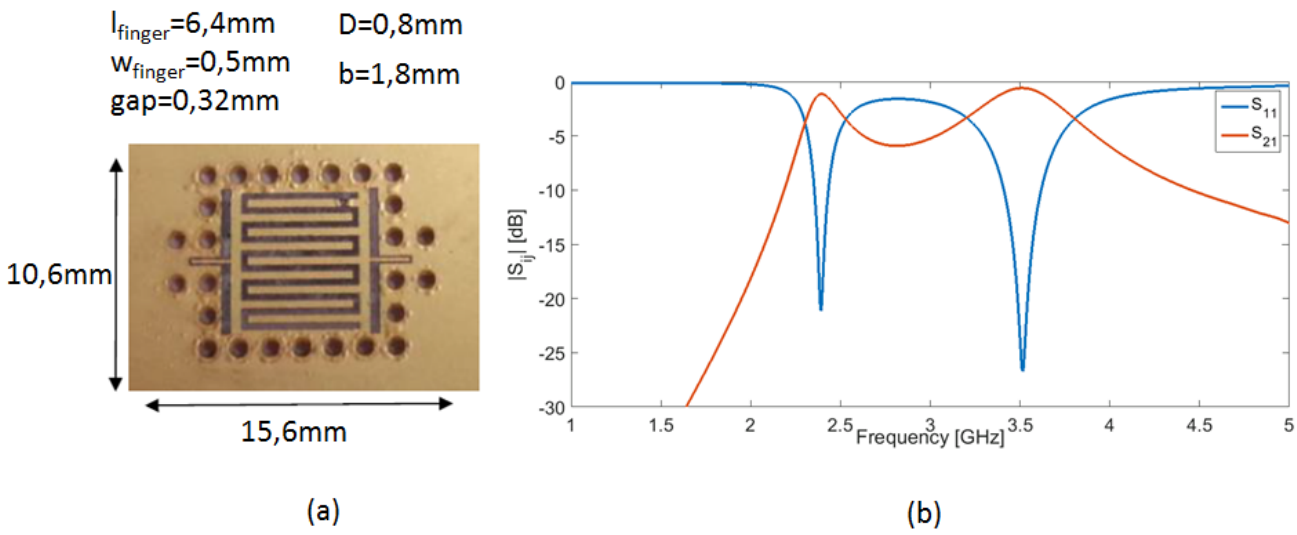

Figure 13: (a) manufactured resonator, (b) related measurement

Now the next goal is to increase the difference between the first resonance and the second which is about 1.1 GHz. With some simulations on HFSS software, the permittivity and the thickness of the substrate were found to affect the separation between the first resonance and the second one. Once again various simulations were made about exploiting the features of interdigital capacitance themselves were in order to optimize the isolation between the said resonances:

- If the width of the fingers decreases, the shift increases but the main resonance has a great insertion loss.
- If the number of fingers increases, the first resonance goes to low frequencies and the value of insertion loss is low but the coupling between those resonances is high so they are close to each other.
- If the length of the finger increases the main frequency is lower as expected and the insertion loss is good.

A tradeoff is predictable and this is why the length of the fingers is an important characteristic. Moreover, if the thickness of the substrate is too high a parasitic resonance is created and therefore deteriorates the isolation. After several simulations an optimized structure is obtained as given in Figure 14:

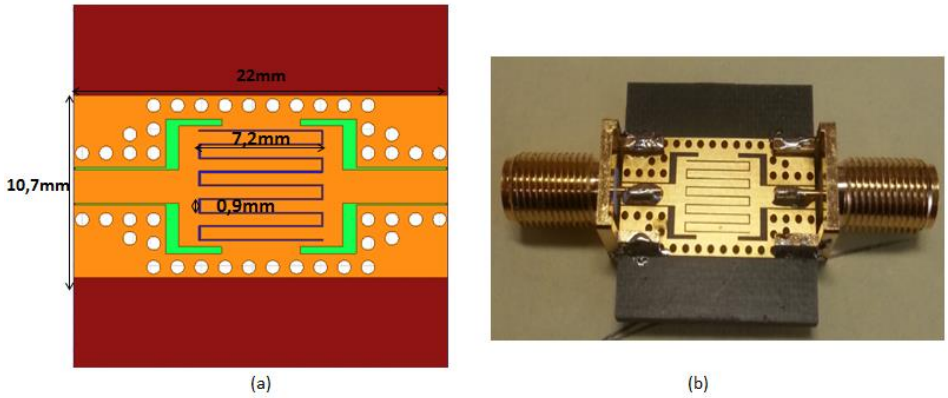

Figure 14: Final first generation elementary cell, (a) design in HFSS,(b) manufactured resonator

The elementary cell is 22mm×10.7mm with a thickness of 1.575 mm (Rogers 5880) with an ε_r of 2.2 and an associated loss tangent of 9.10-4. The length and the width of the fingers are now of 7.2mm and 0.7mm respectively. The gap of the interdigital capacitance is 100µm and the number of fingers 8. Four resonators were created and the extracted values for each one are in the Table 2. The measurement of the resonator number 1 is provided in Figure 15.

Name	f_0(measured) [GHz]	f_0(simu)[GHz]	Δf ($f_{0measured}$-f_{0simu})[MHz]	IL (measured) [dB]	Δf_{-3dB} (measured) [MHz]	Ql	Q_0 (measured)	Q_0 (simu)
Resonator 1	2.58	2.57	10	1	230	13	116	108
Resonator 2	2.58	2.57	10	1	230	13.5	115	108
Resonator 3	2.60	2.57	30	1	230	14	111	108
Resonator 4	2.61	2.57	40	1.1	230	17	113	108

Table 2: extracted values of the four SIW resonators

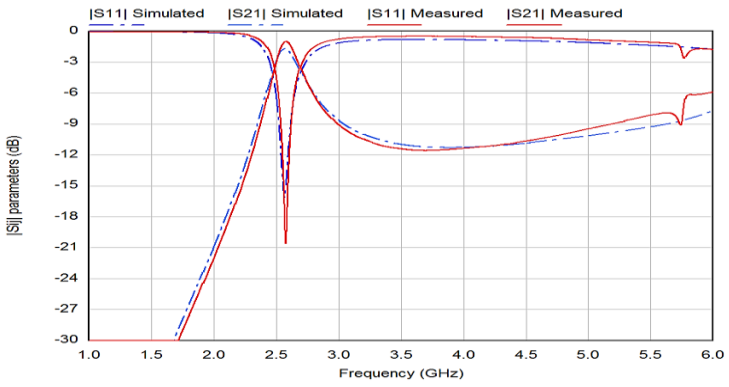

Figure 15 : Comparison between Measurement and Simulation

The four created filters matched very well with the simulation. The resonance frequency is about 2.57 GHz and the isolation is more than $2f_0$. However, the second negative resonance is still present but now at 8 GHz. The unloaded quality factor of a structure is about 116 which is higher than typical planar structures (as expected for an SIW structure). On top of that this resonator has a metallic quality factor Q_{met} (with only the metallic losses) about 274 and a dielectric quality factor Q_{diel} (with only dielectric losses) of 173. Those values come from the eigenmode of HFSS but can be verified by the theoretical formula:

$$\frac{1}{Q_0} = \frac{1}{Q_{met}} + \frac{1}{Q_{diel}} \tag{6}$$

If (6) is used, the same results are obtained then the values obtained by the eigenmode are true. It should be noted that the radiation losses are insignificant even if the resonator is not shielded and that a structure such as interdigital capacitance can radiate with specific circumstances.

2.3.2 Tunability

To study the tunability of the filter a lumped element is added with this HFSS option; in this case, it is an ideal capacitance placed on the interdigital capacitance where the E-field is close to its maximum value to have an important impact on the f_0. So the whole capacitive effect increases and tunes the resonance frequency. The S parameters are calculated with different values of the lumped element (from 0pF to 5.6pF) as seen in Figure 16.

The tuning range ($(f_{max}-f_{min})/f_{max}$) is very large here, at about 64 % as seen in Table 3. Moreover, the theoretical unloaded quality factor Q_0 for the worst case namely with 5.6 pF additional capacitance drops moderately from 121 to 61. Indeed, the higher is the capacitance, the higher are the losses and the lower is Q_0. Depending on the location of the lumped element, the field distribution changes, if the capacitance is placed far from the E-field the impact of the latter is reduced and so for having a wide tuning range a higher capacitive effect is needed.

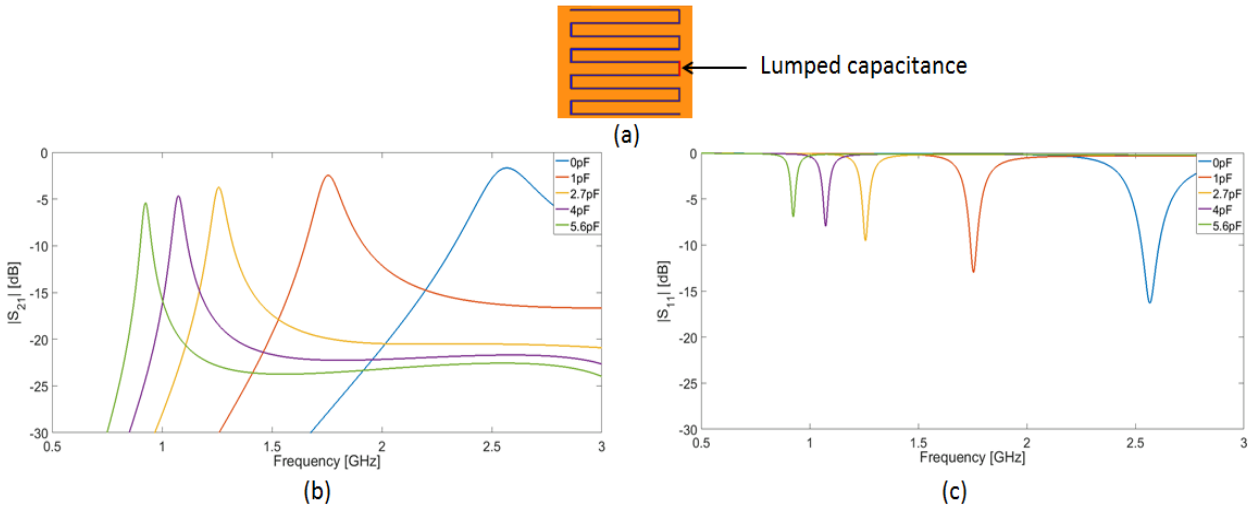

Figure 16 : (a) position of the lumped capacitance, (b) S_{21} parameters from HFSS, (c) S_{11} parameters from HFSS

Values [pF]	f_0 [GHz]	IL(simu) [dB]	Q_0(simu)
0	2.57	1.7	108
1	1.8	2.5	98
2.7	1.26	3.7	68
4	1.07	4.6	54
5.6	0.92	5.4	47

Table 3: Extracted values for the tunability study from HFSS

To study the tunability in real, surface mounted technology (SMT) capacitances are stick on both sides of the interdigital capacitance's gap with conductive Epoxy glue (Figure 17). Since the SMT elements have a metallic layer over its two ends it is possible to connect this kind of capacitance with the interdigital one. To match with the simulation the same values are chosen namely from 0pF to 5.6 pF.

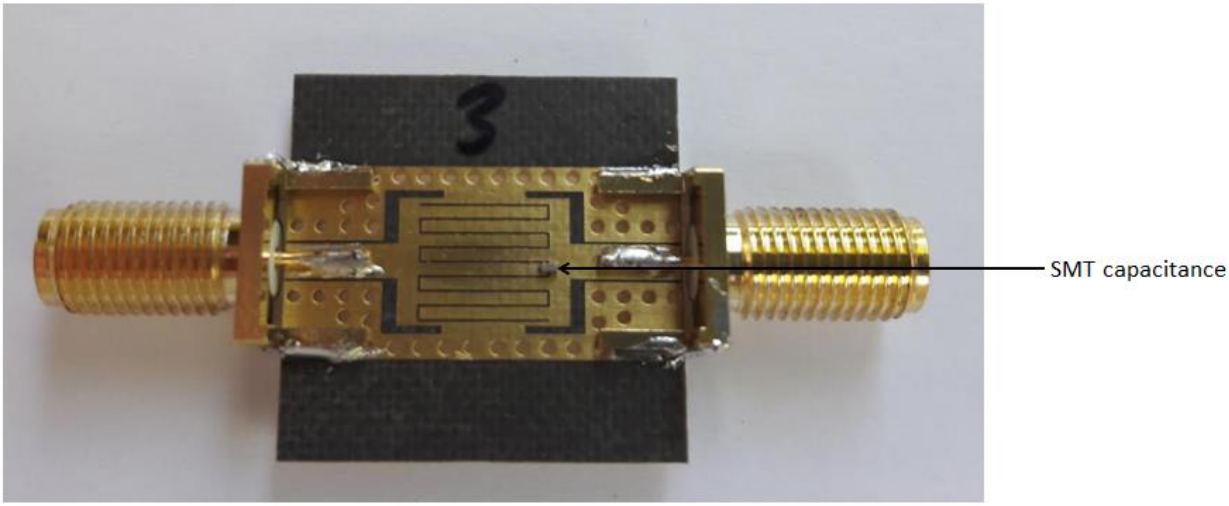

Figure 17: SIW resonator with SMT capacitance

The results show the tunability of the whole structure as seen in Figure 18. The related extracted values are in Table 4. First the tunability of the structure is confirmed and the tuning range is about 65% which is very close to the simulation as well as the resonance frequencies with a maximum difference of 20 MHz. Then, the manufacturing process is very accurate since the f_0 are almost the same and therefore the dimensions of the structure. The unloaded quality factor is about 116 for the off state and decreases to 53 with conductivity of the copper estimated around 35 S/µm. However, for the capacitance of 2.7 pF the Q_o should be higher than 63 with lower insertion loss. This difference might come from the gluing process with a bad electrical connection between the capacitor and the silver Epoxy glue.

Values [pF]	f_0(measured) [GHz]	f_0(simu) [GHz]	Δf ($f_{0measured}$-f_{0simu})[MHz]	IL(measured) [dB]	Q_0(measured)	Q_0(simu)
0	2.58	2.57	10	1	116	108
1	1.81	1.8	10	1.76	109	98
2.7	1.26	1.26	0	4.9	63	69
4	1.05	1.07	20	4.1	74	54
5.6	0.91	0.92	10	5.7	53	47

Table 4: Extracted values of the tunable SIW resonator

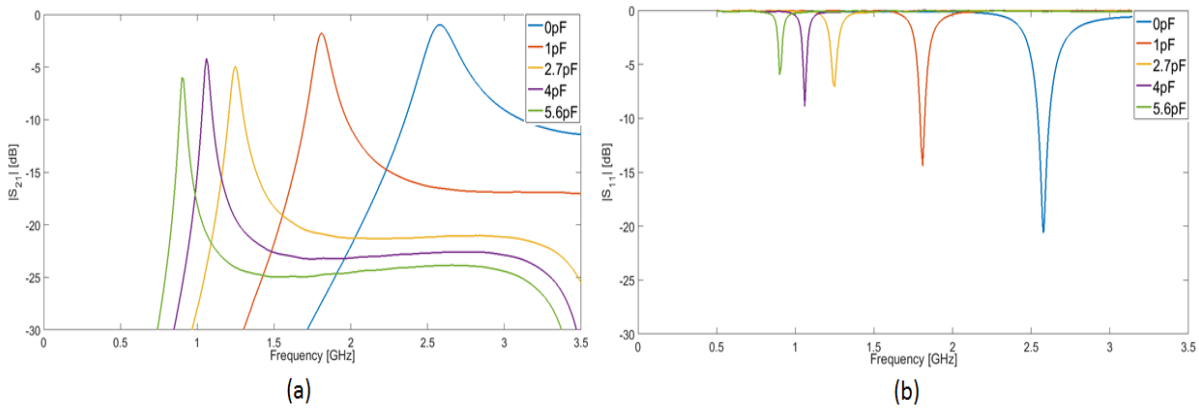

Figure 18: (a) S_{21} parameters from the measurement, (c) related S_{11} parameters

In comparison to the state of the art in the Table 1, this structure provides a very good tuning range (65%) the best compared with the others with a reasonable Q_0 (116). A comparison is made with others resonators created throughout the thesis and others from the literature in Chapter 3. The structure with its SIW nature has benefits such as: good integration, low cost, repeatable manufacturing and results. This is why this resonator is good candidate for the concept of an optically tunable filter depicted in Figure 1. So the next goal for this structure is to add a second level on which the lumped element will be set and quantify the impact of this second floor.

2.4 First generation filter with a reported SMT capacitance

To connect the first and the second level of the structure in Figure 1, an electrical junction is needed to link them up. Therefore, two vias are implemented on two fingers of the interdigital capacitance and must not touch the 100µm gap otherwise the capacitance will be short circuited and then make the metamaterial resonance frequency effect disappear. Avoiding having a classical SIW cavity the sealing process has to be accurate to connect 0.8mm diameter vias with 0.9mm width interdigital capacitance's fingers without touching the gap. For the same purpose the second substrate which is the same than the first one namely Rogers 5880 has a backside without any metallization. To allow us using the sealing process created by LITHOS company the ratio between the thickness of the substrate (for the second floor, in our case 0.5mm) and the diameter of the via has to be lower than one. The glue used for this process has a relative permittivity of 2.7 with a loss tangent of 2.10^{-3} which shifts the resonance frequency of the whole structure since the glue is between the fingers

instead of air. The new f_0 is lower than before because the capacitance is now about 1.4 pF (0.78pF before). Moreover, adding a second substrate means to cover a part of the coplanar excitation lines and therefore increase the shift of f_0 to lower frequencies. The top layer of the second substrate is etched to have only microstrip lines connected to the electrical vias and a gap between them on which the SMT capacitance is glued. Two 1.2mm diameter metallic circles are added on the top layer to ensure the good electrical connection between via holes and the microstrip line. The first floor does not change: coplanar excitation lines have the same dimensions as well as the vias (SIW cavity) with a diameter of 0.8mm. The new entire structure is depicted in Figure 19.

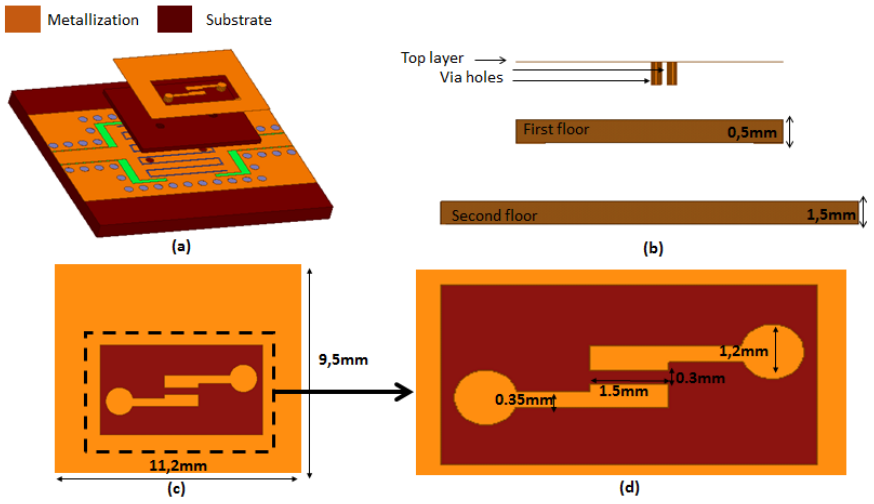

Figure 19: (a) exploded view, (b) front view, (c) top view of the second substrate, (d) zoomed top view

Five resonators were created thanks to the sealing process. All the extracted values from the measurements for the five resonators are in Table 5. The results show a good match with the simulation with a highest difference (Δf) of 50 MHz (Figure 20). This slight change might come from the variation of interdigital capacitance's dimensions (fingers length, width, gap) and/or that the relative permittivity of the glue is not exactly 2.7. The insertion loss for the best case (resonator number 3) are very close to the ones from the previous part (Table 2) as well as the unloaded quality factor. Then, adding a second level does not have a significant impact to the performance of the whole structure with this sealing process and at the useful frequency bands (S and L bands). Therefore, it is possible to think of creating more complex structures with different levels with their proper function such as resonator, tuning elements,

antennas and so on (with the constraint of the design rules related to the sealing process of course).

Name	$f_{0(measured)}$ [GHz]	$f_{0(simu)}$[GHz]	Δf ($f_{0measured}$-f_{0simu})[MHz]	IL [dB]	Δf_{-3dB} [MHz]	Ql	Q_0 (measured)	Q_0 (simu)
Resonator 1	2.09	2.14	50	1.25	130	16	109	107
Resonator 2	2.09	2.14	50	1.1	130	16	115	107
Resonator 3	2.10	2.14	40	1.07	130	16	116	107
Resonator 4	2.10	2.14	40	1.26	131	16	109	107
Resonator 5	2.10	2.14	40	1.13	131	16	111	107

Table 5: Extracted values for the five resonators

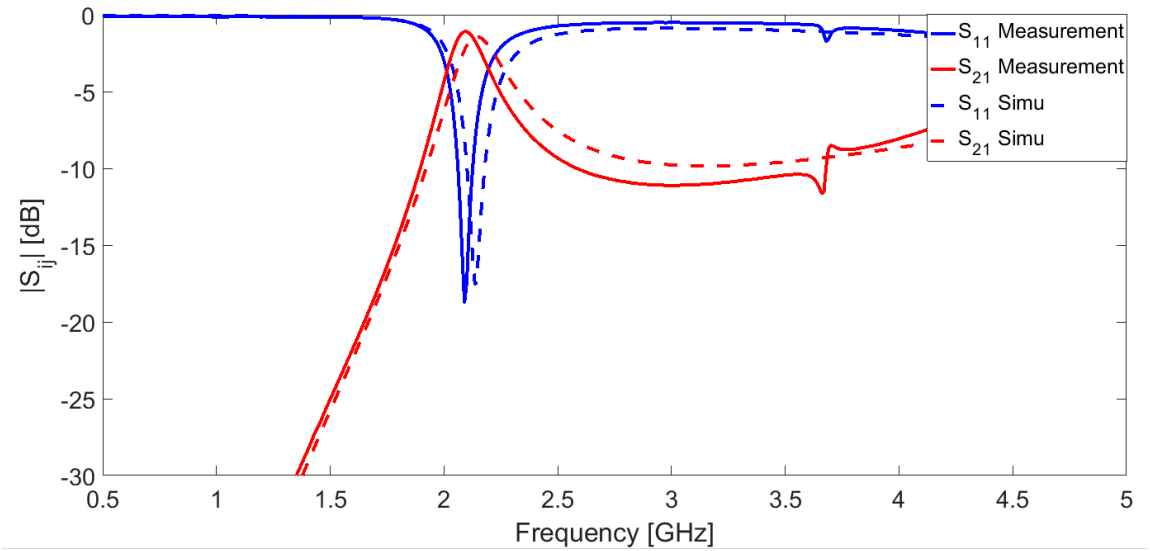

Figure 20: Comparison between simulation and measurement (resonator 2)

For the tunability study, the same method is used as the previous section namely an SMT capacitance is placed over the 1.5mm×0.8mm gap depicted in Figure 19. A simulation was done for a variation of the capacitance values from 0pF to5.6 pF as seen in Figure 21. For the same extreme values namely 0pF and 5.6pF the tuning range is 65% i.e. the same as before (Table 6). Moreover the unloaded quality factor is quite the same compared with the values from Table 3 with a change from 107 to 51. This feature is emphasized by the evolution of the insertion loss which is comparable with Table 3. It should be noted that the parasitic resonance of the interdigital capacitance is affected by the additional capacitance effect (Figure 21), but the isolation is still higher than $2f_0$ and the f_0 of this spurious resonance does not seem to go lower than 2.8GHz.

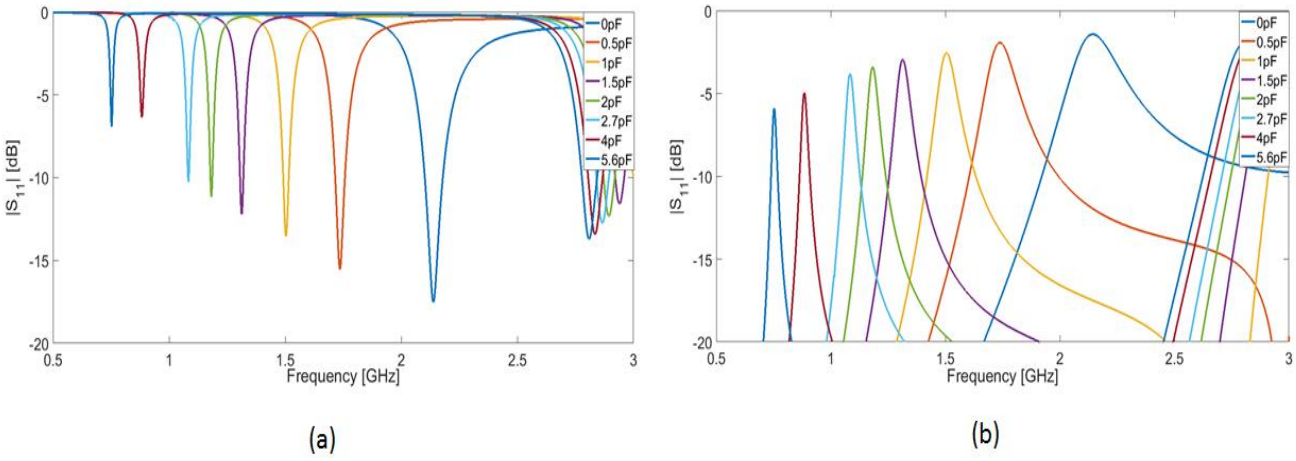

Figure 21: Simulation for different capacitance values, (a) S_{11} parameters, (b) S_{21} parameters

Values [pF]	f_0(simu)[GHz]	IL [dB]	Δf_{-3dB} [MHz]	$Q_{0\ (simu)}$
0	2.14	1.1	264	107
0.5	1.74	1.5	150	101
1	1.5	2.1	96	92
1.5	1.31	2.6	71	84
2	1.18	3.1	51	82
2.7	1.08	3.4	43	78
4	0.88	4.6	30	64
5.6	0.76	5.9	22	51

Table 6: Extracted values from HFSS of the resonators with reported SMT capacitances

As said previously, the SMT capacitance is placed over the gap between the microstrip lines as illustrated in Figure 22. Contrary to the simulation on HFSS, the different values of capacitance are from 0pF to 2pF for the measurements due to lack of time. All the results are in Table 7. The same conclusions as previously made are pointed out: the measurements are close to the simulation in terms of resonance frequency with a highest shift of 50 MHz, unloaded quality factor and insertion loss. The tuning range until 2pF is about 45% which is the same as HFSS simulations. Since the measured tunability of the previous structure (Figure 17) and the simulated are the same, it is possible to think that the new structure (Figure 22) might have the same tuning range than the simulation (Table 6), even if the measurements stop at 2pF, which is about 65%. The measurements of the S parameters are depicted in Figure 23.

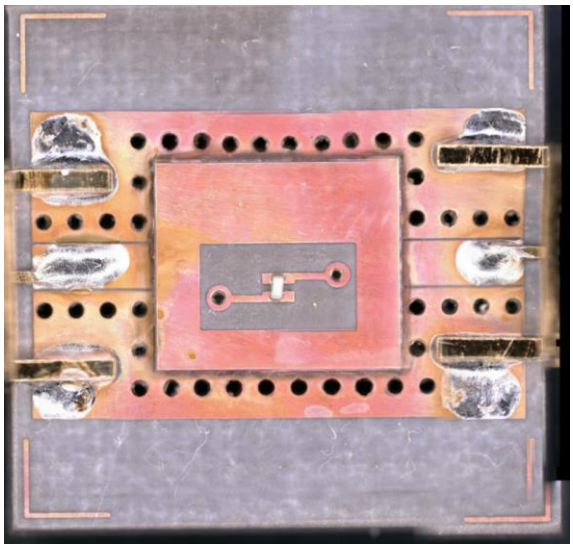

Figure 22: manufactured SIW resonator with a reported SMT capacitance

Values [pF]	f_0(measured) [GHz]	f_0(simu)[GHz]	Δf ($f_{0measured}$-f_{0simu})[MHz]	IL [dB]	Δf_{-3dB} [MHz]	Ql	Q_0 (measured)	Q_0 (simu)
0	2.09	2.14	50	1.1	131	16	115	107
0.5	1.70	1.74	40	1.43	106	16	107	101
1	1.50	1.50	0	2	83	18	98	92
1.5	1.30	1.31	10	2.7	54	24	91	84
2	1.14	1.18	40	3.2	42	27	86	82

Table 7: Extracted values of measurements for resonators with reported capacitances from 0pF to 2pF

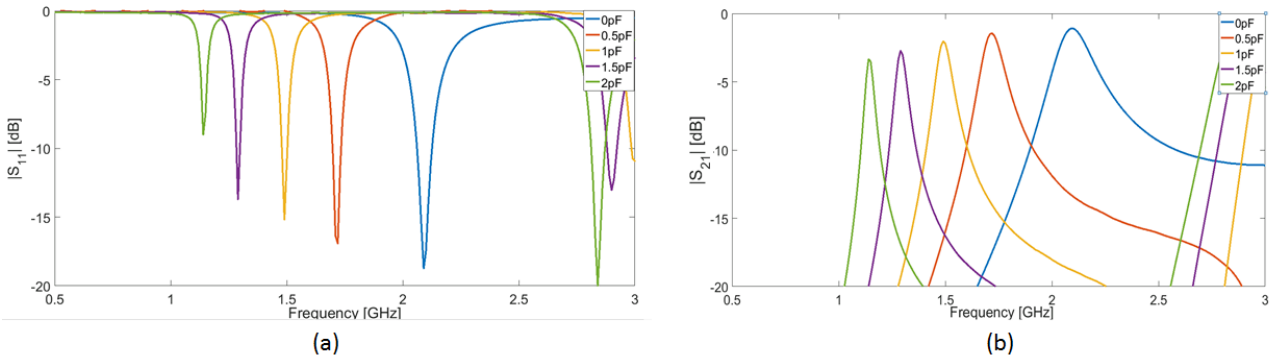

Figure 23: S parameters of the resonator with a reported capacitance, (a) S_{11}, (b) S_{21}

2.5 Conclusion

In order to fulfill the purpose illustrated in Figure 1 a SIW based resonator has been created in this chapter. This unit cell has an unloaded quality factor of 116 for the best case (Table 2) with an interesting tuning range of 65% which is the best among the publications in the Table 1 and it has another very interesting features explained in the Chapter 3 (3.6 section) which is the size /tuning range ratio.

Moreover, in order to predict the impact of the second layer, a suitable sealing process for our frequency bands application has been tried. Indeed, the effects on the unloaded quality factor are insignificant by comparing Table 4 and Table 7. The tuning range is not affected by the addition of the second "floor" (65%) since it is same as the structure without the additional level (64%) even if the measurements done are for capacitance values from 0pF to 2pF (Table 7) and not from 0pF to 5.6pF (Table 6). Indeed throughout this chapter the results from simulations match very well with measurements so based on that it is possible to extrapolate that the tuning range in reality might be same as the one from HFSS.

The "LEGO" like structure can be created with the sealing process used in this chapter and others levels with their own purpose (resonator, tuning method, antennas and so on) can be implemented to form a compact configuration with different functions. However, in this thesis only the first (resonator) and the second level (tuning elements) have been investigated. Even if the created resonator has interesting features such as its size and tuning range, the next goal is to design and manufacture another elementary cell with higher unloaded factor with a good compactness. Indeed, with a Q_0 of 116 and lossy tuning elements such as switches the purpose of the resonator can be deteriorated. So having a new elementary cell with a higher Q_0 allows us to create a system whose the impact of losses are minimized. The next chapter deals with explaining and designing this novel resonator.

2.6 Bibliography

[1] D. Deslandes and K. Wu, “Integrated microstrip and rectangular waveguide in planar form,” *IEEE Microw. Wirel. Compon. Lett.*, vol. 11, no. 2, pp. 68–70, Feb. 2001.

[2] M. Bozzi, A. Georgiadis, and K. Wu, “Review of substrate-integrated waveguide circuits and antennas,” *IET Microw. Antennas Propag.*, vol. 5, no. 8, pp. 909–920, Jun. 2011.

[3] D. Deslandes and K. Wu, “Single-substrate integration technique of planar circuits and waveguide filters,” *IEEE Trans. Microw. Theory Tech.*, vol. 51, no. 2, pp. 593–596, Feb. 2003.

[4] D.-D. Zhang, L. Zhou, L.-S. Wu, L.-F. Qiu, W.-Y. Yin, and J.-F. Mao, “Novel Bandpass Filters by Using Cavity-Loaded Dielectric Resonators in a Substrate Integrated Waveguide,” *IEEE Trans. Microw. Theory Tech.*, vol. 62, no. 5, pp. 1173–1182, May 2014.

[5] G. Q. Luo, Z. F. Hu, L. X. Dong, and L. L. Sun, “Planar Slot Antenna Backed by Substrate Integrated Waveguide Cavity,” *IEEE Antennas Wirel. Propag. Lett.*, vol. 7, pp. 236–239, 2008.

[6] A. Pourghorban Saghati, M. M. Mirsalehi, and M. H. Neshati, “A HMSIW Circularly Polarized Leaky-Wave Antenna With Backward, Broadside, and Forward Radiation,” *IEEE Antennas Wirel. Propag. Lett.*, vol. 13, pp. 451–454, 2014.

[7] Y. Cassivi and K. Wu, “Low cost microwave oscillator using substrate integrated waveguide cavity,” *IEEE Microw. Wirel. Compon. Lett.*, vol. 13, no. 2, pp. 48–50, Feb. 2003.

[8] K. Entesari, A. P. Saghati, V. Sekar, and M. Armendariz, “Tunable SIW Structures: Antennas, VCOs, and Filters,” *IEEE Microw. Mag.*, vol. 16, no. 5, pp. 34–54, Jun. 2015.

[9] F. Giuppi, A. Georgiadis, A. Collado, M. Bozzi, and L. Perregrini, “Tunable SIW cavity backed active antenna oscillator,” *Electron. Lett.*, vol. 46, no. 15, pp. 1053–1055, Jul. 2010.

[10] M. Armendariz, V. Sekar, and K. Entesari, “Tunable SIW bandpass filters with PIN diodes,” in *Microwave Conference (EuMC), 2010 European*, 2010, pp. 830–833.

[11] V. Sekar, M. Armendariz, and K. Entesari, “A 1.2 #x2013;1.6-GHz Substrate-Integrated-Waveguide RF MEMS Tunable Filter,” *IEEE Trans. Microw. Theory Tech.*, vol. 59, no. 4, pp. 866–876, Apr. 2011.

[12] S. Sirci, J. D. Martinez, M. Taroncher, and V. E. Boria, “Varactor-loaded continuously tunable SIW resonator for reconfigurable filter design,” in *Microwave Conference (EuMC), 2011 41st European*, 2011, pp. 436–439.

[13] K. Entesari, A. P. Saghati, V. Sekar, and M. Armendariz, “Tunable SIW Structures: Antennas, VCOs, and Filters,” *IEEE Microw. Mag.*, vol. 16, no. 5, pp. 34–54, Jun. 2015.

[14] S. Sirci, J. D. Martinez, M. Taroncher, and V. E. Boria, “Analog tuning of compact varactor-loaded combline filters in substrate integrated waveguide,” in *Microwave Conference (EuMC), 2012 42nd European*, 2012, pp. 257–260.

[15] S. Adhikari, Y.-J. Ban, and K. Wu, “Magnetically Tunable Ferrite Loaded Substrate Integrated Waveguide Cavity Resonator,” *IEEE Microw. Wirel. Compon. Lett.*, vol. 21, no. 3, pp. 139–141, Mar. 2011.

[16] S. Adhikari, A. Ghiotto, and K. Wu, “Simultaneous electric and magnetic two-dimensional tuning of substrate integrated waveguide cavity resonator,” in *Microwave Symposium Digest (MTT), 2012 IEEE MTT-S International*, 2012, pp. 1–3.

[17] S. Adhikari, A. Ghiotto, and K. Wu, “Simultaneous Electric and Magnetic Two-Dimensionally Tuned Parameter-Agile SIW Devices,” *IEEE Trans. Microw. Theory Tech.*, vol. 61, no. 1, pp. 423–435, Jan. 2013.

[18] S. Sirci, J. D. Martinez, and V. E. Boria, “Low-loss 3-bit tunable SIW filter with PIN diodes and integrated bias network,” in *Microwave Conference (EuMC), 2013 European*, 2013, pp. 1211–1214.

[19] F. Mira, J. Mateu, and C. Collado, “Mechanical Tuning of Substrate Integrated Waveguide Resonators,” *IEEE Microw. Wirel. Compon. Lett.*, vol. 22, no. 9, pp. 447–449, Sep. 2012.

[20] A. Anand, J. Small, D. Peroulis, and X. Liu, “Theory and Design of Octave Tunable Filters With Lumped Tuning Elements,” *IEEE Trans. Microw. Theory Tech.*, vol. 61, no. 12, pp. 4353–4364, Dec. 2013.

[21] “Substrate Integrated Waveguide Based Metamaterial Components,” Univeristy of California, Los Angeles, 2012.

[22] R. A. Shelby, D. R. Smith, and S. Schultz, “Experimental Verification of a Negative Index of Refraction,” *Science*, vol. 292, no. 5514, pp. 77–79, Apr. 2001.

[23] C. Caloz and T. Itoh, *Electromagnetic Metamaterials: Transmission Line Theory and Microwave Applications*. John Wiley & Sons, 2005.

[24] R. Marqués, J. Martel, F. Mesa, and F. Medina, “Left-Handed-Media Simulation and Transmission of EM Waves in Subwavelength Split-Ring-Resonator-Loaded Metallic Waveguides,” *Phys. Rev. Lett.*, vol. 89, no. 18, p. 183901, Oct. 2002.

[25] D. M.Pozar, *Microwave Engineering, 3Rd Ed*. Wiley India Pvt. Limited, 2009.

[26] S. Hrabar, J. Bartolic, and Z. Sipus, “Waveguide miniaturization using uniaxial negative permeability metamaterial,” *IEEE Trans. Antennas Propag.*, vol. 53, no. 1, pp. 110–119, Jan. 2005.

[27] Y. Dong and T. Itoh, “Miniaturized Substrate Integrated Waveguide Slot Antennas Based on Negative Order Resonance,” *IEEE Trans. Antennas Propag.*, vol. 58, no. 12, pp. 3856–3864, Dec. 2010.

[28] K. Wu, D. Deslandes, and Y. Cassivi, “The substrate integrated circuits - a new concept for high-frequency electronics and optoelectronics,” in *6th International Conference on Telecommunications in Modern Satellite, Cable and Broadcasting Service, 2003. TELSIKS 2003*, 2003, vol. 1, p. P-III-P-X vol.1.

Chapter 3:

Alumina

Bandpass filter

3.1 Introduction

The previous chapter has deal with SIW structures and more particularly with resonators filters by introducing different type of tuning methods and their associated performances such as unloaded quality factor Q_0 and tuning range. The first developed elementary cell has a really interesting tuning range of 63% (measured results) but a standard quality factor (with SIW technology) of 110. As a result, a new cavity-based structure is developed in order to reach higher Q_0 by using a capacitive loading with a central post and on annular gap. On top of that, the substrate used for this SIW-like structure is Alumina based with a really low loss tangent which is essential for making a high Q resonator.

The use of such structure is interesting for our "Lego-like" (Figure 1) application since the second level which contains the tuning elements (switches and capacitances) may be very lossy depending on the features of the switches themselves and of the necessary elements for the electrical connection between the leve1 and 2 (electrical vias, metallic glue and so on). Even though the Q_0 will significantly decreases, this one will be high enough for studying the tunability of the cavity described in the next part and for demonstrating the optically tunable cavity concept.

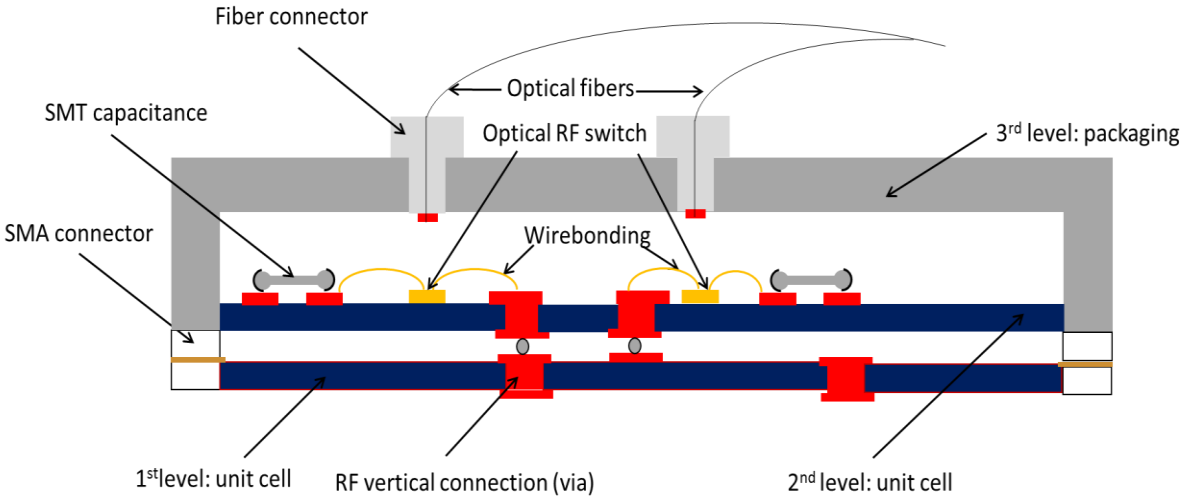

Figure 1: Block diagram for the concept of an optically tunable filter

Firstly, this chapter depicts the well-known theory behind the chosen cavity, its parameters and performances. Then, a compact cavity is investigated as well as second third

and fourth order bandpass filters. A study of its tunability will be made as well as a possible solution for connecting the level 1 and the level 2 (Figure 1). A comparison with tunable filters and resonators found in the literature will also be provided.

3.2 Concept

3.2.1 Cavity

For applications at frequencies higher than 1 GHz, the need of metallic cavity for limiting losses is desirable. A cavity resonator can be considered as volume boundaries with metallic walls in which an EM filed might be excited. This structure can be associated with another cavity or a waveguide thanks to an iris or a slit to create a coupling with it. In general, two types of resonant cavities are used namely a rectangular cavity or a cylindrical one. This chapter only talks about rectangular cavity illustrated in Figure 2.

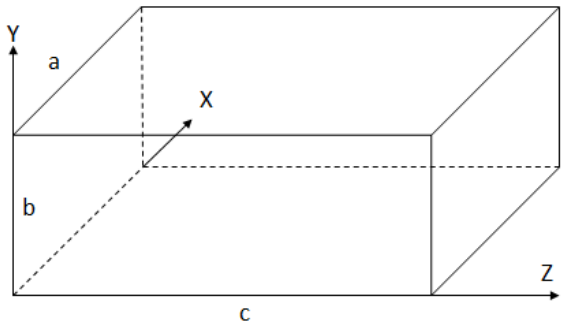

Figure 2 : rectangular cavity

The Figure 2 represents a rectangular cavity with *a* for the width, *b* for the height and *c* for the length. The possible resonant modes of the cavity are called the eigenmodes: TE_{mnp} and TM_{mnp} (with $_{m,n,l}$ being the mode numbers corresponding to the dimensions a,b ,c). The guided wavelength λ_g depends on n and m of the TE_{mn} or TM_{mn} modes [1].

$$\frac{1}{\lambda} = \left[\left(\frac{1}{\lambda_c^2}\right)_{mn} + \left(\frac{1}{\lambda_g^2}\right)_{mn}\right]^{\frac{1}{2}} \quad (1)$$

Then :

$$\lambda_{mnp} = \left[\left(\frac{1}{\lambda_c^2}\right)_{mn} + \left(\frac{p}{2c}\right)^2\right]^{-\frac{1}{2}} \quad (2)$$

Hence:

$$f_{mnp} = \upsilon\left[\left(\frac{1}{\lambda_c^2}\right)_{mn} + \left(\frac{p}{2c}\right)^2\right]^{-\frac{1}{2}} \quad (3)$$

With $\upsilon = \frac{c}{\sqrt{\varepsilon_r}}$

Then, to know the resonant frequencies of a metallic rectangular cavity filled with a dielectric, the following formula has to be applied:

$$f_{mnp} = \frac{c}{2\pi\sqrt{\varepsilon}_r}\sqrt{\left(\frac{m\pi}{a}\right)^2 + \left(\frac{n\pi}{b}\right)^2 + \left(\frac{p\pi}{c}\right)^2} \quad (4)$$

For the purpose of this thesis, the resonator has to be designed and made tunable in order to cover the L and S bands, respectively 1-2 GHz and 2-4 GHz. On top of that for reaching high Q_0 and good compactness, the chosen substrate for this application is made of Alumina with a relative permittivity (ε_r) of 8.7 and a loss tangent of 1.10^{-4} at 10 GHz.

Thanks to (4) it is easy to find the right dimensions for designing a cavity in HFSS. The finite element method used by HFSS to solve eigenvalue problems attests to the good design of the cavity. Since a 2mm thick Alumna substrate is used, the TE_{101} mode is obtained around 2.45 GHz with a 27x32 mm². Typical Q_0 factor using a metallization of the Alumina resonator having a conductivity of 20 S/µm is around 370 as seen in Figure 3. It should be noted that the Q_0 is higher with Alumina substrate than the previous structure introduced in the Chapter 2.

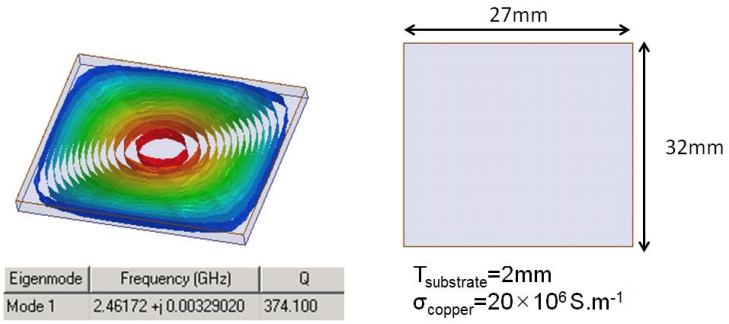

Figure 3: Dimensions of the cavity and its associated fundamental mode

3.2.2 Rectangular shaped gap

3.2.2.1 Dimensions

To integrate the resonator in a tunable multilayer/level structure (Figure 1), a rectangular shaped gap is etched in the metallic layer (at the surface of the substrate) and slightly into the dielectric layer (Figure 4). Therefore, by adding a capacitive effect (varactor, SMT capacitance) over this gap a frequency shifting of the resonance can be observed [2] since it is located close to the maximum of the E-field. The resonator tunability principle is the same as the one depicted in the previous chapter. The main advantage of this sort of gap is the suitability for surface mounted component as shown in [2]. On top of that, the resonant frequency and the tuning range are independent of fabrication and assembly tolerance since the addition of the capacitive effect is created by SMT components.

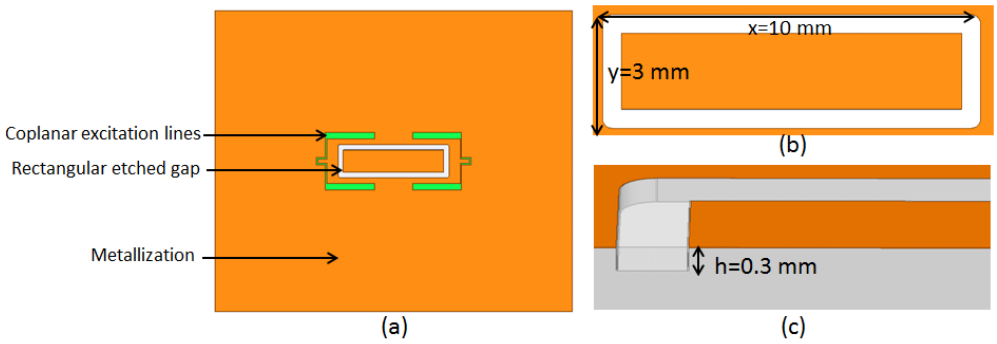

Figure 4: Rectangular shaped gap: (a) top view, (b) zoomed top view to the center, (c) zoomed view of the gap depth

The rectangular shaped gap's dimensions are studied to quantify its influence on the added capacitive effect. A resonator is modelled as a series RLC circuit with a frequency resonance, f_0 such as:

$$f_0 = \frac{1}{2\pi\sqrt{LC}} \tag{5}$$

The inductance is fixed at 1nH, so the equivalent capacitance for the resonator depicted in Figure 3 is 4.32 pF. Thanks to HFSS, the f_0 for each resonator with different dimensions of the gap is simulated and computed. The impact of three main parameters namely the length, the width and the heigth of the groove are investigated and reported in the Table 1.

	Parameters [mm]	f0 [GHz]	Capa [pF]
h [mm] (with x=10mm y=3mm)	0	2.47	0
	0.01	2.47	0.02
	0.1	2.46	0.04
	0.2	2.45	0.08
	0.3	2.44	0.12
	0.4	2.41	0.18
x [mm] (with y=3mm h=0.2mm)	6	2.49	0
	8	2.48	0.02
	9	2.47	0.04
	10	2.45	0.08
	11	2.42	0.18
	12	2.41	0.22
y [mm] (with x=10mm h=0.2mm)	2	2.47	0
	3	2.45	0.08
	4	2.42	0.23
	5	2.39	0.34
	6	2.37	0.43
	7	2.33	0.64

Table 1: Computed capacitances according to the gap's parameters (see Figure 4)

The variation of the dimensions has an effect on the capacitive effect as well as f_0 and more particularly the y dimension. However, these changes do not have significant influence

as we thought first but can be useful if the need of a fine tuning is required. The dimensions shown in the Figure 4 are chosen in order to have a resonance frequency around 2.45 GHz i.e. x=10mm, y=3mm and h=0.2mm.

3.2.2.2 Coplanar excitation lines

This type of access is chosen due to the arrangement of the EM fields associated with the fundamental mode TE_{101} according to [3] [4] . Fabricating this excitation lines is easy thanks to an etching of the top metallization with a laser beam and allow an easy characterization of resonators with appropriate Ground-Signal-Ground (GSG) probes. Due to the fact tha the lines are short circuited, the EM filed is concentrated at its ends. Therefore external couplings (Q_e) are tuned by changing the dimensions and the location of the pattern. Q_e represents the coupling between the excitation system and the excited cavity mode.

The method to quantify this parameter consists in simulating the structure with no losses and therefore the Q_0 is infinite. The equation (3) of the first chapter becomes:

$$\frac{1}{Q_l} = \frac{1}{Q_{e1}} + \frac{1}{Q_{e2}} \tag{6}$$

With $Q_{e1}=Q_{e2}$ since the excitation lines are the same

$$Q_l = \frac{Q_e}{2} \tag{7}$$

The coupling factor Q_l is computed thanks to (8).

$$Q_l = \frac{f_0}{\Delta f_{-3dB}} \tag{8}$$

The loaded quality factor can be computed with the S_{11} parameter. The f_0 is measured corresponding to a phase shifting on the S_{11} parameter as well as the frequencies $f_{0\text{-}90°}$ and $f_{0+90°}$. Then, the equation (8) is used with a new Δf (Figure 5) and Q_e can be determined.

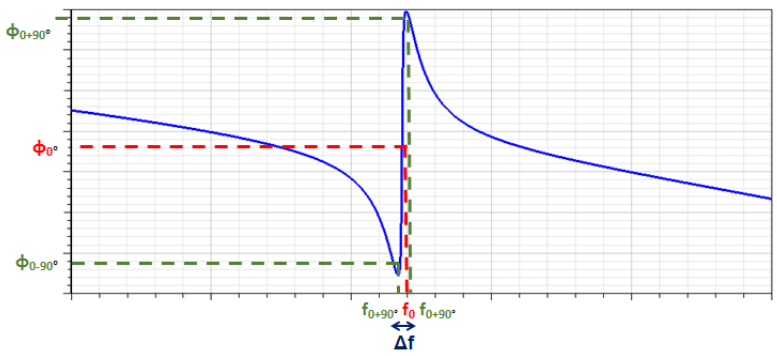

Figure 5: Phase of the S_{11} parameter.

The dimensions of the gap (0.15 µm) and the central conductor (0.35 µm) of these coplanar lines are designed to be suitable with 500µm pitch GSG probes equipment.

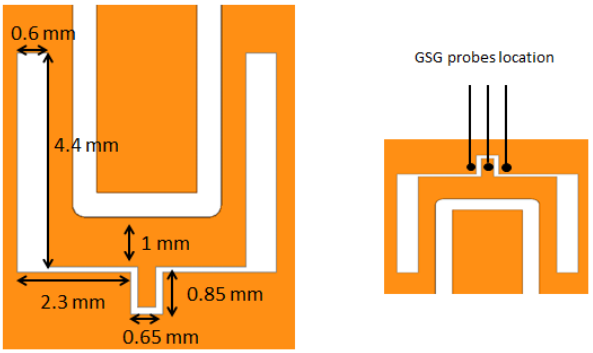

Figure 6: Dimensions of the coplanar lines

The driven modal simulation with HFSS is illustrated in Figure 7 the f0 is 2.46 GHz wit insertion loss of 0.7dB for a Q_e of 23.

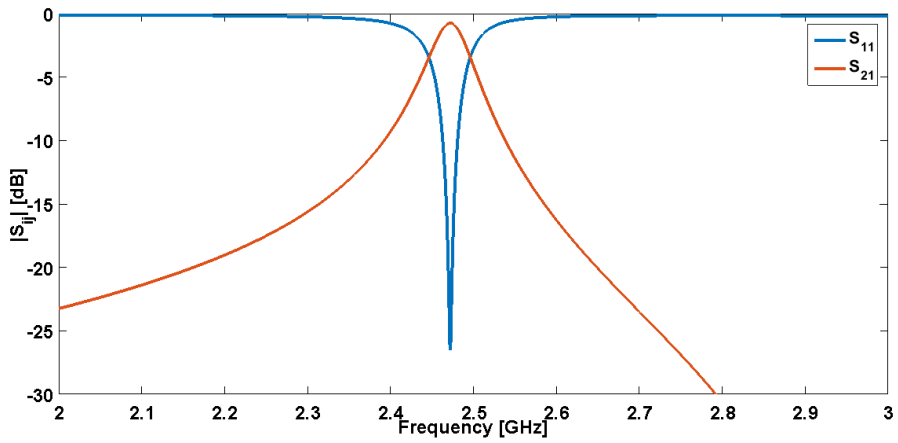

Figure 7: S parameters of the structure with the rectangular etched gap

3.2.2.3 Tunability

For studying this aspect the same method is used as in the previous chapter: we just connect an ideal capacitance over the rectangle etched gap (close to the maximum of the E-field) and we study how evolve the S parameters. A lumped element is placed as seen in the Figure 8 and each S_{21} parameter is simulated for different values of capacitance from 0 pF to 3 pF.

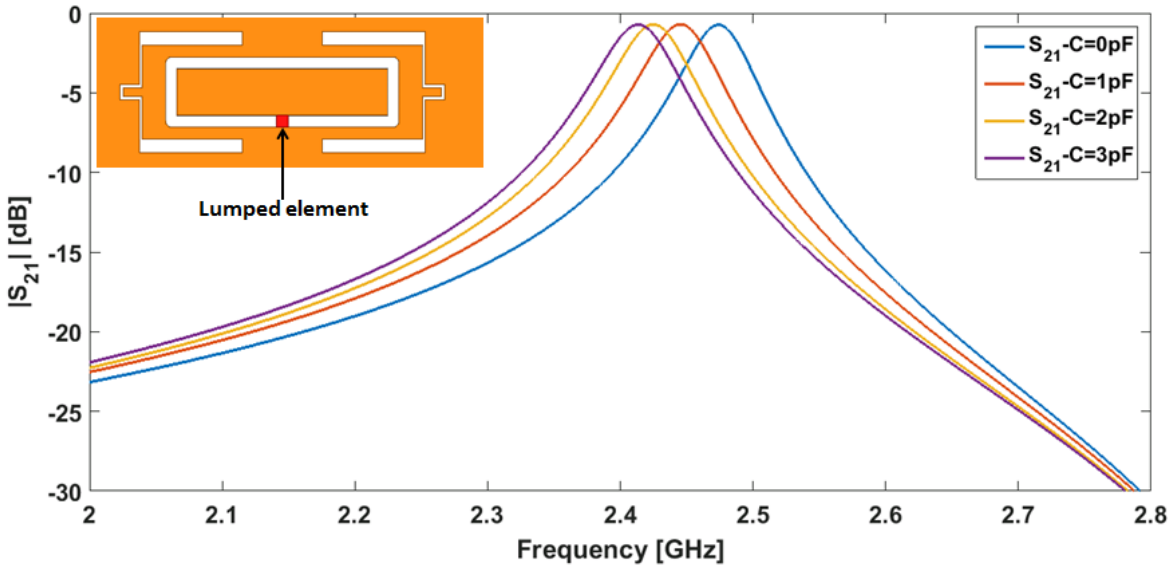

Figure 8: S_{21} parameters for different values of capacitances

The tuning range is low (<5%) which is too small for a proper tunable application because the resonator frequency changes from 2.46 GHz to 2.42 GHz when an extra 3pF capacitor is used. However, it is possible to increase the tunability by changing the previous structure into an evanescent mode resonator.

3.2.3 Cavity-loading technique

3.2.3.1 Approach

An evanescent mode resonator can be constructed by inserting a metallic obstacle such as a post in the middle of the cavity. This well-known technique was presented first by Craven and Mok [5] and has resulted in a whole generation of hand-tuned filter in the 1970s

until today [6]–[10]. This technology has several names in the literature such as coaxial or combline resonators. The main advantages of a loaded resonator are:

- Miniaturization: the metallic post in the middle of the cavity creates a strong parallel plate capacitor between the top of the loading element and the cavity wall. Therefore, the cutoff frequency of the fundamental mode TE_{101} shifts to a lower frequency.
- Tuning: the post allows a high concentration of the electric field in a small area (above metallic post and underneath the cavity wall). Therefore, a tuning element can be inserted and can greatly influence the resonant frequency. For example a microelectromechanical systems (MEMS) diaphragm is used to reach [6] a 4:1 tuning range (from 6 to 24 GHz).
- Wide spurious free range: in [10] loaded resonators demonstrate a 17:1 spurious free range while the spurious free range of a typical unloaded cavity resonator is less than 2:1 [11].

A 7.2×1×1.8 mm^3 metallic post is inserted inside the previous structure. As seen in Figure 9 an electric field is set between the top of the post and the cavity wall, the value of the created capacitance depends on the height of the dielectric medium.

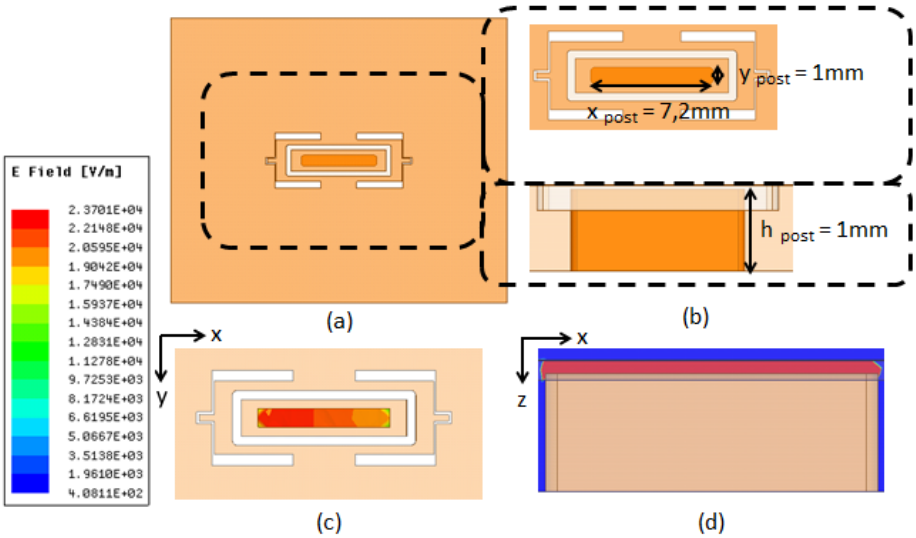

Figure 9: Dimensions of the capacitive post: (a) top view, (b) zoomed views, (c)side view- and the related E-field: (c) top view, (d) zoomed side view to the metallic post.

Thanks to the E field concentrated near the capacitive post, a correct tuning range can be reached when a SMT capacitance is added. As previously in order to study this aspect an ideal lumped element (with a changing capacitance value) is added over the 500 µm wide gap of the structure (Figure 10).

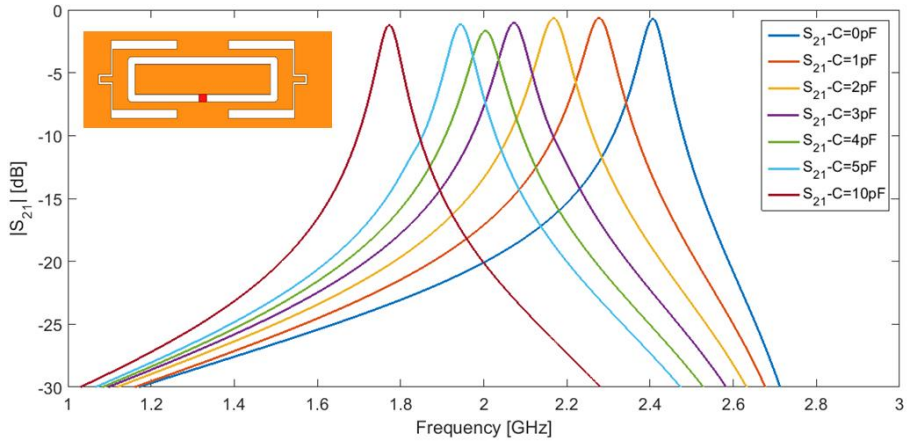

Figure 10: Ideal tunability of the loaded cavity

From 0pF to 3pF the tuning range is now of 17% which is higher than with the previous resonator (5% without the post). As seen in Figure 10 the tuning range can be wider namely 27% from 0pF to 10pF (after 10pF the resonant frequency of the structure is still very close to 1.76 GHz). On top of that the tunability depends on the height of the post (h_{post}): the higher the post is, the wider the tuning range is as depicted in Figure 11. Indeed, the capacitive value created by the post is stronger for a smaller gap between the top of the post and the cavity walls. A small gap thus increases the effect of the lumped elements (capacitances).

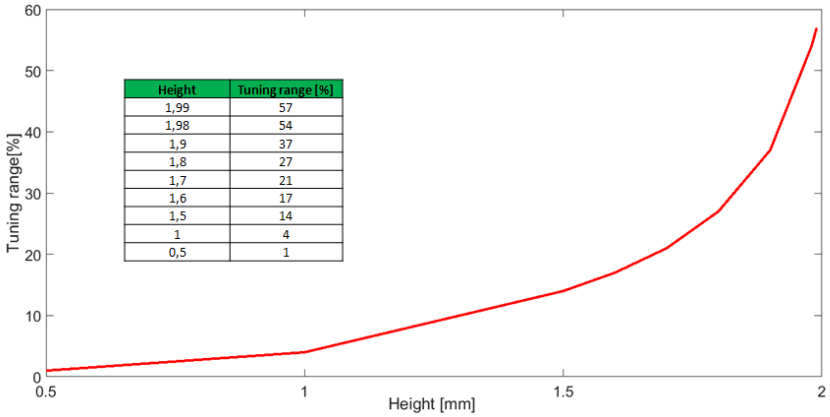

Height	Tuning range [%]
1,99	57
1,98	54
1,9	37
1,8	27
1,7	21
1,6	17
1,5	14
1	4
0,5	1

Figure 11: Tuning range (from 0pF to 10pF) versus the height of the post

The chosen height is a tradeoff between the tuning range higher than 25% and the feasibility to make the structure because if the post is taller than 1.8mm it might weaken the whole resonator. However, such simulations are not realistic because of the ideal behavior of the lumped element. To be closer to the reality, resistances are added to the simulation depicting the losses from the glue (epoxy for instance) used to stick those elements to the resonator. The value of this resistance is 0.1 Ω in order to take into account the resistivity of the SMT element and the resistivity provided by the non-perfect gluing process with epoxy. From the Figure 12 the tuning range varies from 2.4 GHz to 1.86 GHz with 0.7 dB and 5.1 dB of insertion loss respectively with capacitance values (red square) from 0pF to 7pF (to match with the measurements as seen later in this chapter) with a resistance of 1Ω (green square). The value of Q_0 changes from 326 to 106 with 20 S/µm conductivity for the resonator plating and the same Alumina used in the last part (ε_r = 8.7 and loss tangent of 1.10^{-4}).

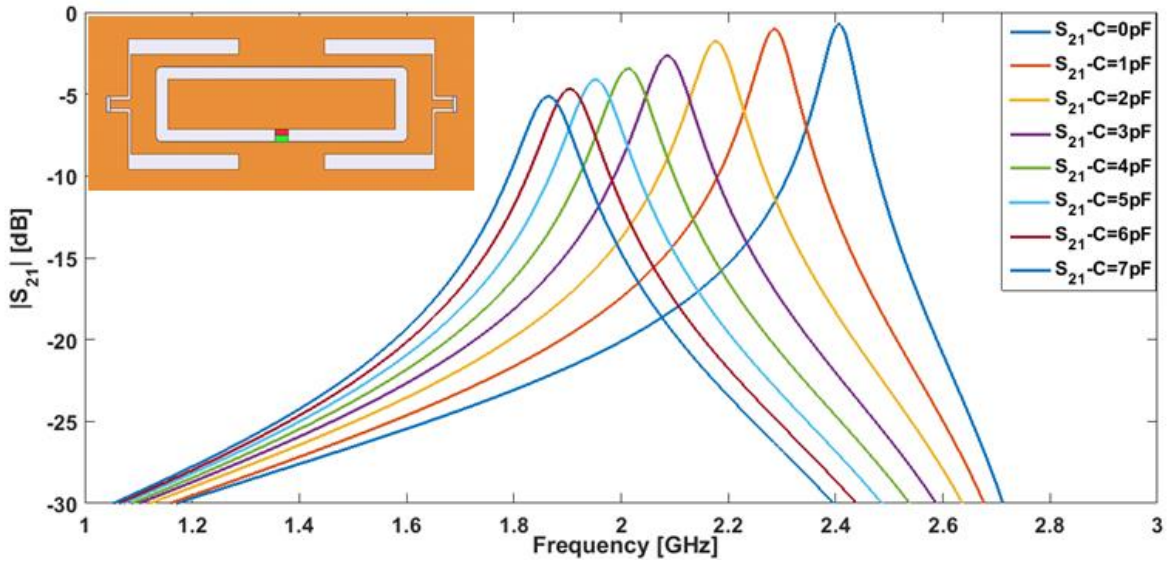

Figure 12: Tunability with a resistive element

3.2.3.2 Fabrication

In this chapter, the resonators and filters are made with the same method. Firstly, the Alumina based structures are created with an additive manufacturing process called Stereolithography [12]. Then, they are metallized either with gold or silver plating to confine the electromagnetic field within. In order to measure their frequency response, excitation coplanar lines are etched on the top**.**

3.2.3.2.1 Process

The Stereolithography process is chosen here to create 3D Alumina structures due to its rapid prototyping performances, good resolution (80µm) and the inexpensive cost of the produced CAD models. However, this method is not as cheap as the PCB process widely used to create SIW structure for instance. But thanks to the Alumina Stereolithography apparatus, the 3D structure has a very good loss tangent (1.10^{-4}) and can offer higher Q resonator.

The principle of the 3D Stereolithography (Figure 14) is based on a layer by layer polymerization of a photosensitive liquid monomer irradiated with a UV laser beam controlled by a computer. The first step is to design the object and to export the file into a particular format which transforms all the faces of the structure into elementary triangles. Thus, the said 3D object is cut into different slices which are 10-100µm thick. Those slices are created consecutively and can manufacture the whole 3D object layer by layer. With this method, complex structures can be made as depicted in Figure 13.

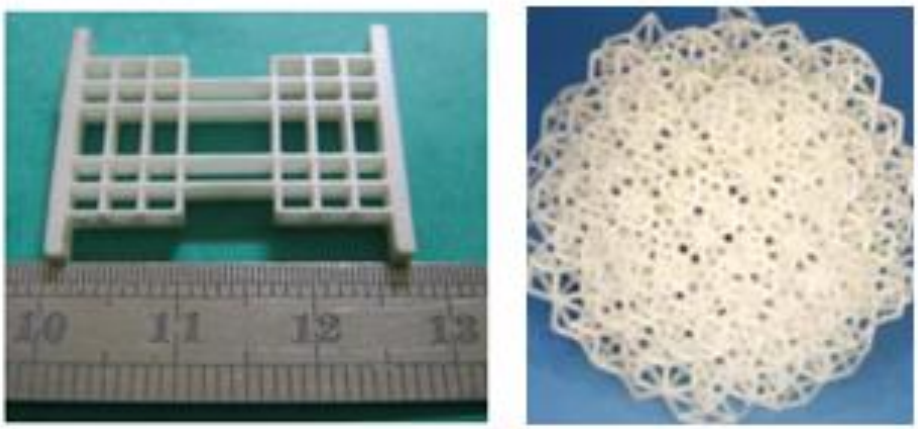

Figure 13: Structures made with stereolithography [3], [13]

The polymerization is made with a UV laser and specific mirrors to guide the beam on the specific layer (Figure 14). A particular spreading mechanism is set in the apparatus because of the high viscosity of the ceramic paste. The quantity for creating a layer is controlled thanks to a distribution system. The paste is spread uniformly on a 25cm×25cm surface with a double edge blade scraper and this layer is polymerized with the UV laser. Afterward, the carrier goes down (depth equal to the thickness of the next layer). At the end of the manufacturing, it is necessary to remove the non-polymerized paste with a brush and to

soak the 3D structure into different diluents baths. The created element is called “raw” because it has to be heat up to get its final dimensions, features and properties.

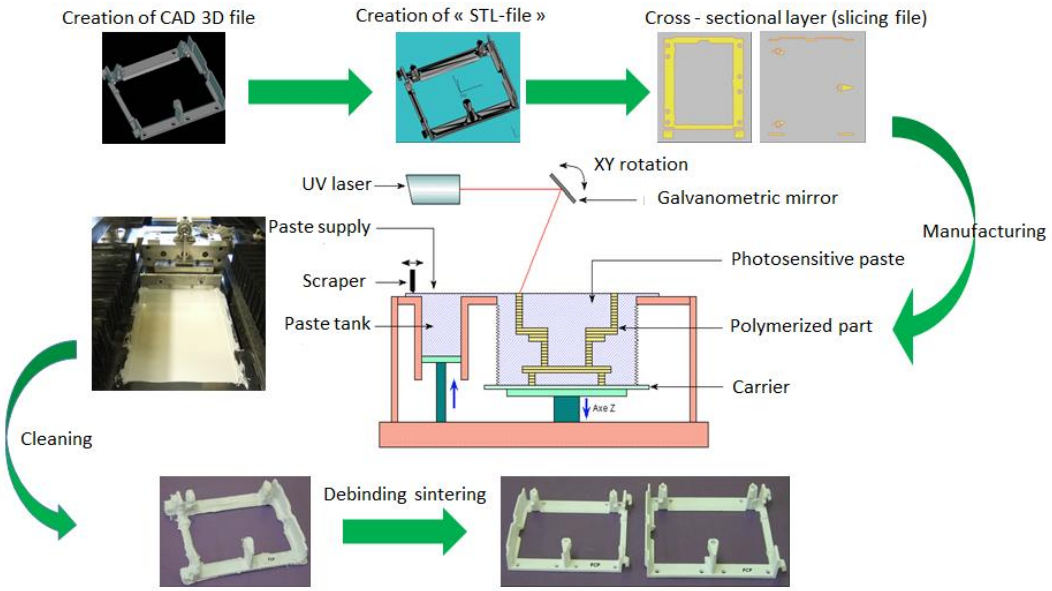

Figure 14: Stereolithography process

3.2.3.3 Measurements

3.2.3.3.1 Resonator

The resonators were made by the CTTC in Limoges with this additive manufacturing process. The X, Y and Z dimensions were measured thanks to a digital microscope made by Keyence. The comparison between the measurements and the simulation are illustrated in Figure 15. The eigenmode value shows a very small shift of the resonance frequency between the simulation and the measurement (<1%) showing that the SLA process created structure with dimensions close to the simulation. The next step is to metallize those structures to measure them and to compare the extracted value of the unloaded quality factor obtained by the measurement and the simulation (driven modal or eigenvalue). Copper with σ=10 S/µm (with gold electrolyse) and silver plating with σ=40 S/µm are chosen to cover the resonators.

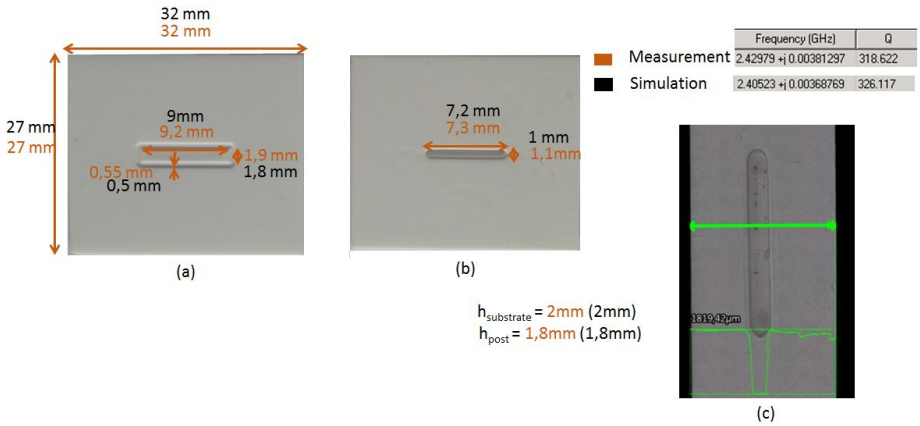

Figure 15: X, Y and Z dimensions of the loaded resonator- (a) top view, (b) bottom view, (c) height of the post measurement.

Nine filters were created, four which were metallized with silver by serigraphy process and the remaining five prototypes were metallized with copper layer created through an electroless process. The resonators are illustrated in Figure 16.

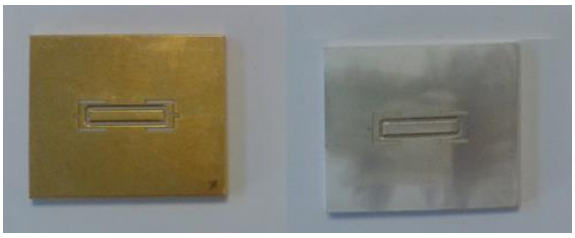

Figure 16: Copper and silver plated resonators

Silver resonators exhibit a good unloaded quality factor as seen in Table 2 (>600 for the best ones) and close to the simulation results. However, some resonators suffer from undercoupling due to the GSG probes used to measure the structures which do not contact well onto the surface. This problem occurred many times especially with a copper overlayer (Table 3) as seen in the measurement. So the extracted values of Q_0 are far from the theoretical value without a proper excitation of the structure (even if the resonance frequency is close to the expected value). A gold electrolysis was done to increase the thickness of the gold layer but even by doing that and with a consequence of a better contact of the probes, the results are still the same. So the quality of the copper is questioned and might be not suitable for such application.

Name	f_0(measured) [GHz]	f_0(simu) [GHz]	Δf ($f_{0measurde}$-f_{0simu})[MHz]	Δf_{-3dB} [MHz]	Ql	Q_0	Comments
Resonator 1	2.38	2.4	20				Undercoupling
Resonator 2	2.38	2.4	20	59	41	600	
Resonator 3	2.35	2.4	50	63	38	612	
Resonator 4	2.39	2.4	10	63	38	517	

Table 2: Quality factor associated with silver resonators

Name	f_0(measured) [GHz]	f_0(simu) [GHz]	Δf ($f_{0measured}$-f_{0simu}) [MHz]	Δf_{-3dB} [MHz]	Ql	Q_0	Comments
Resonator 6	2.34	2.4	60	70	33	33	
Resonator 7	2.32	2.4	80	72	32	32	
Resonator 8							Undercoupling
Resonator 9							Undercoupling
Resonator 10							Undercoupling

Table 3: Quality factor associated with copper plated resonators

The comparison of the resonance frequency is made between the measurement and the driven modal solution type with HFSS software. One example is depicted in Figure 17.

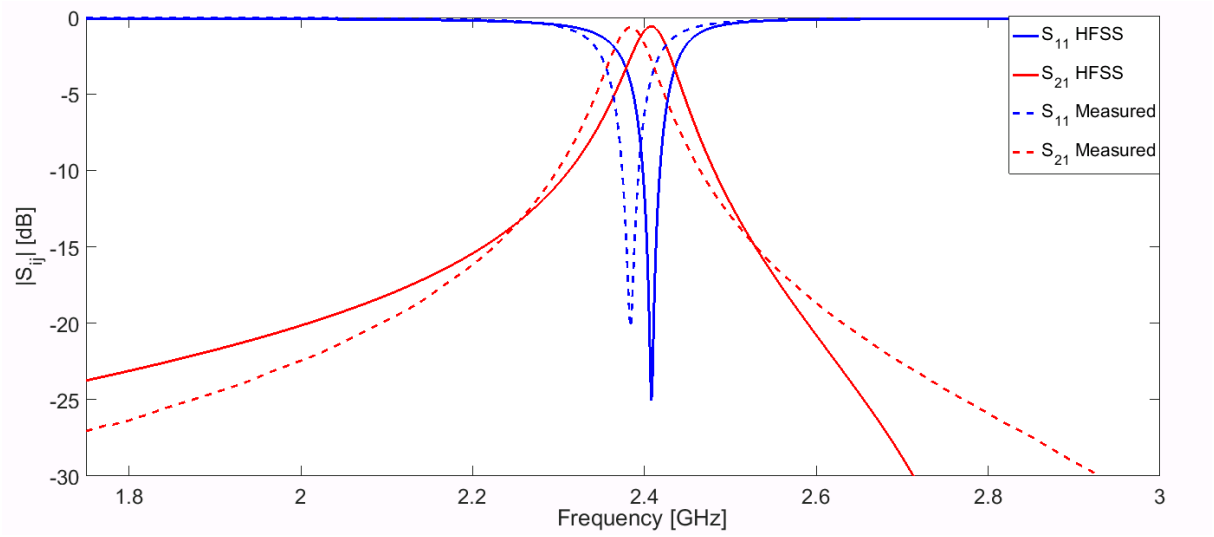

Figure 17: Comparison between simulation (HFSS) and measurement corresponding to the Resonator 2.

3.2.3.3.2 Tunability

As said previously, the tuning effect is provided by the implementation of Surface Mounted Capacitor on the rectangular etched gap. Different values from 1pF to 7pF have been studied and reported on the Table 4.

Value [pF]	f_0 (measured) [GHz]	f_0(simu) [GHz]	Δf ($f_{0measured}$-f_{0simu}) [MHz]	IL (measured) [dB]	Q_0 (measured)	Q_0 (simu)
0	2.38	2.40	20	0.63	600	580
1	2.25	2.28	30	0.66	525	511
2	2.08	2.16	80	1.12	326	302
3	1.97	2.06	90	1.30	282	252
4	1.88	1.99	110	1.71	248	225
5	1.79	1.93	140	1.88	228	209
6	1.70	1.88	180	2.43	195	170
7	1.68	1.84	160	2.66	190	142

Table 4: Extracted values of the measured resonators

The resonance frequency from the measurements is always close to the simulation (160 MHz shift for the worst case). The unloaded quality factor decreases from 600 to 190 depending on the value the capacitor. The tuning range is 29% of f0 which is higher than the simulation (about 23%). Those results are very convincing because this high Q resonator has a high tuning range according to the Table 1 from the Chapter 2. On top of that, the Q_0 is much higher than SIW structures introduced in the last chapter for instance as it is twice as high for the best case. However reaching such a Q_0 means using substrate of good quality and therefore increases the price of the whole structure.

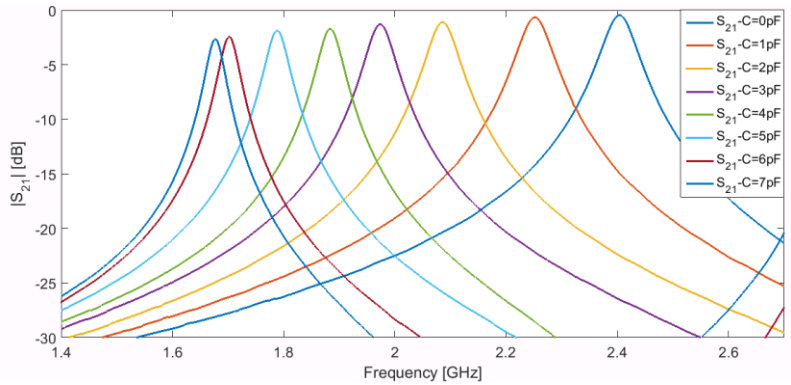

Table 5: Tunability measurement of the resonator

3.3 Miniaturization

3.3.1 Concept

The next goal is to create a more compact resonator with a size reduction higher than 25% to minimize the size of the unit cell (Figure 1), with high unloaded quality factor (>400), and a tuning range greater than 15%. The previous structure has interesting features but it is possible to miniaturize by increasing the capacitive effect provided by the post. A simple simulation consisting of increasing or decreasing the height of the capacitive post in the middle of the cavity allows the impact of the post to be quantified. Four values for the height of the post are chosen and the resonance frequency is noted for each.

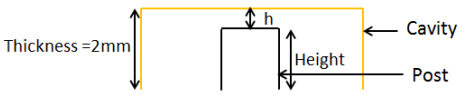

Height [mm]	f_0 [GHz]
1.8	2.41
1.95	2.40
1.9	2.39
1.95	2.39

Table 6: Resonance frequency for different heights of the capacitive post

As seen in Table 6 the influence of the post is not significant enough which is unexpected because such a post has to be of important influence on f_0. To understand this behaviour the latter is considered as a parallel plate capacitor with a ε_r=8.7 and an area, A, of 7.2 mm^2. Knowing the total height of the substrate is 2mm, a variation of capacitance is computed as a function of a variation of the post's height.

The formula for a parallel plate capacitor is:

$$C = \frac{\varepsilon_0 \varepsilon_r A}{h} \tag{9}$$

h is the distance between the two plate.

The variation of the capacitance due to the change of height is given by:

$$\Delta C = \frac{|h_1 - h_2| \times \varepsilon_0 \varepsilon_r A}{h_1 \times h_2} \quad (10)$$

With $\Delta C = C_2 - C_1$

So two values of height are chosen, namely 1.8mm and 1.95mm, which represent a h_1 of 0.2mm and h_2 of a 0.05mm respectively. The computed ΔC is 8.3pF which should provide a wide shift on f_0. Since the post has no such influence on the resonance frequency, let us first consider the structure as a series RLC resonator. The equivalent capacitance is 4.4pF found by (5) with an inductance of 1nH. The last value is added with the variation of capacitance which gives 12.7pF. The new of f_0 should be 1.41GHz for a total capacitance of 12.7pF and it is much lower than the value found with HFSS software. This difference might come from the isolated metal patch surrounded by the rectangular etched gap. Indeed, this isolation creates a floating ground (Figure 18) which prevents the EM field from setting up between the metal layer and the top of the post. In order to solve this problem a new design has been investigated.

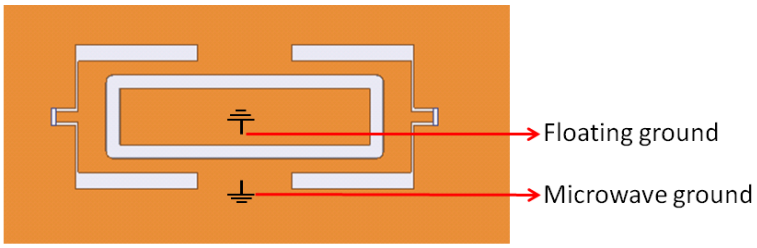

Figure 18: Representation of the grounds for the resonator

This new structure consists in implementing two non-connected patterns etched in U shape with a top metallization above them (Figure 19). The resonance frequency is 1.43GHz with insertion loss of 0.46dB, a bandwidth of 71 MHz. The new f_0 is very close to the one computed in the last section (1.41GHz) which is confirmed that the main capacitive effect is from the capacitive post and can be modeling as a parallel plate capacitor.

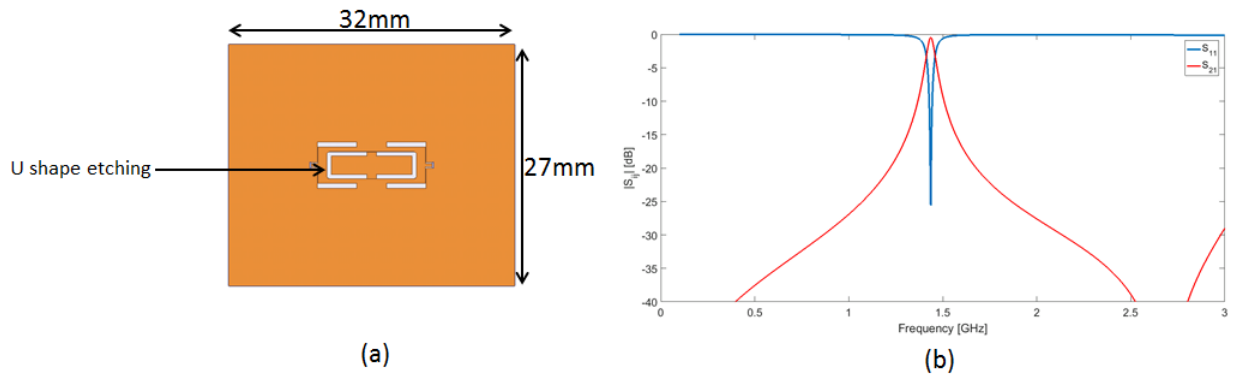

Figure 19: New design of the resonator (a) and its associated S parameters (b)

The next step using this new design (Figure 19) is to readjust the size of the whole resonator to obtain a resonance frequency close to 2.4 GHz (with h=0.8mm). The Figure 20 illustrates the compact resonator with a f_0 of 2.49 GHz and with an unloaded quality factor of 590 (Eigen mode simulation with silver plating)This unloaded quality factor is still high (>500) for this compact resonator. The influence of the post (with a height of 1.8mm) allows a significant reduction of the size of the substrate (34% of surface saving as it can be seen in Figure 20).

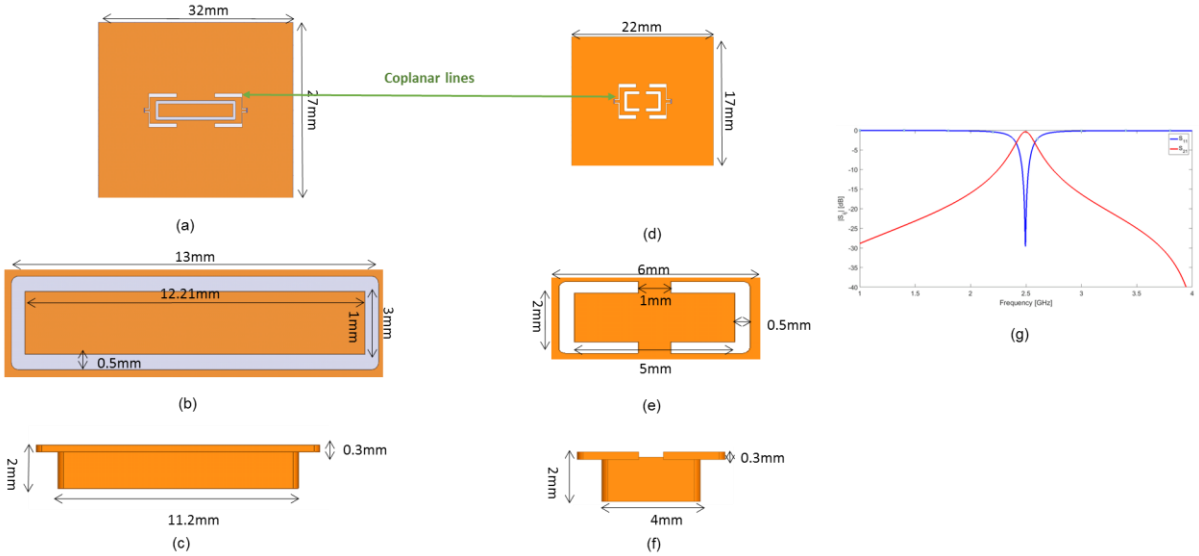

Figure 20: (a), (b) top views of the first filter, (c) its side view, (d), (e) top views of the compact filter, (f) its side view, (g) S parameters of the compact resonator.

3.4 Measurements

The process used to manufacture this miniaturized resonator is the same as before. Silver plating was applied on all the compact resonators to achieve Q_0. The Figure 21 illustrates the new design with the old one (same scale). Four compact structures were manufactured and studied, the experimental vales are found in Table 7.

Figure 21: Picture of a compact resonator (32mmx27mm) and the previous design (22x16.8mm)

Thanks to a numerical microscope from the brand Keyence dimensions of the manufactured structure are measured. A comparison between the physical structure and the simulation from HFSS is made in Figure 22. The alumina substrate is 22mm×17mm on HFSS and 22mm×16.8mm for the created resonator and the rest of the dimensions are very close to the simulation.

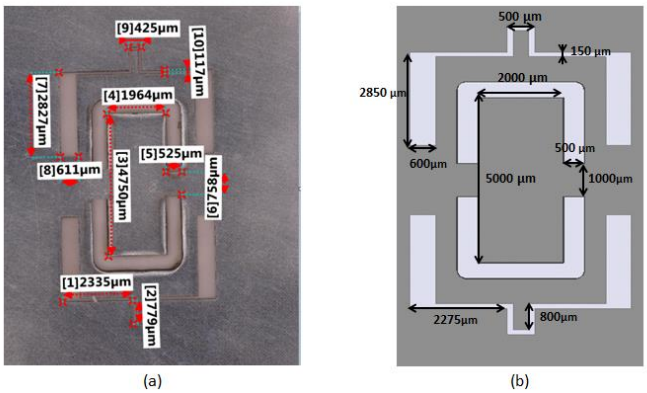

Figure 22: Measurement of the dimensions for the manufactured resonator (a) and simulation (b)

The frequency response of such a structure is obtained by using the same 500µm pitch GSG probes than previously. The results for the compact resonator number 1 are depicted are compared with the simulation in Figure 23.

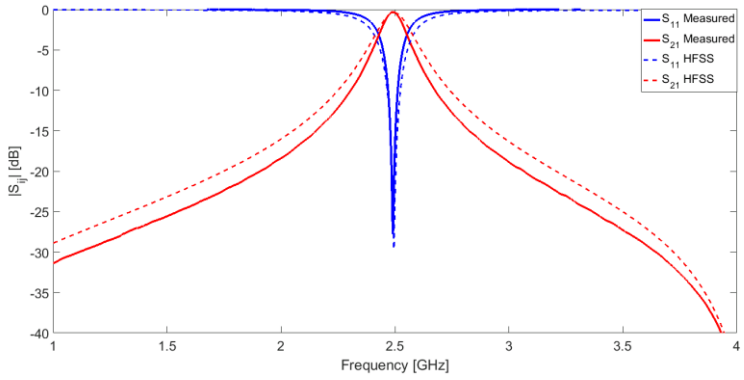

Figure 23: Simulation and Measurement comparison of the miniaturized resonator "Compact1"

Name	Height of the post [mm]	f_0 (measured) [GHz]	f_0 (simu) [GHz]	Δf ($f_{0measured}$-f_{0simu}) [MHz]	Δf_{-3dB} [MHz]	Ql	Q_0
Compact 1	1.8	2.50	2.49	50	128	19	570
Compact 2	1.78	2.55	2.49	10	134	19	518
Compact 3	1.85	2.35	2.49	190	112	21	425
Compact 4	1.82	2.46	2.49	80	127	19	390

Table 7: Measurements for the miniaturized resonators

Even if the resonance frequency is very close to simulation results ("compact 1", "Compact 2" and "Compact 4") the difference is greater for "Compact 3". In fact if the height of the post is just a bit higher or smaller than the simulation the shift of f_0 is more significant since the E-field between the metal layer and the top of the post is now more important than before. This is why the most important f_0 shift is observed for "Compact 3" which has the highest difference of height between simulation and measurement as seen in Table 7. The unloaded quality factor is more than 500 for the structures "Compact 1" and "Compact 2" for a surface reduction of 34% and only a reduction of 5% of the Q_0.

3.5 Tunability

The main problem with this structure is that it cannot be tuned properly. Indeed if a lumped element is set on the gap to produce an extra capacitive effect and thus creating a shift of $f_{0,}$ nothing happens. In the previous case the metal patch was isolated from the microwave ground but for this miniaturized structure the top metal layer is connected to the ground and therefore tuning is not created if a lumped element like SMT capacitance is set. The idea to solve this problem is to remove a dielectric and a metal part in order to create a U shaped capacitance illustrated in Figure 24. To manufacture this structure a micro machining tool was used to drill the alumina part

Figure 24: Novel miniaturized resonator

The four compact resonators were measured again with GSG probes. An example of comparison between the simulation and the measurements is found in Figure 25. The Table 8 sums up all the insertion loss and Q_0 for these novel resonators.

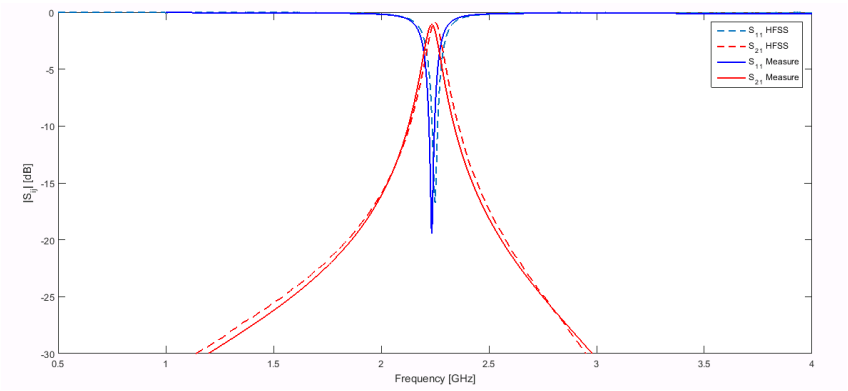

Figure 25: Comparison between simulation and measurement for the novel miniaturized resonator

Name	f_0(measured) [GHz]	f_0 (simu) [GHz]	Δf ($f_{0measured}$-f_{0simu})[MHz]	Δf-3dB [MHz] (measure	IL(measured) [dB]	Ql (measured)	Q_0(measured)
New compact1	2.25	2.23	19	84	0.9	27	275
New compact 2	2.18	2.23	51	81	1.0	27	255
New compact 3	2.22	2.23	11	80	0.8	28	303
New compact 4	2.07	2.23	161	75	1.0	28	261

Table 8: Extracted values for the four novel miniaturized resonator

Once again the f_0 from the measurements are close to simulation. However, the Q_0 is now lower than 300 due to the U shaped capacitance which is a lossy element. This observation is made with HFSS before the measurement because the simulated Q_0 is about 320.

In order to study the tunability, the same process is applied with different values of SMT capacitances. Each measurement is referenced in Table 9. As seen, the insertion loss increases significantly for capacitive values higher than 1.5pF. Therefore the tuning range may be considered useful for the capacitive values from 0pF and 1.5pF which is about 15%. The Q_0 decreases from 303 to 101 when adding a capacitance of 4pF. As expected, several tradeoffs exist between the Q_0, the tuning range and the size of the structure. It should be noted that throughout this chapter different capacitance ranges were studied for each resonator in order to study the maximum tuning range for each case. In the next part, a comparison between those three structures (original resonator, novel miniaturized structure and the CRLH SIW resonator from the Chapter 2) and others from the literature is made to underline pros and cons for each structure.

Values [pF]	f_0(measured) [GHz]	f_0(simu) [GHz]	Δf ($f_{0measured}$-f_{0simu})[MHz]	IL(measured) [dB]	Q_0(measured)	Q_0(simu)
0	2.20	2.23	30	0.91	303	320
1	2.05	1.95	100	1.59	215	232
1.5	1.88	1.85	30	2.29	192	202
2	1.87	1.83	40	4.7	171	186
2.2	1.84	1.79	90	5.17	156	175
2.7	1.79	1.74	50	6.58	120	150
3	1.70	1.69	10	6.88	114	135
4	1.68	1.54	140	13.62	101	115

Table 9: Extracted values of measured novel miniaturized resonators

3.6 Comparison

For this part several publications from the literature are compared with the three resonators developed in this thesis: the SIW based first generation cell, the Alumina based high Q tunable cavity resonator and the miniaturized type. Three SIW structures are chosen : [2], [14], [15] as well as four 3D approach resonators [16]–[20] in order to have a global perspective and to point out pros and cons for each of our structures by comparing them to resonators based on different technologies : 2D approach (SIW structures) and 3D approach (3D structures). The studied features in Table 11 are the unloaded quality factor (Q_0) for the off state when Q_0 is the greatest (Q_{max}) and for the on state when the Q_0 is the lowest (Q_{min}). Q_{max} and Q_{min} are related to f_{high} and f_{low} respectively because in the off state no added capacitance effect is applied unlike for Q_{min} when the added capacitance is the most important and f_0 is as low as possible. In order to compare the size of each structure by taking into account the permittivity of the substrate the guided wavelength is computed for each resonator (11). The a, b and c dimensions relates with those in Figure 2.

$$\lambda_g = \frac{c}{f_0\sqrt{\varepsilon_r}} \tag{11}$$

	Name	Q_0 (Q_{max}-Q_{min})	f_{high} [GHz]	f_{low} [GHz]	TR (f_{high}-f_{low}/f_{high}) [%]	λ_g [mm]	a [λ_g]	b[λ_g]	c[λ_g]	Volume 10^3 [λ_g^3]
Structures from the thesis	1st generation	110-53	2.68	0.97	64	75	0.14	0.02	0.3	0. 8
	2nd generation	600-190	2.38	1.68	29	42	0.64	0.05	0.76	24
	Compact 2nd generation	303-101	2.2	1.88	15	46	0.36	0.04	0.48	6.9
SIW structures	[14]	299-286	10	9.82	1.8	16	0.9	0.21	0.9	170
	[2]	214-90	1.1	0.5	54	149	0.24	0.03	0.24	1.73
	[15]	640-300	3.4	1	70	45	0.2	0.07	0.5	25.2
3D structures	[16]	650-300	5	1.9	62	31	0.58	0.14	0.97	78.76
	[17]	1000-300	24.4	6.1	75	3.5	2	0.71	1.71	2698
	[18]	240-110	4	2.5	37.5	21	0.19	0.25	0.85	40.4
	[19]	702-360	4.6	2.3	50	23	0.43	0.08	0.43	14.8
	[20]	1150-350	6	4	33	25	0.36	0.3	0.46	49.7

Table 10: Comparison between resonators created in the thesis and others from the literature

The first generation, the SIW resonator with the interdigital capacitance, has one of the most extended tuning range with loaded cavities such as [15] and [17]. But the compactness of this metamaterial resonator is very important and the tradeoff between the size and the tuning range of such a structure is the best among those publications, as seen in Figure 26 where a comparison is done between the tuning range and the volume in terms of $\lambda_g^3(a[\lambda_g]\times b[\lambda_g]\times c[\lambda_g])$. For a better reading, the volume is plotted using a log scale. The minus sign allows the dimension to be normalized: if one is negative (for instance in [17]) that means one or more of its dimensions are higher than its λ_g and the compactness of the structure is then questionable. Even though this first generation has the best compactness related to its tuning range, but its Q_0 is the smallest compared with the other resonators.

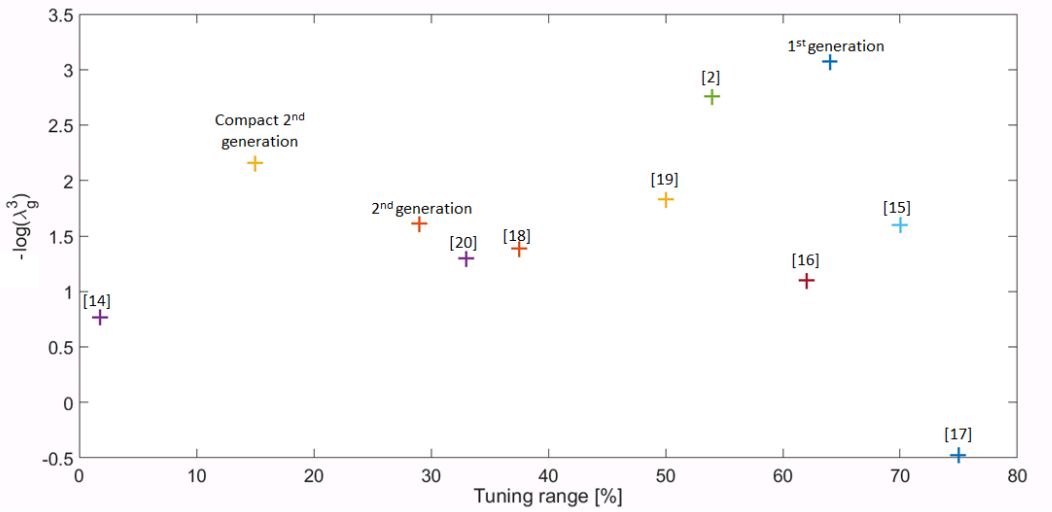

Figure 26: Comparison between the compactness and tuning range

The second generation has the highest Q_0 among the three resonators developed throughout the thesis and higher than [2], [14] and [18] but with narrower tuning range as seen in Figure 27 . On top of that, some resonators from the literature have a better Q_0 with high tuning range in most 3D structures cases. But this resonator is simple compared to 3D approach structures that are divided into several elements to create a single resonator. The Alumina substrate with a ε_r of 8.7 allows the resonator to have a quite good compactness associated with a high Q as seen in Figure 28.

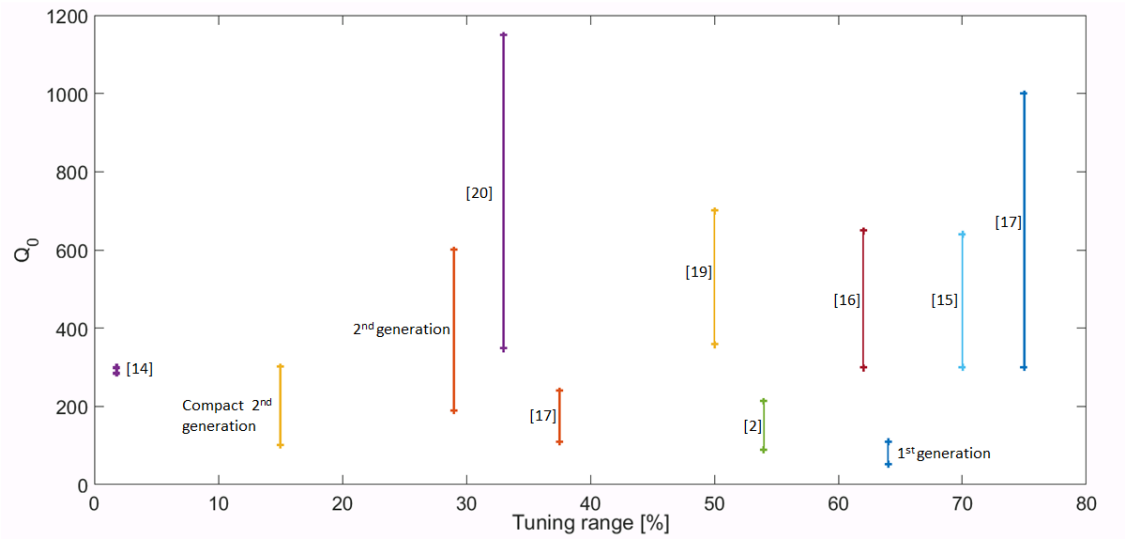

Figure 27: Unloaded quality factor versus the tuning range

The compact second generation cell has a very good compactness as seen in Figure 26 and Figure 28. On top of that the related Q_0 is quite high and among the more compact resonators namely the first generation cell and [2]; this compact resonator has the best unloaded quality factor and it is possible to reduce the size of the whole structure by increasing the height of the capacitive post. Unfortunately the tuning range is low as seen in Figure 27.

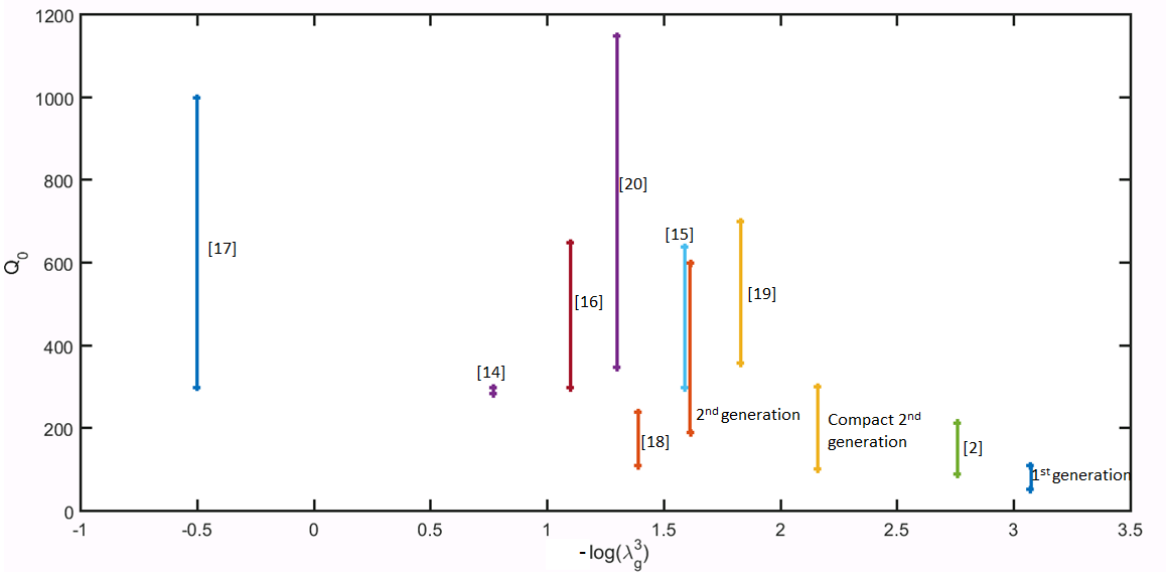

Figure 28: Unloaded quality factor versus the compactness

3.7 Multi-pole filters

This section investigates multi-pole filters based on the compact resonator presented in the previous section in order to evaluate their performance. Firstly, a second order filter is studied with explanations about optimization of such a filter and how this structure can be tuned. Then, a three pole and four poles are simulated and a discussion is proposed about the topology of the last one to create a transmission zero to improve its selectivity.

3.7.1 Second order filter

3.7.1.1 Concept

The basis of this filter is the same as the design depicted in Figure 21, but another metal post is added to create the second pole. Thus, a magnetic coupling is created between these two posts since a magnetic field arises around each of them as seen in Figure 29

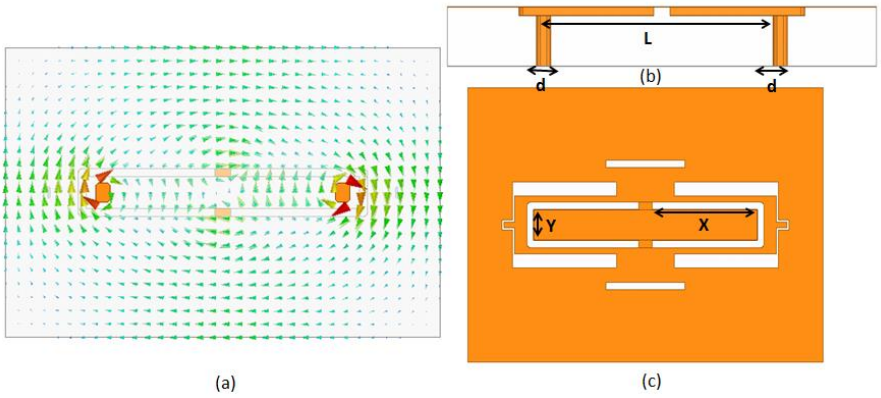

Figure 29: Magnetic field around the metallic posts -orange boxes- (a), side view (b), top view (c)

In order to create a proper second order filter with a central frequency around 2.52GHz with a bandwidth of 22% (the features are chosen arbitrarily), critical parameters need to be optimized namely the dimensions of the resonators, the distance between them and the size of the rectangular shaped gap. Parametric studies can be done to optimise the design because they are simple enough for a second order filter but time demanding for a higher number of pole. Thus, another approach with coupling matrices is used for finding optimal dimensions to match the pattern of the Tchebychev two poles filter depicted in Figure 30.

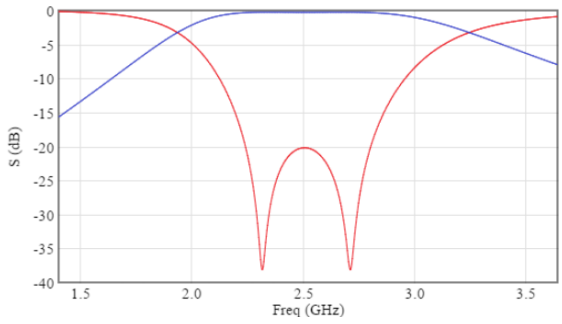

Figure 30: Objective frequency response

The coupling matrix is particularly useful because of its matrix form which allows mathematical operation (for matrix) to be applied such as inversion, partitioning and so on. On top of that it clearly represents the coupling (direct or indirect) for each different resonator with the others for mutlicoupled series-resonator illustrated in Figure 31. L_i and C_i define the resonators and $\overline{Mij}$ the coupling between them. It should be noted that the resonators are assumed lossless.

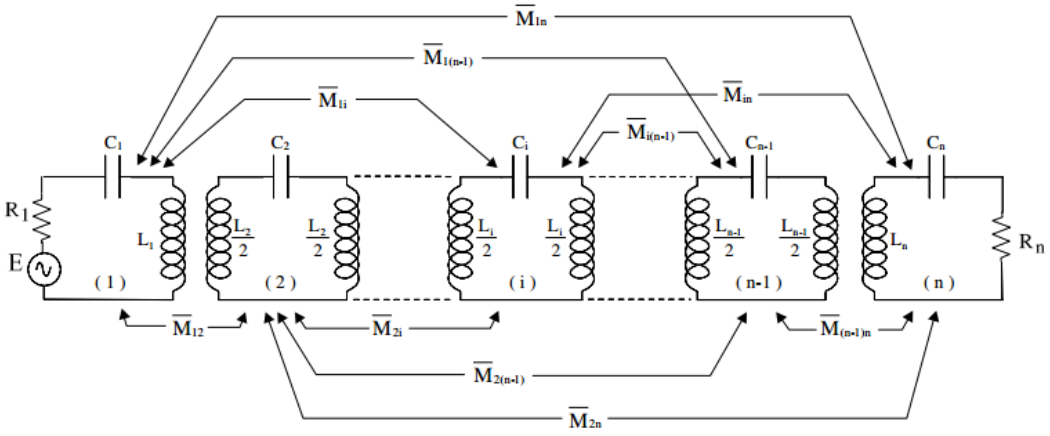

Figure 31: Multicoupled serie-resonator bandpass prototype network [21].

Mathematical processes are needed to implement the value of different couplings from the electrical model (Figure 31) into the matrix form and are detailed in [21]. Different types of coupling matrix exist depending on the topology of the filter. For instance the arrow coupling matrix which is useful because it can be the starting point for others transformations. Another form is the folded configuration because those topologies are realized with cavities

and allow a maximum transmission zeros. Those two widely used topology are depicted in Figure 32.

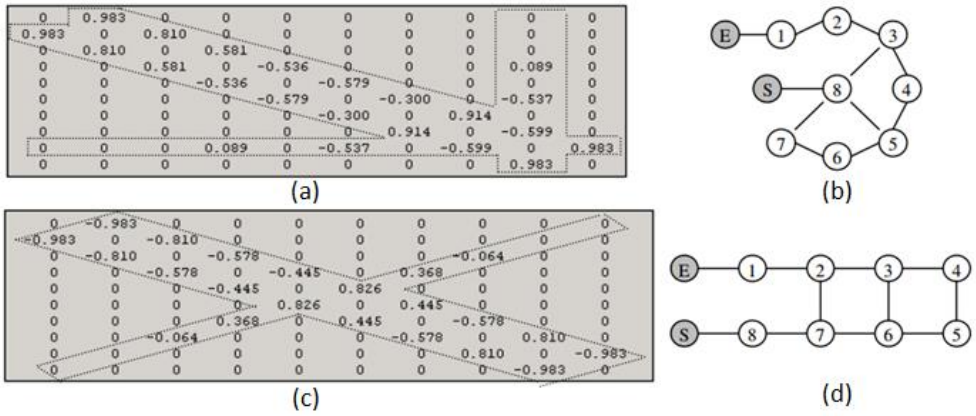

Figure 32: (a) Arrow coupling matrix ,(b) related topology, (c) folded coupling matrix ,(d) related topology [22].

Once the theoretical coupling matrix is obtained it is possible now to optimize the design. The software called PRESTO developed by Xlim and the INRIA is used to extract a coupling matrix from the S parameter of the simulated second order filter (HFSS design) and to compare it with the theoretical coupling matrix. Thanks to this process the identification of what coupling should change to be closer to the ideal results is possible and thus the physical parameters of the filter can be adjusted.

By using this method the design of a two pole Tchebychev filter illustrated in Figure 29 is optimized. The ideal coupling matrix with a bandwidth (BW) of 0.56GHz and a central frequency (f_c) of 2.52 GHz is the following:

$$\begin{bmatrix} 0 & 1.23 & 0 & 0 \\ 1.23 & 0 & 1.67 & 0 \\ 0 & 1.67 & 0 & 1.23 \\ 0 & 0 & 1.23 & 0 \end{bmatrix} \quad (12)$$

To match as close as possible (12), the parameters of the two poles filters in HFSS are optimized to obtain the final design illustrated in Figure 33:

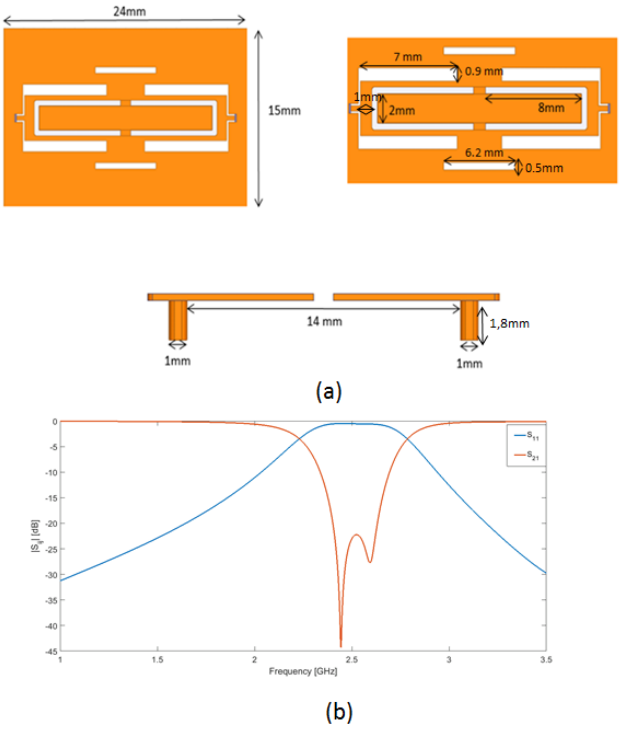

Figure 33: (a) Dimensions of the second order filter, (b) related S parameters (HFSS)

The simulated filter has a f_c of 2.52 GHz and a FBW of 22%. The return loss is -22dB and the insertion loss (I.L.) is 0.52dB. The simulated coupling matrix associated with this structure is:

$$\begin{bmatrix} 0 & 0.95 & 0 & 0 \\ 0.95 & 0.060 & 1.5 & 0 \\ 0 & 1.5 & 0.060 & 0.95 \\ 0 & 0 & 0.95 & 0 \end{bmatrix} \quad (13)$$

Several notes can be pointed out from (13). Firstly, the good frequency position of each pole since 0.06 (for the first pole) and 0.06 (for the second pole) are close to zero. Then the inter-resonator coupling almost matches with the ideal one (1.67). But, the input and output coupling are lower than expected. To increase that value the excitation lines might be increased for instance from 7mm to 7.5mm but in that case it can only reduce the BW and shift the f_0. On top of that increasing the Q_e (access coupling) does not reduce the insertion loss so that is why the length of 7mm is kept for those lines.

Four two poles filters were created with the same process than with the previous resonators. Each of them was measured with a 500µm pitch GSG probes. The values from the measurements are reported in Table 11.

Name	f_c(measured) [GHz]	f_c(simu)[GHz]	Δf ($f_c$measured-$f_c$simu) [MHz]	Δf-3dB (simu) [MHz]	Δf-3dB (measured) [MHz]	Return loss (simu) [dB]	Return loss (measured) [dB]	IL (measured) [dB]
2_pole_1	2.76	2.52	240	560	900	-22	-8.1	-1.6
2_pole_2	2.96	2.52	440	560	960	-22	-6.27	-1.7
2_pole_3	2.74	2.52	220	560	860	-22	-5.6	-2.4
2_pole_4	2.7	2.52	180	560	800	-22	-8.1	-1.4

Table 11: Extracted measurement for the four two-pole filters

A shift of the f_c is observed and the measured BW is higher than expected. On top of that the return losses for all the filters are greater than 10dB. For explaining those differences between the simulation and the measurement the dimensions of the fourth two-pole is done.

A dimensional study is made thanks to a Keyence digital microscope as seen in Figure 34 .

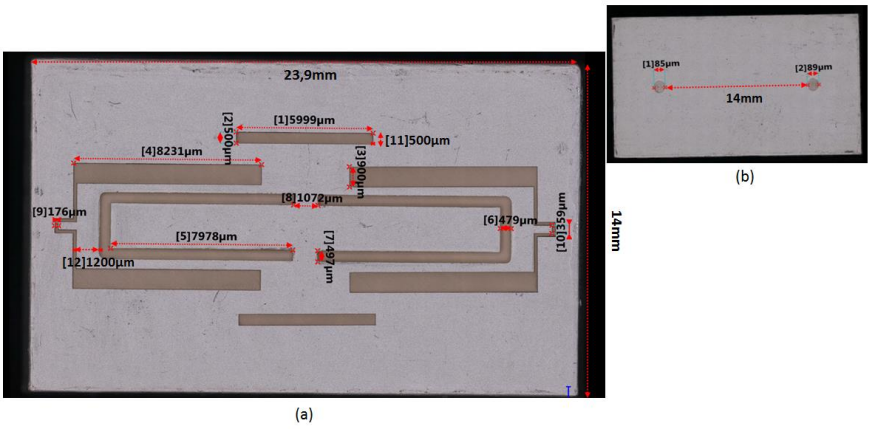

Figure 34: Dimensions of the fourth second order filter(24mm×14mm), (a) front side, (b) back side.

Almost all the dimensions match with the simulation ones except for the length of the excitation lines (8.2mm instead of 7mm) and the space between them and the gap (1.2mm

instead of 1mm). Even though the length of the excitation lines is greater (about 1mm), the access coupling is lower than expected because the space between those lines and the rectangular gap of the structure is 0.2mm longer and this dimension is very influential on the Q_e and that can explain the undercoupling of the second order filter. Moreover, the height of the posts is not exactly 1.8mm but 1.78mm for the first one and 1.7mm for the second one. Then the capacitive effect changes; this difference explains why the poles do not have the same frequency compared to the simulation and why the coupling between the resonators ($\overline{M21}$) changes as well. The bandwidth of the filter is altered by these two features namely Q_e and $\overline{M21}$. To emphasize this explanation, the coupling matrix (14) is analyzed and the same conclusions are pointed out. Indeed, the output and input coupling are 0.82 and not 0.95; the coupling $\overline{M21}$ is 1.1 instead of 1.5 which alters the bandwidth. The frequency of the second pole is more shifted since the height of the second post has the greatest change about its dimensions.

$$\begin{bmatrix} 0 & 0.82 & 0 & 0 \\ 0.82 & -0.040 & 1.1 & 0 \\ 0 & 1.1 & 0.16 & 0.83 \\ 0 & 0 & 0.83 & 0 \end{bmatrix} \quad (14)$$

The next goal is to improve the characteristics of such a structure. As it is an all in one structure it is difficult to modify several dimensions such as the distance between the post and their height. This is why two 6mmx0.5mm lines were etched on both sides of the filter to provide a post processing. Theoretically, they can change the f_c and the Q_e by reducing or increasing the length; in this case the first option is chosen to have a higher a Q_e. The idea is to put silver paint over each line to reduce them as much as possible. But it is not effective because the coupling access is not as high as in the simulation making post processing lines not useful enough. So the only solution to have significant change of the Q_e is to increase the length of the coplanar excitation lines.

The excitation lines of fourth second order filter was etched, as seen in Figure 35, in order to add an extra length of 1.5mm (according to the dimension from the Keyence device the extra length is 1.6mm so a total length of 9.8mm).

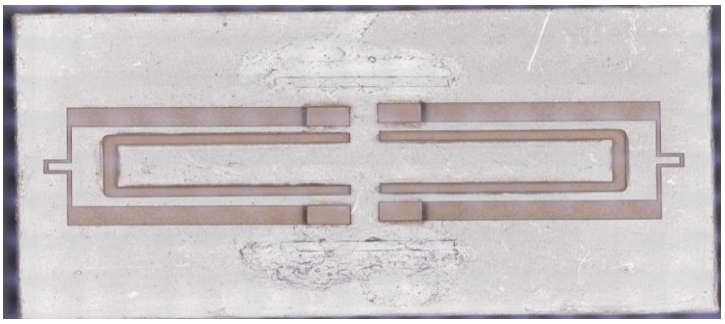

Figure 35: final second order filter

The measurement depicted in Figure 36 shows that the return loss is 15dB which gives the filter a flatter bandwidth but a wider BW than before (192 MHz), lower insertion loss (0.46dB). The f_c shifts to 2.82 GHz.

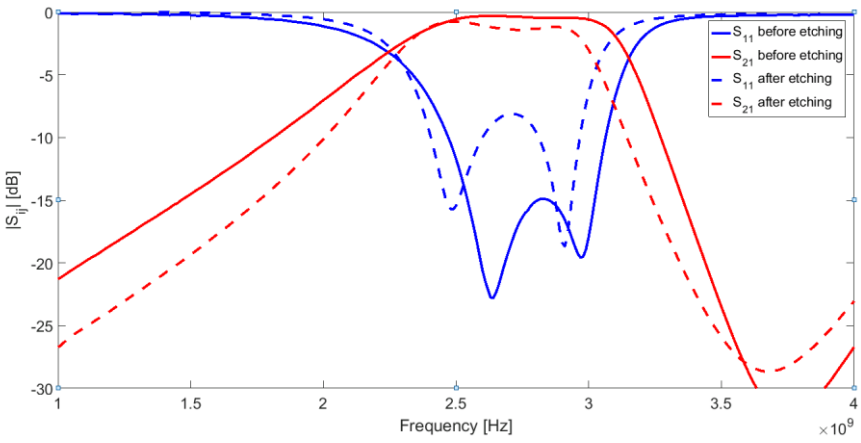

Figure 36: Comparison of S parameters before and after the etching

The input and output coupling have increased as shown in (15) as well as $\overline{M21}$.

$$\begin{matrix} 0 & 0.95 & 0 & 0 \\ 0.95 & -0.030 & 1.3 & 0 \\ 0 & 1.3 & 0.080 & 0.95 \\ 0 & 0 & 0.95 & 0 \end{matrix} \quad (15)$$

The return loss might be better if the length of the excitation lines increases but as the fact that retro-simulation of this structure is time consuming (for matching the Q_e) a tradeoff was made for this dimension. On top of that etching more than 1.5mm might be critical because if the excitation lines touch each other it will be impossible to excite the structure properly.

Even though the features of this filter could be closer to the simulation, its features are good with a return loss of -15 dB and insertion loss of 0.46dB. Unfortunately this second order filter is not tunable, for the exact same reason as the first compact filter: the top metal layer is grounded. So a new design is proposed in the next part to make a two pole tunable filter.

3.7.2 Tunability

Based on the design of the compact tunable filter, two elementary cells with their own capacitive post are placed side by side as illustrated in Figure 37 with the dimensions. The red rectangular represents the perfect capacitive effect to demonstrate the tuning aspect of the concept. The simulation on HFSS gives a second order filter with a return loss of -17 dB, IL of 0.7dB and a BW of 370 MHz.

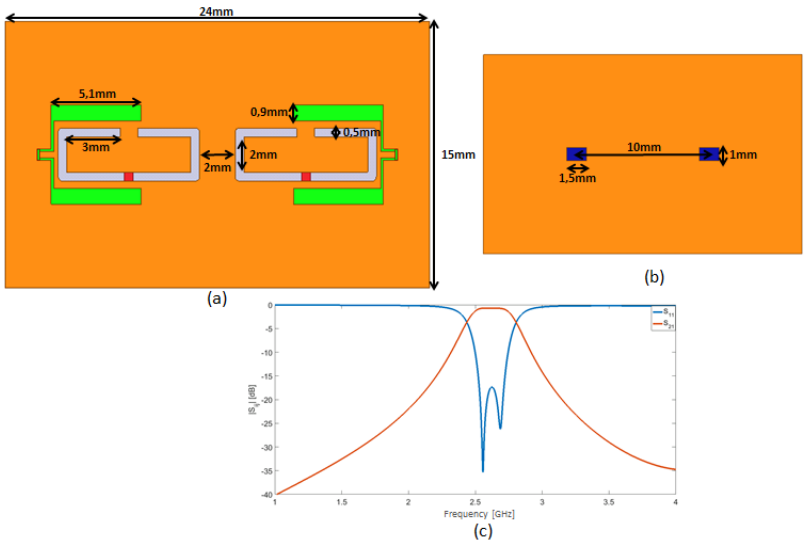

Figure 37: Dimensions of the tunable second order filter, (a) front side, (b) back side, (c) related S parameters

Thanks to the HFSS software, frequency response is given for a variation of the added capacitance from 0pF to 1 pF. As seen in Figure 38 this tunable structure has a tuning range of 15% (f_c varies from 2.62 GHz to 2.23 GHz) with an evolution of the return loss from -17 dB to -6.5dB. The insertion loss decreases as long as the capacitive effect increases i.e. from 0.7dB to 3dB as well as the BW from 370 MHz to 170 MHz.

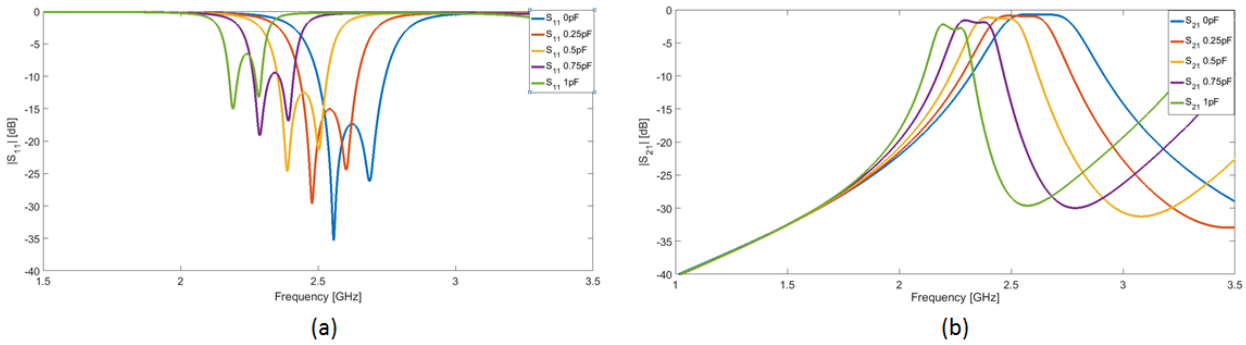

Figure 38: S parameters for the tunable second order filter, (a) S11, (b) S_{21}

As expected this design allows a tuning of the central frequency unlike the previous one. This filter can be more optimized with better return loss and insertion loss if a better control of the evolution of $\overline{M21}$ over the tuning range is done. This structure was demonstrated as a proof of concept to make a two pole tunable filter based on the miniaturized compact resonator. Unfortunately, this structure was not manufactured because of the lack of time.

3.8 Third and fourth order filter

Two designs based on the tunable filter are presented in this part. As previously only simulations have been done so far. The topologies for those filters are quite simple because an elementary cell is added right after the other.

The third order filter is designed to obtain a central frequency of 4GHz and a bandwidth of 1.3 GHz. The features of this structure are chosen arbitrarily as well as the fourth order filter. The same optimization method is applied namely the matching of the ideal coupling matrix (16) with the one from the HFSS software (17).

$$\begin{bmatrix} 0 & 1.08 & 0 & 0 & 0 \\ 1.08 & 0 & 1.03 & 0 & 0 \\ 0 & 1.03 & 0 & 1.03 & 0 \\ 0 & 0 & 1.03 & 0 & 1.08 \\ 0 & 0 & 0 & 1.08 & 0 \end{bmatrix} \quad (16)$$

$$\begin{bmatrix} 0 & 0.99 & 0 & 0 & 0 \\ 0.99 & 0.15 & 0.89 & 0 & 0 \\ 0 & 0.89 & 0 & 1.0 & 0 \\ 0 & 0.12 & 1.0 & 0.14 & 0.99 \\ 0 & 0 & 0 & 0.99 & 0 \end{bmatrix} \quad (17)$$

The matching of those coupling matrix is very good because the values from (17) are very close to (16). It can be noted that the first and the third pole are slightly shifted but not significantly as seen in Figure 39.

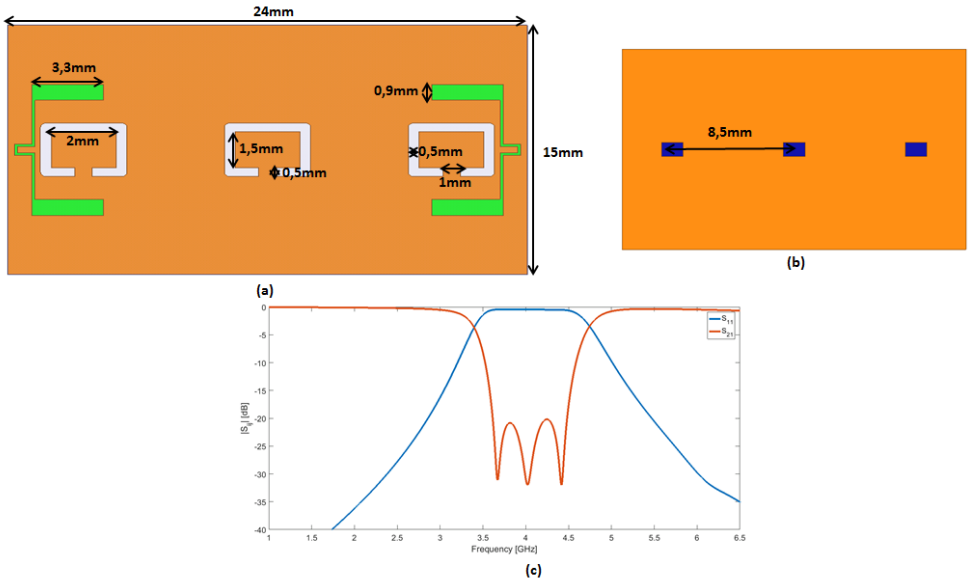

Figure 39: Third order filter design, (a) top view, (b) bottom view, (c) S parameters

The third order filter has a central f_c of 4 GHz and a BW of 1.3GHz, return loss of 20 dB and insertion loss of 0.45 db. By the same method a fourth order filter is designed with an objective f_c of 3.5 GHz and BW of 0.8 GHz. The ideal coupling matrix and the one extracted from the design are (18) and (19) respectively.

$$\begin{bmatrix} 0 & 1 & 0 & 0 & 0 & 0 \\ 1 & 0 & 0.91 & 0 & 0 & 0 \\ 0 & 0.91 & 0 & 0.70 & 0 & 0 \\ 0 & 0 & 0.70 & 0 & 0.91 & 0 \\ 0 & 0 & 0 & 0.91 & 0 & 1 \\ 0 & 0 & 0 & 0 & 1 & 0 \end{bmatrix} \quad (18)$$

$$\begin{bmatrix} 0 & 1.0 & 0 & 0 & 0 & 0 \\ 1 & 0.1 & 0.9 & 0 & 0 & 0 \\ 0 & 0.9 & -0.1 & 0.67 & 0.1 & 0 \\ 0 & 0.1 & 0.67 & 0 & 1 & 0 \\ 0 & 0 & 0.1 & 0.9 & 0.1 & 1 \\ 0 & 0 & 0 & 0 & 1 & 0 \end{bmatrix} \quad (19)$$

Again the coupling matrices are very close each other and thanks to that method the simulation gives a fourth order filter with a fc of 3.4 GHz, a BW of 0.75 GHz and I.L equal to 0.55 dB. The design and the S parameters are illustrated in Figure 40.

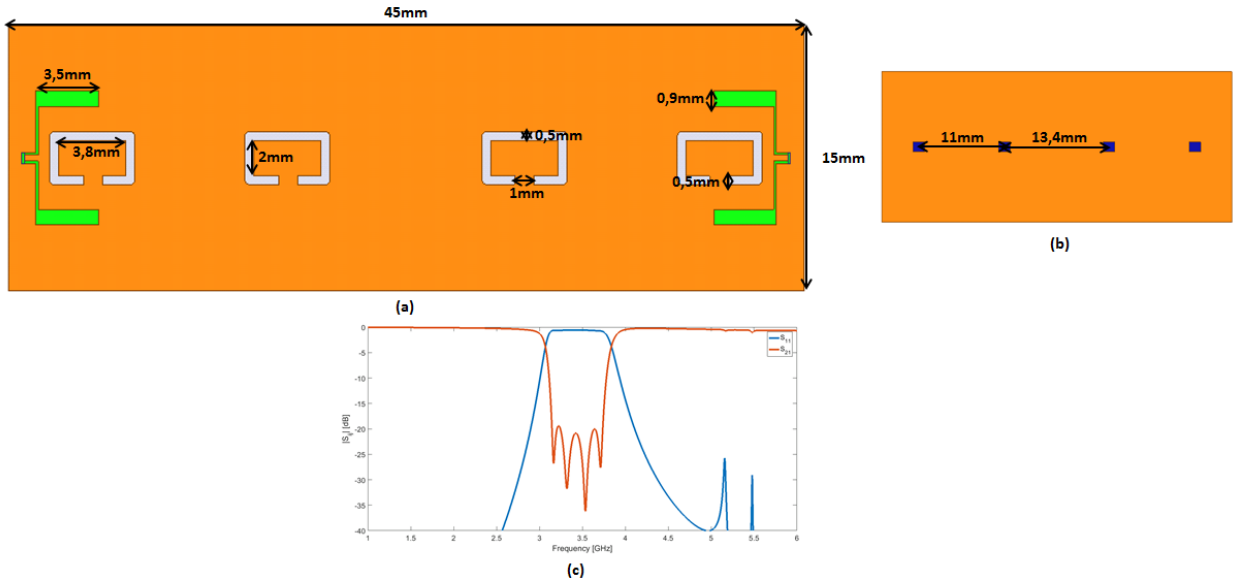

Figure 40: Design of the fourth order filter, (a) top view,(b) bottom view, (c) S parameters

A capacitive effect has been added on each gap of each elementary cell to study the tuning feature. Unfortunately, with those designs it is very difficult to control the inter coupling when the f_c of each cell shifts and we run out of time to make a proper design of such four pole tunable filter.

3.9 Conclusion

In this chapter, a new Alumina based resonator manufactured with SLA process is designed. The unloaded quality factor is interesting (600 in the off state) considering the size of the whole structure and the tuning range (29%). However, it is possible to reduce the size by 34% thanks to effect of the capacitive post (with a height of 1.8mm) to obtain in the end a compact resonator with a Q_0 of 303 with a tuning range of 15%. As seen in Figure 28 this loaded cavity has one of the best tradeoff between the Q_0 and the volume in terms of λ_g compared with the structures from the literature. The reduction factor could be higher if the height of the post is higher than 1.8mm. In a perspective view, another solution could be tested to reduce the whole size and to have a better tuning range by using both the SLA process with a higher relative permittivity material for Alumina and the metamaterial effect of

the first generation cell. Thanks to this 3D manufacturing it is possible to create the same design as the first one and maybe have a potential compact structure with higher tuning range.

The second part of this chapter consists in proving the possibility to create higher order filter based on the elementary cell of the compact resonator. Then a second order tunable filter has been designed with a tuning range of 15%. A third order and fourth order filter with a BW of 1.3 GHz and 0.75 GHz respectively around 4GHz have been designed but unfortunately not manufactured due to lack of time. It could be interesting to make them tunable but in spite of their simple topologies, the inter resonator coupling of high order filter becomes more complex according to the number of resonator. It may not be impossible to tune those filters by adding other capacitive or inductive effects to counterbalance the drift of the inter resonator and access couplings.

The second chapter and this one have studied different elementary cells to be part of the concept depicted in Figure 1 with pros and cons for each. However, the preferred choice is the second generation (not the compact one) because this resonator has the highest Q_0. Therefore the resonance of the structure will be less impacted by the losses from the optically tuning devices and by the sealing process to connect the first “floor” (resonator) to the second one (tuning elements). Besides, the size of the second generation resonator allows us to design the second floor easily because space constraints are less significant than with the compact structure.

3.10 Bibliography

[1] D. M.Pozar, *Microwave Engineering, 3Rd Ed*. Wiley India Pvt. Limited, 2009.

[2] A. Anand, J. Small, D. Peroulis, and X. Liu, "Theory and Design of Octave Tunable Filters With Lumped Tuning Elements," *IEEE Trans. Microw. Theory Tech.*, vol. 61, no. 12, pp. 4353–4364, Dec. 2013.

[3] N. DELHOTE, "Composants céramiques 3D par procédé de stéréolithographie : solutions de filtrage hyperfréquence innovantes," thesis, Université de Limoges.

[4] A. KHALIL, "Technologies LTCC et stéréolithographie céramique 3D appliquées à la conception de dispositifs millimétriques et sub-millimétriques :," thesis, Université de Limoges.

[5] G. F. Craven and C. K. Mok, "The Design of Evanescent Mode Waveguide Bandpass Filters for a Prescribed Insertion Loss Characteristic," *IEEE Trans. Microw. Theory Tech.*, vol. 19, no. 3, pp. 295–308, Mar. 1971.

[6] M. S. Arif and D. Peroulis, "A 6 to 24 GHz continuously tunable, microfabricated, high-Q cavity resonator with electrostatic MEMS actuation," in *Microwave Symposium Digest (MTT), 2012 IEEE MTT-S International*, 2012, pp. 1–3.

[7] H. Joshi, H. H. Sigmarsson, D. Peroulis, and W. J. Chappell, "Highly Loaded Evanescent Cavities for Widely Tunable High-Q Filters," in *Microwave Symposium, 2007. IEEE/MTT-S International*, 2007, pp. 2133–2136.

[8] X. Liu, L. P. B. Katehi, W. J. Chappell, and D. Peroulis, "High- Tunable Microwave Cavity Resonators and Filters Using SOI-Based RF MEMS Tuners," *J. Microelectromechanical Syst.*, vol. 19, no. 4, pp. 774–784, Aug. 2010.

[9] S. Moon, H. H. Sigmarsson, H. Joshi, and W. J. Chappell, "Substrate Integrated Evanescent-Mode Cavity Filter With a 3.5 to 1 Tuning Ratio," *IEEE Microw. Wirel. Compon. Lett.*, vol. 20, no. 8, pp. 450–452, Aug. 2010.

[10] E. J. Naglich, J. Lee, and D. Peroulis, “Tunable bandstop filter with a 17-to-1 upper passband,” in *Microwave Symposium Digest (MTT), 2012 IEEE MTT-S International*, 2012, pp. 1–3.

[11] D. Peroulis, E. Naglich, M. Sinani, and M. Hickle, “Tuned to Resonance: Transfer-Function-Adaptive Filters in Evanescent-Mode Cavity-Resonator Technology,” *IEEE Microw. Mag.*, vol. 15, no. 5, pp. 55–69, Jul. 2014.

[12] P. J. Bártolo, Ed., *Stereolithography*. Boston, MA: Springer US, 2011.

[13] T. Jaffre, L. Leger, B. Jecko, J. Claus, and C. Chaput, “Fabrication of 3-D alumina photonic bandgap structures by laser rapid prototyping- application to the design of three dimensional photonic crystal resonator antenna,” in *17th International Conference on Applied Electromagnetics and Communications, 2003. ICECom 2003*, 2003, pp. 255–258.

[14] F. Giuppi, A. Georgiadis, A. Collado, M. Bozzi, and L. Perregrini, “Tunable SIW cavity backed active antenna oscillator,” *Electron. Lett.*, vol. 46, no. 15, pp. 1053–1055, Jul. 2010.

[15] S. Moon, H. H. Sigmarsson, H. Joshi, and W. J. Chappell, “Substrate Integrated Evanescent-Mode Cavity Filter With a 3.5 to 1 Tuning Ratio,” *IEEE Microw. Wirel. Compon. Lett.*, vol. 20, no. 8, pp. 450–452, Aug. 2010.

[16] X. Liu, L. P. B. Katehi, W. J. Chappell, and D. Peroulis, “High- Tunable Microwave Cavity Resonators and Filters Using SOI-Based RF MEMS Tuners,” *J. Microelectromechanical Syst.*, vol. 19, no. 4, pp. 774–784, Aug. 2010.

[17] M. S. Arif and D. Peroulis, “A 6 to 24 GHz continuously tunable, microfabricated, high-Q cavity resonator with electrostatic MEMS actuation,” in *Microwave Symposium Digest (MTT), 2012 IEEE MTT-S International*, 2012, pp. 1–3.

[18] S. M. Hou, J. H. Lang, A. H. Slocum, A. C. Weber, and J. R. White, “A High- Widely Tunable Gigahertz Electromagnetic Cavity Resonator,” *J. Microelectromechanical Syst.*, vol. 15, no. 6, pp. 1540–1545, Dec. 2006.

[19] H. Joshi, H. H. Sigmarsson, D. Peroulis, and W. J. Chappell, “Highly Loaded Evanescent Cavities for Widely Tunable High-Q Filters,” in *Microwave Symposium, 2007. IEEE/MTT-S International*, 2007, pp. 2133–2136.

[20] S.-J. Park, I. Reines, C. Patel, and G. M. Rebeiz, “High- RF-MEMS 4 #x2013;6-GHz Tunable Evanescent-Mode Cavity Filter,” *IEEE Trans. Microw. Theory Tech.*, vol. 58, no. 2, pp. 381–389, Feb. 2010.

[21] R. J. Cameron, R. Mansour, and C. M. Kudsia, *Microwave Filters for Communication Systems: Fundamentals, Design and Applications*. Wiley, 2007.

[22] [Online] Available: http://epublications.unilim.fr/theses/2009/perigaud-aurelien/perigaud-aurelien.pdf. [Accessed: 08-Jul-2016].

Chapter 4: Optical tunability

4.1 Introduction

To fulfill the concept and the realization of optically controlled tunable components, functional *direct optical control* with an optically sensitive material (i.e. whose dielectric constant varies with light) or *indirect optical control* with an optically controlled device (i.e. photosensitive diode or switch) need to be developed.

This chapter gives a review for actual photosensitive materials which may be useful for our application. Then, a material compatible with our needs is chosen to perform simulations with HFSS software to study the variation of the scattering parameters of the generation one filter previously explained in Chapter 2. A novel concept of optically controlled RF switch is investigated as well to achieve low ON-state insertion loss. Enhancements are also proposed to improve the S_{21} of such switch for decreasing the loss of the whole system which combines the alumina based resonator (second generation) and the optical tuning system.

4.2 Photosensitive Material-direct optical control

4.2.1 Principle

Certain electronic devices such as photodiodes are designed to be sensitive to light generation conduction (or electron-holes pairs). This well-known phenomenon is based on the emission of electrons when the material is lighted.

If the light has a sufficient energy the electrical conductivity of certain materials increases when they are exposed too. Therefore, a second effect appears called the photoconductivity. When light is absorbed by a material such as semiconductor, the number of free electrons (negative charge) and electron holes (positive charge) changes and increases its electrical conductivity. But the light which strikes the semi-conductor has to be sufficient enough to permit the electrons to raise across the band gap (from the valence gap to conduction gap). The most common photoconductive material are silicon, germanium, and cadmium sulfide. Some devices can be found in the literature using the photoconductive effect such as [1][2].

The photorefractive effect is a nonlinear optical effect which exists in certain crystals and others materials that respond to light by altering their refractive index. The photorefractive effect is observed in materials which are both electro-optic and photoconducting. When an incident light strikes the material, charges that are photogenerated in the illuminated regions, migrate and eventually get trapped at the dark regions of the sample. Therefore, the resulting charge redistribution creates an internal electric field which changes the refractive index via electrooptic effect.

4.2.2 Review of photosensitive material

4.2.2.1 Zinc oxide (ZnO)

Zinc oxide is a photoconductive material as well as a piezoelectric optoelectronic and n-type semiconductor. This inorganic compound has a good transparency, high electron mobility and a wide bandgap. This material is also stable under normal pressure and temperature conditions and harmless. Zinc oxide films can be deposited by different methods: evaporation, chemical vapor deposition (CVD), sputtering, spin-coating, etc.

Materials based on ZnO have potential application for transparent thin film transistor, surface acoustic wave (SAW) devices, light emitting devices and photoconductive sensors[3] and switches [4].

ZnO is used once doped with other materials as Gallium (Ga)[5], Magnesium (Mg) or Aluminum (Al)[6]. By doing that the band gap increases and semiconductors with wide band-gap permit devices to operate at much higher voltages, frequencies and temperature.

Different tests were made during the thesis of Dr Gonzales J.M [7]. He shows that the conductivity (σ) of ZnO is about 0.36×10^{-3} S/m in the dark environment and goes up to $\sigma=2.2\times10^{-2}$ S/m when the material is illuminated at low frequencies which is too low for creating tunable devices with a sufficient change. This conclusion comes from an experiment which consists in putting down a sample of this material in a coplanar structure and see the change on S parameters (Figure 1) by lighted it with a UV source.

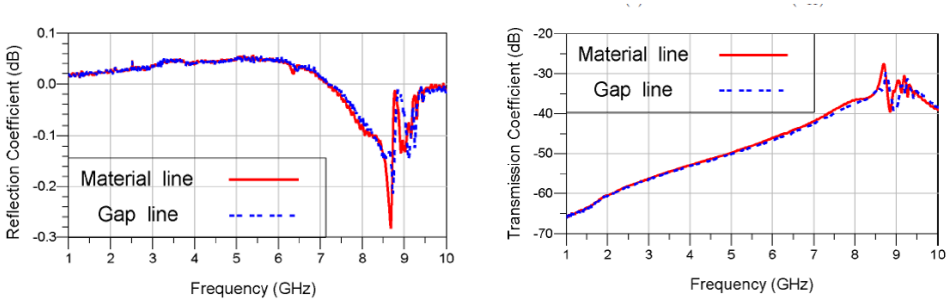

(a) Reflection coefficient (S_{11}). (b) Transmission coefficient (S_{21}).

Figure 1: Measured results of the coplanar line with a gap in the center conductor [7]

4.2.2.2 Vanadium Dioxide (VO2)

The next material is a photoconductive one too, but it is very sensitive to the temperature (or thermosensitive). Vanadium Dioxide presents the particularity of transiting between an isolating state to a metallic one. The transition gives the material a modification of its electrical and optical properties. The conductivity increases and also the reflectivity especially in the infrared domain.

The deposition of the vanadium dioxide can be made thanks to several methods such as laser ablation. This technique permits having great quality films which present very interesting properties with a very big change on the conductivity between the two states [8]. This technique allows the deposition over big surfaces (≈ 10cm in diameter).

Some characterization of this material has been carried out at Xlim at DC and for high frequencies [9]. At ambient temperature the conductivity is low (lower than 100 $S.m^{-1}$). If the temperature increases up to 72°C the transition appears and then a sudden change of the conductivity is noticed (metallic state). If the temperature is higher than 90°C the conductivity is about 10^6 $S.m^{-1}$. The transition is reversible but with a hysteresis effect. A characterization at high frequencies shows a transmission around 0 dB (isolating state) if the temperature is around 25°C and of -25dB when the temperature increases up to 95°C (metallic state) as illustrated in (Figure 2).

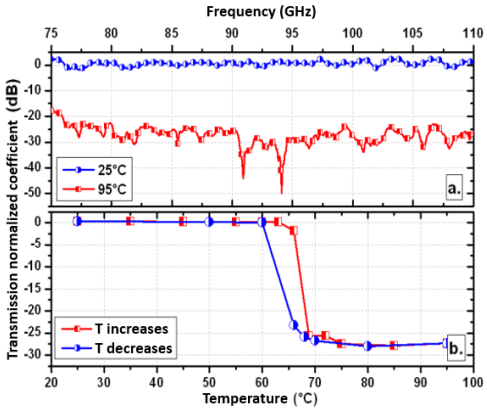

Figure 2 : Measured transmission of a VO2 film from 25 to 95 for a frequency band between 75-110 GHz (a) and an associated hysteresis cycle (b)[9]

This material is really promising for creating tunable filter devices. But the thickness control will be crucial for developing a good quality microwave device. Indeed, VO_2 films are very thin (100nm), not even a few skin depths, so a big part of the electromagnetic waves will pass through and the devices will not behave properly.

4.2.2.3 Nano-crystalline Silicon (nc-Si)

Silicon (Si) is the main component for most semiconductor devices and integrated circuits. This material is widely used because it is still a semiconductor in high temperature environment and because its native oxide is easily grown in a furnace and forms a good semiconductor/dielectric interface.

This semiconductor has an indirect bandgap of 1.1eV corresponding to an infrared wavelength of 1.1µm. As a result, this material is photosensitive, which is an unwanted feature but interesting feature for photosensitive devices as switches as seen later in the thesis.

The dielectric material properties of silicon can be changed with the used of a suitable optical source namely with an appropriate wavelength and intensity to induce a plasma in the semiconductor material. A large amount of work has been carried out exciting silicon plasma regions [10] as well as filter based on that property [11].

A study was done [7] to create a photoconductive material by using nano-particles in a polymer material to create an direct bandgap material. It enhances the sensitivity to light with

a good rejection ratio. These particles were mixed with 3571 dielectric polymer from DuPont at first. In the second iteration the polymer was replaced with epoxy. However, these two host materials have micro-particles instead of nano-particles and show no significant changes between the dark and the light state. Indeed the particle's size has not small enough to produce a change in a bandgap. From the literature, the material is expected to be a good photoconductive material.

4.2.2.4 Cadmium Sulfide (CdS)

4.2.2.4.1 Theory

This material is a composite photorefractive material consisting of photoconductive spheres dispersed in an insulating polymer. Changing the conductivity of spheres changes the effective permittivity of the material as a result. The temperature has an effect on a photoconductivity of the spheres as well but this change is too small to be useful.

The particles used are cadmium sulfide (CdS) spheres with a radius of 1 μm. The features of bulk CdS extracted from [12] are as follows:

- Electron mobility μ_e =160cm^2/Vs
- Hole mobility μ_h=15cm^2/Vs
- Low frequency or static relative permittivity: $\varepsilon_r(0)$=8.5
- Relative permittivity in the optical range: $\varepsilon_r(\infty)$=5.26
- Minority carrier life time : τ is 22.3μs to 57.4 μs
- Bandgap is 2.4 eV

The bandgap is 2.4 eV which means the wavelengths has to be shorter than 520 nm to absorb and create a single electron-hole pair as it can be deduced from

$$E(eV) = h\nu = \frac{hc_0}{\lambda} = \frac{(4.136\times10^{-15})(3\times10^{8})}{\lambda} \approx \frac{1240\ eV\ nm}{\lambda} \qquad (1)$$

With h the Planck constant and c_0 the speed of light in vacuum.

This photorefractive material was prepared by Prof. Steven McGarry and characterized by J.M Gonzales and N. Jess [7],[20]. The extracted values for the material under dark and light condition are the following:

Property	Value (dark)	Value (light)
Electric permittivity (ε_r)	4	4.6
Loss tangent (tan δ)	0.05	0.12

Table 1: RF parameters under dark and light conditions at 8 GHz [7]

The $\Delta\varepsilon_r$ is 0.6 or 15% which is quite smallfor tunable microwave devices. Nevertheless a simple simulation was performed to quantify the impact of such photosensitive medium with microwave component.

4.2.2.4.2 Simulations

The SIW filter made up of electrical vias and interdigital capacitance illustrated and explained in chapter 2 is used to evaluate the potential of such a photorefractive material (with a too small variation of permittivity) to be interesting for tuning applications. The filter is shown Figure 3.

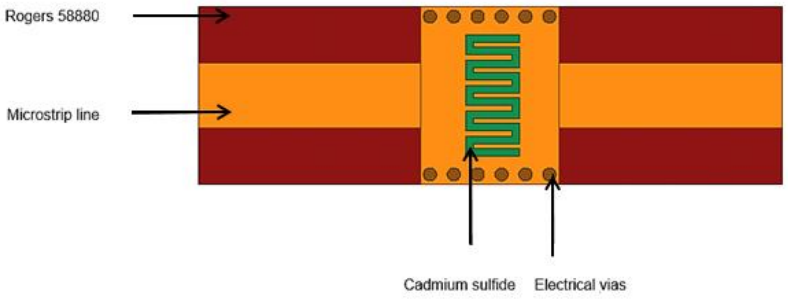

Figure 3 : First generation one filter with cadmium sulfide

The etched capacitance is used for both creating a capacitance effect of course and for being a cradle which can receive the cadmium sulfide. Therefore two simple simulations are done with HFSS that consist in including electrical parameters for dark state for the first one and light state for the other. Because of the small variation of the photosensitive material

permittivity between two states, the frequency shift of the frequency resonance f_0 is too low: about 10 MHz.

A lot of simulations were performed to increase this shift, namely variations of the length, width, numbers of fingers and the height of the etched gap. Unfortunately the design of the capacitance or rather the form of the material set up into the cradle has no influence on the frequency response contrary to the intrinsic electrical parameters of the material. Therefore another technology will be used to fulfill the main goal of this thesis with indirect optical control.

4.3 Optically controlled RF switch-indirect optical control

4.3.1 Concept

This work is based on [13] and proposes a single-FET RF switch (providing low/high impedance path between drain and source with the transistor ON/OFF[14][15]), by bringing the V_{gs} above or below the threshold voltage (V_t) with the dark or illuminated photodiode monolithically integrated gate of the MOSFET.

Devices fabricated in a Si CMOS process are normally very sensitive to optical illumination as silicon is sensitive to light, even broadband lamp or LED. In order to avoid this sensitivity CMOS circuits are by default shielded with the top metal layers that prevent the light from getting to lower layers of device. In order to create photodiodes sensitive to visible light sources, these protective layers can be removed from the top of the p-n junction of a common diode. In this way, when the chip is illuminated, the light will excite the carriers on the silicon and the p-n junction creates a voltage at the terminals of the photodiode.

The technology used is a standard 0.13 µm Si CMOS technology form IBM industry. This process includes FET structures that support High-Frequency RF-compatible models, a wide range of optional passive devices and wiring with a thick last metal (4µm). A high-quality analogue design ensures close correlation between measurements and simulations. This technology is an excellent candidate for low-cost, high performance wireless applications such as Bluetooth or Wi-Fi. This CMOS process is made up of:

- Up to 8 layers: three thin (0.29 µm, 0.35µm and 0.32µm), two thick (0.55µm) and three thick RF-top metal (0.46µm, 3µm and 4µm).
- Supply voltage: VDD=1.2V core and VDD 2.5V input/output.
- Substrate resistivity of 1-2 Ω.cm.
- Twin well CMOS technology on non-epi P^- substrate.
- Shallow trench isolation.
- Dual gate oxide with physical thickness of 2.2nm and 5.2nm.
- Minimum lithographic image of 0.12µm.
- Low resistance Co silicided N^+ and P^+.
- Wire-bond pads or controlled collapse chip connections.

The cross section of the process is illustrated with the different layers used in Figure 4[16].

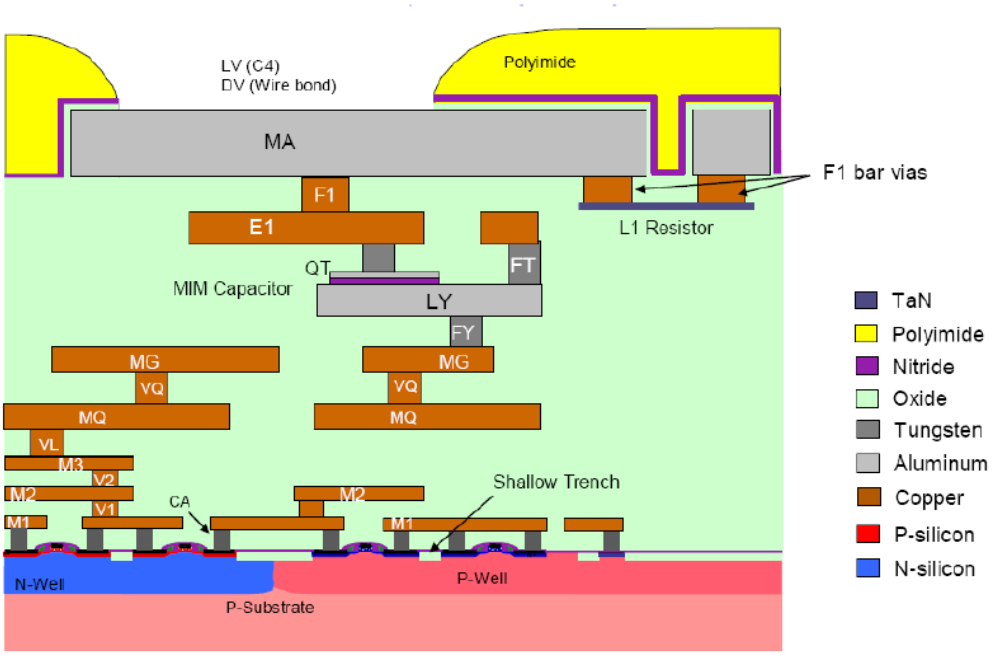

Figure 4: Cross section of the IBM CMOS 0.13 µm technology [16]

The main technical challenges of an optically controlled CMOS RF switch are the generation of a sufficient photo-induced gate voltage using small area photodiodes, and the achievement in the RF path of low ON-state insertion loss and high OFF-state isolation using no external bias.

To fulfil this goal a MOSFET with a P-type substrate is chosen (which is a single-crystal silicon wafer that provides physical support for the device). The source and the drain are two doped n-regions created in the substrate. An electrical insulator (SiO_2) is grown on the surface of the substrate, covering the area between the source and the drain region. The thickness of this layer is usually called t_{ox} and its value is typically from 2 to 50 nm [17] . The gate electrode is form with deposited metal on top of the oxide layer; the metal contacts are also made to the source region, the drain region, and the substrate, also known as the body. The physical structure of a p-type MOSFET is illustrated in Figure 5: Cross section of an NMOS transistor [17]

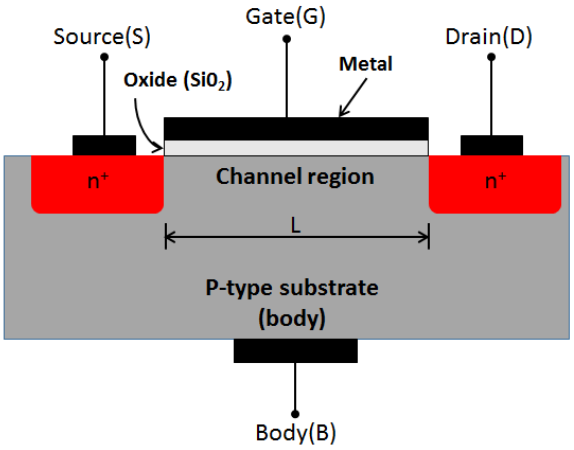

Figure 5: Cross section of an NMOS transistor [17]

4.3.2 Optically RF switch-OFF mode

When V_{GS}=0V , there is no bias applied voltage, then two back to back diodes exist in series between drain and source. One diode is formed by the pn junction between the n^+ drain region and the p-type substrate and the other diode is formed by the other pn junction between the substrate and the n^+ source region as illustrated in. These back to back diodes prevent current conduction form drain to source when a voltage V_{ds} is applied. In fact, the path between drain and source has very high resistance (of the order of $10^{12}\Omega$).

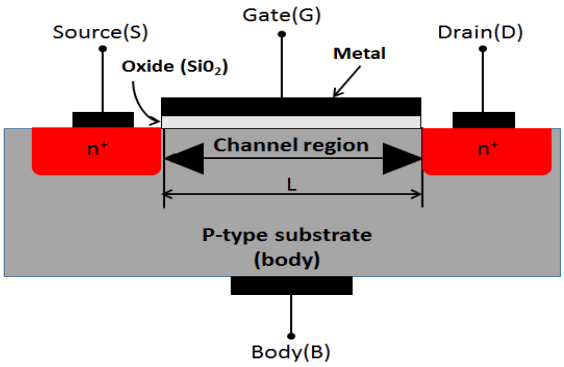

Figure 6: NMOS transistor with no voltage applied to the gate

4.3.3 Optically RF switch-ON mode

When both the source and the drain are grounded and a voltage is applied to the gate, free holes (positively charged) are repelled from the region of the substrate under the gate into the substrate, leaving behind a carrier-depletion region. On top of that the positive gate voltage attracts electrons from the n^+ source and drain regions into the channel region. When a sufficient number of electrons accumulate near the surface under the gate, a n region is created, connecting the source and the drain regions. The induced n region forms a channel for current flow from drain to source [17].

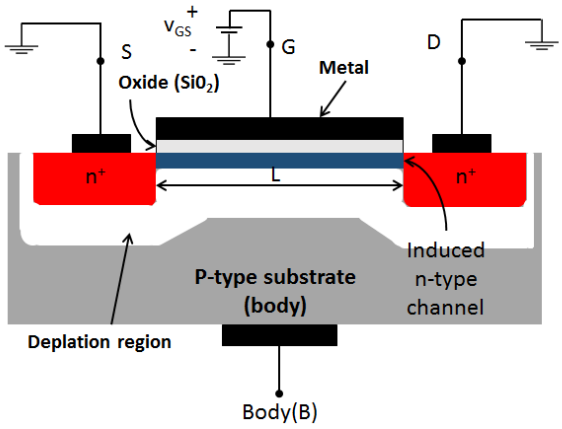

Figure 7: NMOS transistor with a positive voltage applied to the gate and an induced n channel [17].

The value of V_{GS} at which a sufficient number of electrons accumulate in the channel region to form a conducting channel is the threshold voltage (V_T). This intrinsic value is controlled during device fabrication and lies in the range of 0.5V to 1.0V. The higher the

voltage (V_{GS}), the more the MOSFET can conduct which means a broader channel and a lower ON state impedance. Indeed, the conductance of the channel is proportional to the excess gate voltage (V_{GS}-V_t) as well as the current I_D. When the switch is conducting, it typically operates in the linear (triode region) mode of operation since the source and drain voltages are nearly equal. The device operates as a linear resistor whose value is controlled by VGS.

A parallel plate capacitor is formed between the gate and the channel region of the MOSFET with the oxide layer acting as the dielectric. Since V_{GS} is higher than zero, positive charges accumulate on the top of plate of the capacitor (the gate electrode). Electrons propagate trough the induced channel and then create negative charge on the bottom plate. Thus, an electric field is developed in the vertical direction and that field controls the amount of charge in the channel. Therefore it determines the channel conductivity and the current that flows through the channel when a voltage V_{DS} is applied.

The V_{GS} voltage is controlled thanks to the use of photodiode in this thesis. In [7], some "opto-switches" were fabricated with IBM's 0.13µm process. Three photodiodes were connected to the gate of the MOSFET as seen in Figure 8, which control the ON/OFF state of the transistor itself. The drain and the source constitute the RF input and output ports respectively.

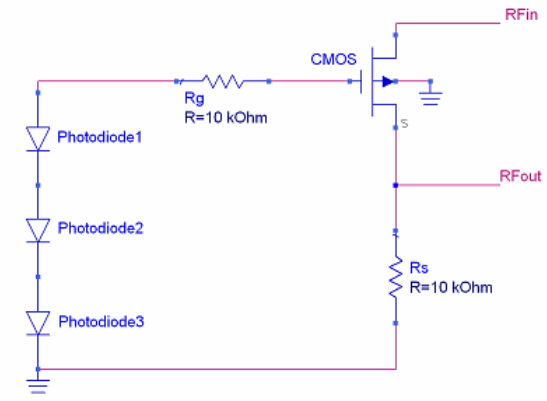

Figure 8: Circuit schematic of the RF CMOS switch [7]

The results from 200MHz to 2.2 GHz are in Figure 9. The light source used is an Oriel quartz tungsten lamp (bulb 6333, with maximal emission at a wavelength around 760nm) with a relatively low optical power applied to the RF switch of 20nW. Those results confirm the

switching operation of the circuit with more a difference between the ON and the OFF state higher than 20 dB at 2.2 GHz. However, the S_{21} parameter is -6.8dB which is too high for creating a tunable resonator with optical control.

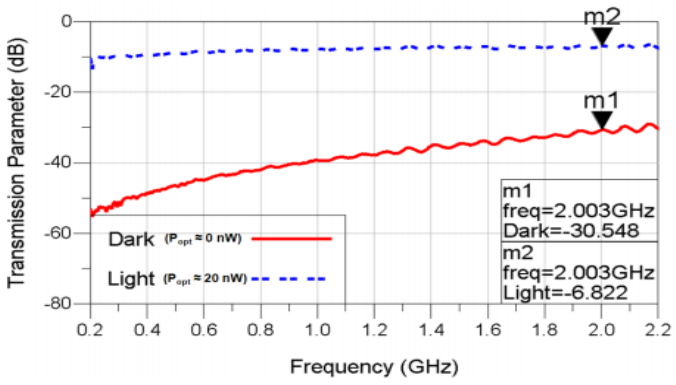

Figure 9: RF measurements of the zero-biased switch [7]

4.3.4 Investigations

4.3.4.1 Preliminary results

The preliminary devices in [7] are too lossy for our application. Then, new switches were created with different features namely the thickness of the oxide layer and the width of the gate. Those new components give a better understanding about the impact of physical elements on the S_{21} parameters. For measuring this device at RF frequencies an Agilent 8722ES Vector Network Analyzer (VNA) and the apparatus shown in Figure 10 are used to make the transition between the SMA connector of the VNA and the pads of the RF switch. The ON/OFF components are glued with conductive epoxy between two 50Ω coplanar lines. All the results are presented in Table 2.

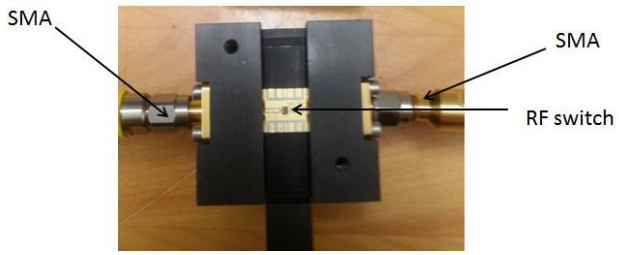

Figure 10: Picture of the RF test fixture

Config	1	2	3	4	5	6
Chip	S_{21} [dB]	S_{21} [dB]	S_{21} [dB]	S_{21} [dB]	S_{21} [dB]	S_{21} [dB]
1	-4.1	-4.3	-7.9	-3.3	-14.3	-13.7
2	-4.1	-4.2	-7.8	-3.4	-14.2	-14.2
3	-3.8	-4.1	-8.1	-3.1	-14.5	-14.1
4	-4.1	-4.1	-7.9	-3.3	-14.5	-13.8
5	-4.1	-4.2	-8.1	-3.4	-15.3	-14.3
6	-3.8	-3.8	-8.0	-3.1	-14.4	-13.6

	Gate width [µm]	Length of channel[nm]	Oxide thickness [nm]
1	50	130	2
2	50	130	2
3	80	130	6
4	80	130	2
5	50	130	6
6	50	130	6

Table 2: Measurements of different optical switches in ON state (with V_{GS}=3V) at 2.5 GHz

Several observations can be made from Table 2. The addition of the fourth photodiode does not improve the insertion. It appears that the configuration 4 has the smallest S_{21} parameters because the parallel plate capacitor C_{ox} is the highest for this configuration and then the current that flows in the channel has the highest value as well. But the transmission loss is still too high (-3.1dB) for typical switching applications. This is why we will investigate different designs to maximize the I_{DS} current.

4.3.4.2 Maximizing I_{DS}

4.3.4.2.1 Approach

The current that flows through the channel depends on many physical parameters as seen in (2) [17].

$$I_{ds} = \mu_n \times C_{ox} \times \frac{W}{L}\left[(V_{GS} - V_t)V_{DS} - \frac{1}{2}{V_{DS}}^2\right] \quad (2)$$

With:

- μ_n: mobility of electrons in the channel as called as surface mobility
- C_{ox} :parallel plate capacitor formed by the gate and the channel
- W: width of the channel
- L : length of the channel
- V_t : threshold voltage

The current in the channel is proportional to the ratio of the channel width W by the channel length L. Those values can be selected by the circuit designer to maximize or reduce the current I_{DS}. However, for a given fabrication process there is a minimal channel length L_{min}. This parameter characterizes the process and in our case the L_{min} is 0.13µm. Moreover W cannot be higher than 80µm according to the IBM's process manual [16]. In Table 2 the configuration 4 has already optimized values for W and L therefore to increase current I_{ds} the capacitance C_{ox} must be higher. Again, the configuration 4 has the thinnest oxide layer namely 2nm. Then, the only value with this technology which can increase the value of the current channel is the threshold voltage V_t.

Indeed in order to maximize the current from drain-source (I_{DS}) to improve the ON state performance of the MOSFET, the threshold voltage has to be as low as possible. Therefore in the second manufacturing, low threshold voltage transistors are used with a V_t of 260mV instead of 355mV for the ones used in Table 2. Moreover another approach is used by taking the same transistors used for the configuration 4 in Table 2. But in this case, the V_t of the MOSFET can change with the use of photodiodes connected to the body of the substrate. Indeed according to [17]:

$$V_t = V_{t0} + \gamma\left[\sqrt{2\phi_f - V_{BS}} - \sqrt{2\phi_f}\right] \quad (3)$$

With :

- V_{t0}: the threshold voltage for V_{SB}=0V
- V_{SB}: the voltage applied on the body
- ϕ_f: a physical parameter with ($2\phi_f$) typically 0.6V
- γ: a fabrication-process parameter given by:

$$\gamma = \frac{\sqrt{2qN_A\varepsilon_S}}{C_{ox}} \quad (4)$$

Where q is the electron charge (1.6×10^{-19}C); N_A is the doping concentration of p-type substrate and ε_S is the permittivity of silicon.

However if V_{BS} is too high more negative charges will be in the N induced channel and a mirroring effect will appear. This effect will balance those negative charges by adding positive charges on the gate, therefore the V_t will increase so I_{ds} will decrease and it is called the body effect. For doing that a triple well process is used with IBM CMOS 0.13µm technology depicted in Figure 11 . This method is employed to obtain a dynamically varying threshold voltage. On top of that, we can connect photodiodes on the N-Well port in order to reduce the leakage current which appears if the voltage applied to the body is too high.

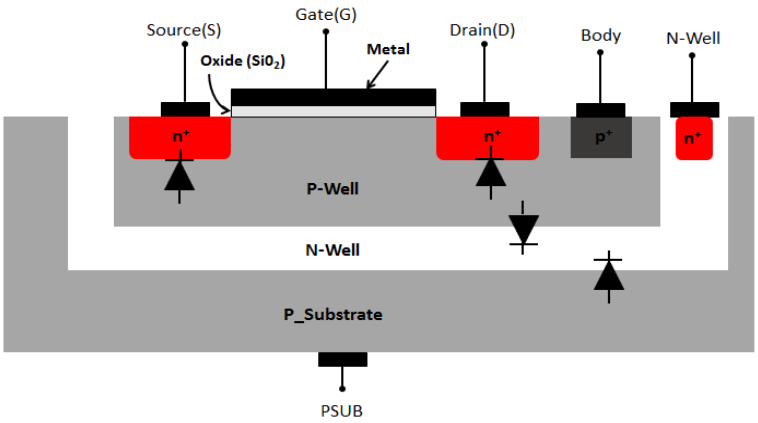

Figure 11: Cross section of an NMOS transistor with triple well process

In addition, to carry out a full characterization of the optical switch many pads must be added in order to access different device nodes and make various connections of the photodiodes. The different designs prepared for the final chips are as follows:

1. A design with 5 series photodiodes for the DC characterization. It is possible to select the number of active photodiodes (0,1,2,3 or 5). This design will be useful to analyze the induced voltage.
2. A design with low threshold voltage connected to 4 pads (ground, RFin, RFout and the gate). Thanks to the latter a voltage injection can be applied to measure the optimized voltage that the transistor requires for a low S_{21}.
3. A design with three photodiodes connected to the gate of a low threshold voltage transistor with pads for RF characterization and the ground. The number of active photodiodes can be chosen by connecting to the proper ground pads (0,1,2 or 3 photodiodes).

4. A design with three pads connected to the gate, the body and to the N-well of the n-FET triple well transistor. Indeed given the triple well process a voltage can be applied to the parts of the transistor. As a result the V_t of the transistor can be changed by applying a voltage. With this design, measured voltage values can be found to optimize the insertion loss of the transistor (or equivalently increase the I_{DS})
5. The last design is the same as the previous one but instead of having pads for voltage injection, the photodiodes are connected to the gate, the body and the N-Well of the NMOS transistor in order to create a full optically controlled (bias-free) RF switch based on the triple well process as shown in Figure 12.

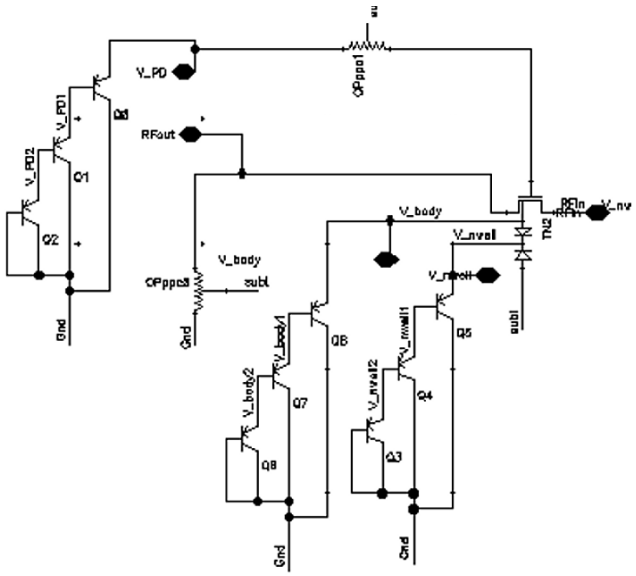

Figure 12: Full optically controlled (bias-free) RF switch layout

The layout of the entire containing the 5 designs described above is illustrated in Figure 13

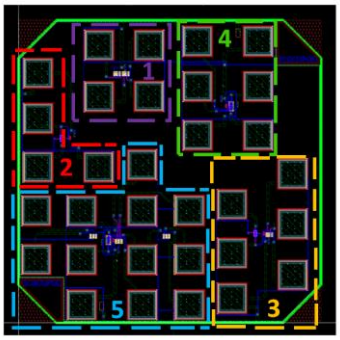

Figure 13: Layout of the 1mm ×1,1mm chip on CADENCE (with 0,11mm × 0,11mm pads)

4.3.4.3 Measurements

Unfortunately, during the design we forgot to remove the silicide layer which is a thin layer of metal which protects the silicon. Then the majority of photons are reflected by this and cannot go through and therefore a low induced voltage is created. But it is still possible to characterize the switches, namely the low threshold voltage transistor and the transistor with body and N-well connections, by simulating the action of photodiodes with voltage supplies. The chips are connected to 50Ω coplanar lines with DC pads on both sides of these lines. Thanks to the apparatus illustrated in Figure 14 DC pins connect the DC pads and are linked to voltage supplies. So with a proper wire bonding the switches can be turn OFF or ON depending on the values of V_{GS} and optimized with V_{body} and V_{nwell}.

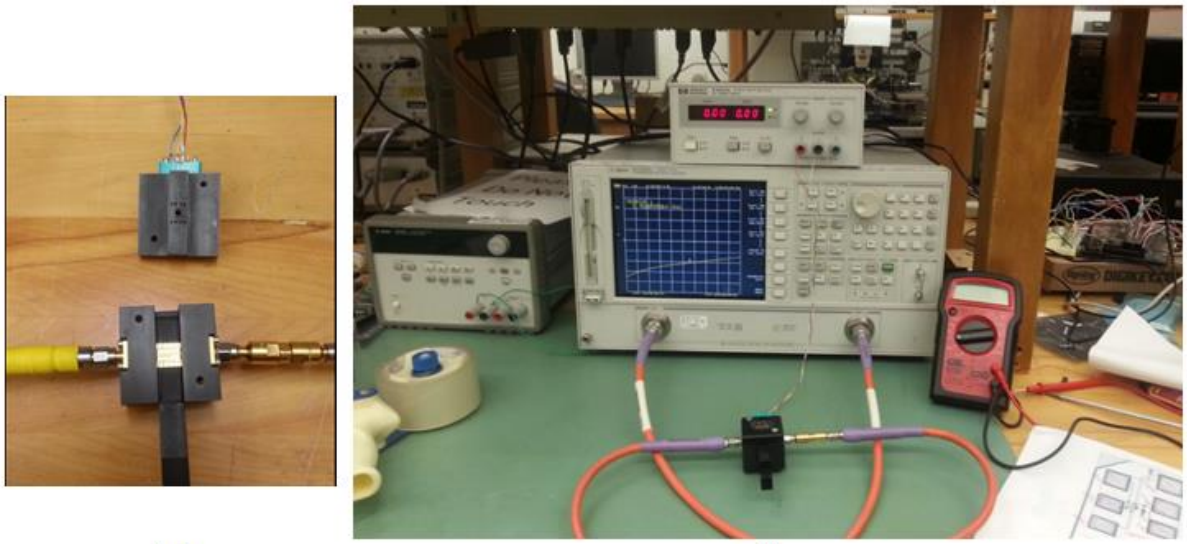

Figure 14: (a) Test fixture, (b) complete characterization bench

The first measurement is about the Low Threshold Voltage (LTV) transistor. The V_{GS} varies from 0V to 3V. The S_{21} parameters are registered with 0.5V steps as seen in Table 3. For the OFF state the insertion loss is about 19dB and the best result for the ON state is 1.35dB which is better than the preliminary results (3.1dB). The S_{21} parameters stop increasing significantly for a V_{GS} higher than 2V (Figure 15).

	V_{GS} [V]	S_{21} [dB]
Low threshold voltage	0	-19.3
	0.5	-6.3
	1	-2.3
	1.5	-1.6
	2	-1.45
	2.5	-138
	3	-1.35

Table 3: Extracted results of S_{21} parameters of LTV transistor at 2.5 GHz

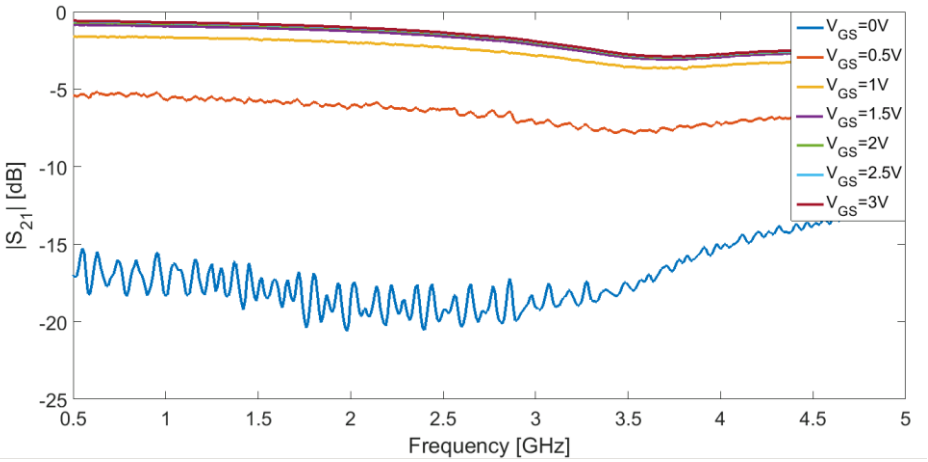

Figure 15: S_{21} parameters of LTV transistor

The same process is applied for the second measurements. But in this case, the N-FET transistor with DC pads connected to the gate, the N-well and the body is chosen. First of all, only the gate of the transistor is connected to a voltage supply, the body and the N-Well are connected to the ground. The results are close to the values from the Table 3 except for the OFF state with insertion loss of 13.2dB (Table 4 and Figure 16). The N-FET is the same as the configuration number 4 in Table 2 but the S_{21} parameter is enhanced for the best case (1.35dB instead of 3.1dB) because we noticed that the photodiodes are connected to the ground except for the first one. Then only one photodiode produces induced voltage instead of three for the new design. On top of that, due to the triple well process, the isolation is worse (13V).

Then, when the V_{body} increases the insertion loss decreases but if V_{body} is higher than 0.6V they increase due to the current leakage. However the impact of this method is minimal since the S_{21} improves only by 0.08dB. Also, when a voltage is applied on $V_{N\text{-}Well}$ the S_{21} parameter is better. As we thought, this part of the transistor reduces the leakage current coming from the high value of V_{body}.

Even though using the triple well process for biasing the V_{body} with the help of photodiode does not have the impact as firstly thought, this approach is interesting for low power and high speed operation according to [18]. Having such a switch with enhanced performance and low power actuation could be beneficial for miniaturized tunable system. In

the next section, we are going to talk about a technology which allows a better performance for RF switches.

N-FET	V_{GS} [V]	S_{21} [dB]	V_{GS}=1.5V $V_{N\text{-}Well}$=0V	V_{body} [V]	S_{21} [dB]	V_{GS}=1.5V V_{body}=0.8V	$V_{N\text{-}Well}$ [V]	S_{21} [dB]
	0	-13.2		0	-1.65		0	-1.68
	0.5	-2.83		0.1	-1.63		0.1	-1.64
	1	-1.76		0.2	-1.61		0.3	-1.61
	1.5	-1.65		0.3	-1.6		0.5	1.58
	2	-1.63		0.4	-1.59		1	1.58
	2.5	-1.36		0.5	-1.58		1.5	1.58
	3	-1.35		0.6	-1.57			
				0.7	-1.66			
				0.8	-1.68			

Table 4: Extracted values of the N-FET with connections on gate, body and N-Well

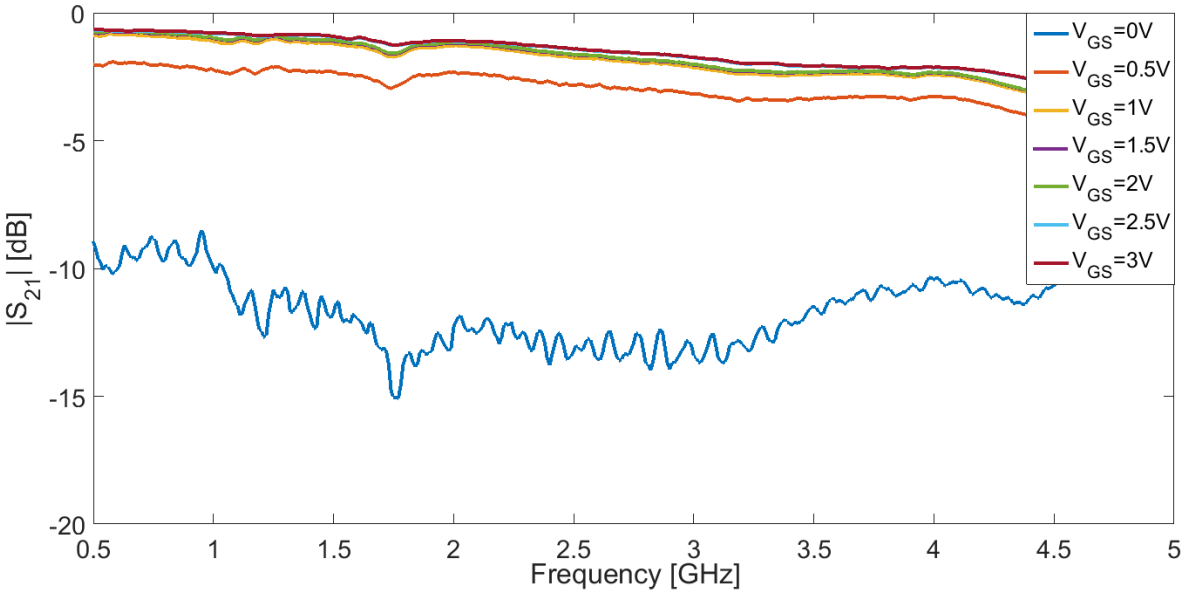

Figure 16: S_{21} parameter for the N-FET transistor

4.3.4.4 Substrate On Insulator (SOI) technology

The solution to enhance the performance of the switches is to reduce the length of the channel according to (2). The SOI technology has emerged over the last years and has taken a big part of the mobile RF world. Indeed, the RF SOI has established itself as the technology of choice for cellular, Wi-Fi and 4G thanks to its intrinsic properties such as Low on-resistance for reduced insertion loss, low off capacitance, substrate parasitics for high

isolation, high Q and low cost manufacturing. Those features come from the fact that an insulator layer is added just below the n^+ doping regions (for a NMOS) and the induced channel to decrease the quantity of leakage current going through the substrate and therefore allowing the reduction of channel length. The RF SOI has many advantages compared to GaAs, SiGe and CMOS technologies as seen in Figure 17[19]

Figure 17: Comparison of manufacturing technology [19]

This technology is very interesting for manufacturing full optically controlled RF switches with better performance than 0.13µm CMOS technology. On top of that, the body biasing to enhance the speed and the power actuation of the component is still possible with CMOS-SOI process manufacturing.

Because of the silicide layer, our switches are not optically controlled. However, the concept of optically tunable filter depicted several times throughout the thesis could be verified thanks to a design explained and illustrated in the next section.

4.4 Concept of tunable filter with optical control

The elementary cell taken for doing such a structure is the second generation resonator because of its high unloaded quality factor of 600 for the OFF state which is needed with the use of not optimized switches like the ones describes in the last section. On top of that, the size of the resonator can extend the space constraints for designing the level number 2 (Figure 1- General Introduction). This first floor has to receive switches and a SMT capacitance. So different gaps are etched over metallized Rogers 5880 substrate (Figure 18): one for the capacitance and four for the switches. Multiple pads are created as well in order to wire bond

the RF switches and apply voltages on them. Five 0.8mm diameter electrical vias are designed to connect the first level and second one (four for the ground and one for the RF signal). The back side of this second floor has metallized squares just below the vias in order to make a proper connection with tin micro balls to ensure the good electrical continuity from the resonator to the capacitance and the switches.

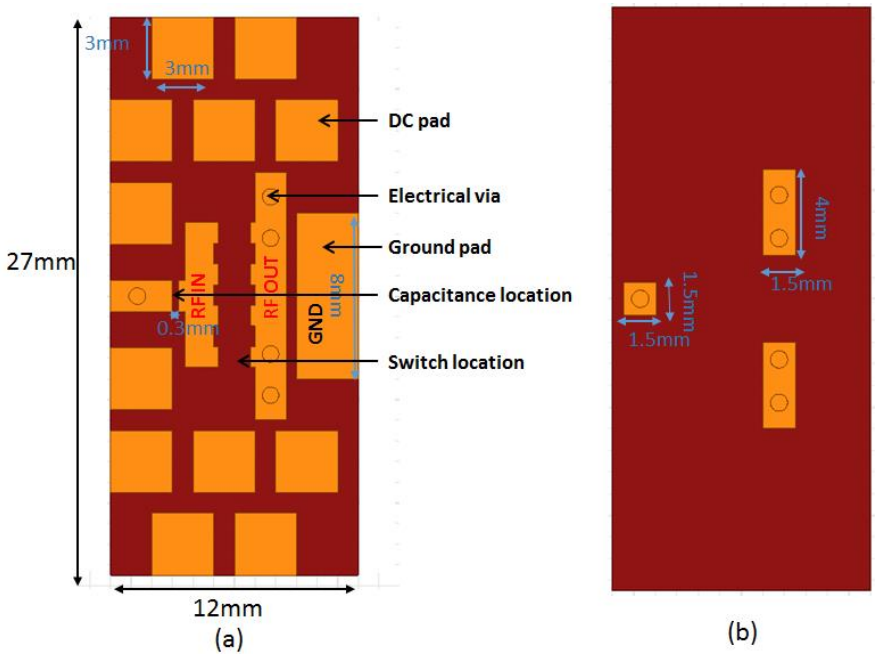

Figure 18: Second level design, (a) front side, (b) back side

The RF signal goes up thanks to the first electrical via, goes through the SMT capacitance and the RF switches, and finally goes down thanks to four vias connected to the part of the resonator located after the etched gap as seen in Figure 19. The number of vias right after switches has to be higher than two to ensure the connection as seen in Table 5 . Indeed the insertion loss improves with two vias but not after this number. However, having four vias allow the sealing process to be more accurate since the vias are used as reference points to align correctly the first and the second level and then to ensure the electrical connection. Regarding the number of switches, four is chosen because it is a good tradeoff between the number of available component we have and the insertion loss. As seen in Table 5, the insertion loss decreases when the number of switches increases. Indeed, we simulate on HFSS those components as a resistance (Ron for the ON state) of 17Ω , found by matching the value of the resistance with S parameters simulation on ADS software corresponding to

the best results of Table 3.Then, putting in parallel multiple resistances can decrease the whole equivalent resistance down to 4.5Ω with four switches.

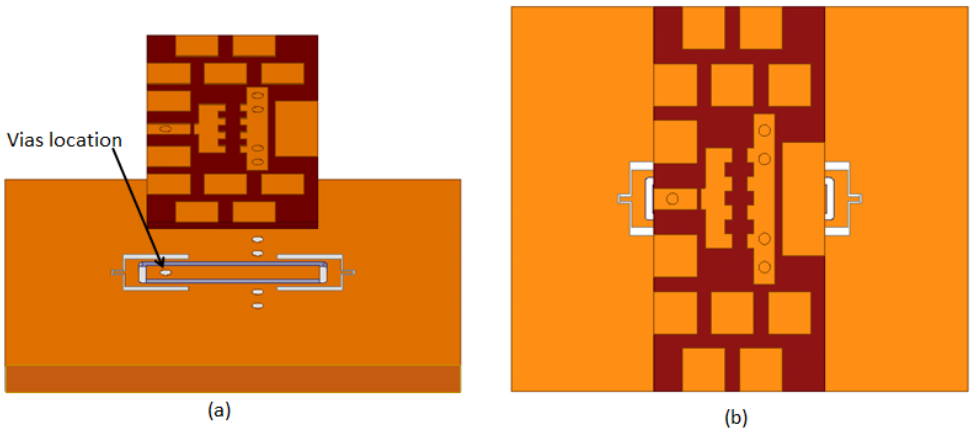

Figure 19: Design of the resonator with SMT capacitance and RF switches, (a) exploded view, (b) upper view

Number of vias	Capa [pF]	Insertion loss [dB]
1	0	1
	0.5	3
	1	6.3
	1.5	9
	2	11.8
2	0	0.6
	0.5	1.3
	1	2.5
	1.5	4.2
	2	5.7
3	0	0.6
	0.5	1.3
	1	2.6
	1.5	4
	2	5.7
4	0	0.6
	0.5	1.3
	1	2.5
	1.5	4
	2	5.7

Number of Switches	Capa [pF]	Insertion loss [dB]
1	0	0.6
	0.5	5.1
	1	10.7
	1.5	15.5
	2	19
2	0	0.6
	0.5	2.6
	1	5.5
	1.5	9
	2	12.1
3	0	0.6
	0.5	1.7
	1	3.5
	1.5	5.5
	2	7.6
4	0	06
	0.5	1.31
	1	2.5
	1.5	4
	2	5.7

Table 5: Insertion loss values depending on number of vias (left-with four switches) and switches (right-with four electrical vias)

At the end, the HFSS simulation depicted in Figure 20 shows a tunability with a great increase of the insertion loss due to the RF switches and their Ron of 17Ω. As seen in Table 6, the unloaded quality factor decreases significantly from 560 to 51 because the switches are lossy and the unloaded quality factor drops significantly. However, the tuning range using 0pF to 2pF capacitances is the same for the structures with and without the second level namely 10%. So, the addition of the second level has only an impact on the Q_0 but not the tuning range.

To prove this concept with measurements, wire-bonding will be made to make the low threshold voltage transistor work as RF switches since the OFF state is better (S_{21}=-19,3dB) and the mapping to connect those later with the DC pads are easier since the number of wire bonding will be lesser than with N-FET transistor with body biasing. On top of that, reducing the number of wires might prevent crossing them and a damageable grounding of the RF signal for the worst case.

	With the second level			Without the second level		
Value [pF]	f0(simu) [GHz]	IL [dB]	Q0 (simu)	f0(simu) [GHz]	IL [dB]	Q0 (simu)
0	2.34	-0.6	568	2.4	-0.6	580
0.5	2.28	-1.3	302	2.33	-0.65	555
1	2.22	-2.5	170	2.28	-0.7	511
1.5	2.17	-4	88	2.21	-0.91	416
2	2.11	-5.7	51	2.16	-1.12	302

Table 6: Comparison between simulated resonator with the second level and without (HFSS)

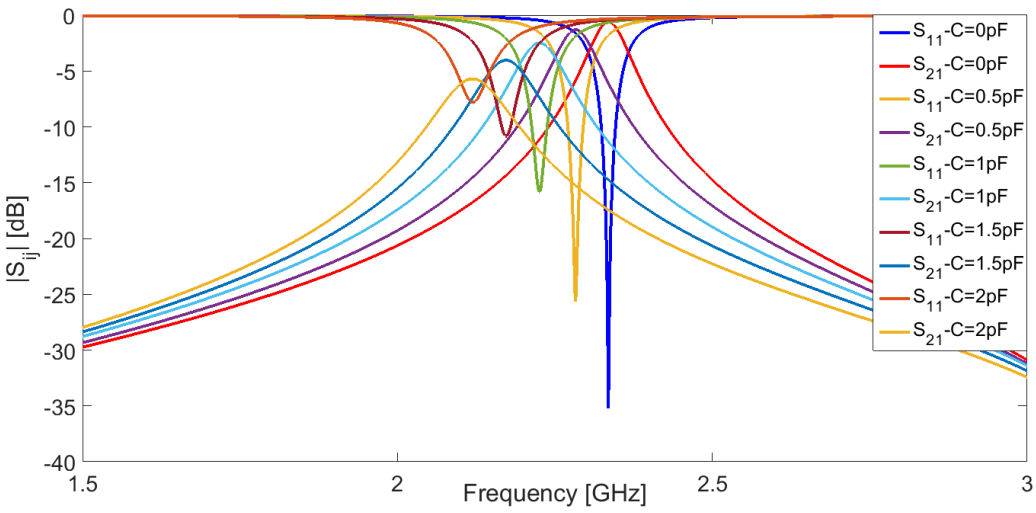

Figure 20: Simulation of the resonator with the second level

The Figure 21 depicts the final circuit with both resonator level (level 1) and tuning level (level 2) on which there are the RF switches connected to DC pads and therefore voltage supplies to control the gate-source voltage. A SMT capacitance of 1pF is set as well on the same level. Due to lack of time the whole system was measured with only one value of capacitance (1pF). However, as seen in Figure 22 there are two states ON and OFF. For V_{GS}=0V (OFF state) the resonance frequency is 2.32 GHz which is very close from the simulation results and a Q_0 of 536 ($Q_{0\text{-HFSS}}$=568). For the ON state, V_{GS}=3V, the f_0 is now of 2.26 GHz and a Q_0 of 121. The measured tuning is 5% which is the same as the simulation results. So it is very promising results because it makes us confident if we measure the whole circuit with SMT capacitance higher than 1pF.

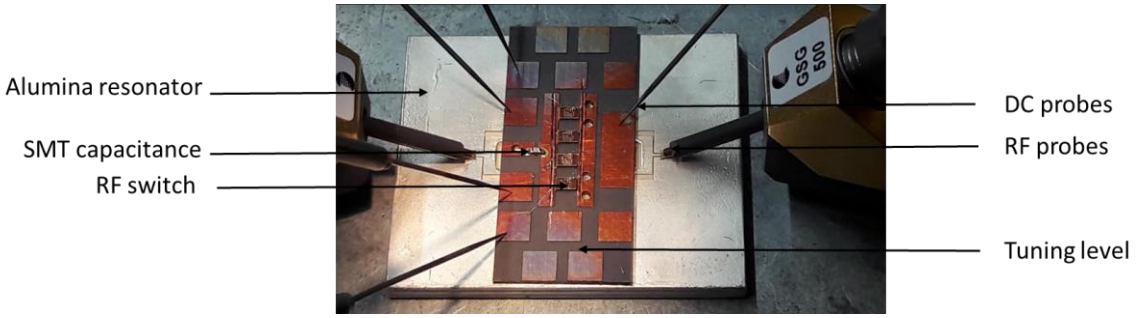

Figure 21: Controlled resonator with RF switches and Voltage supplies

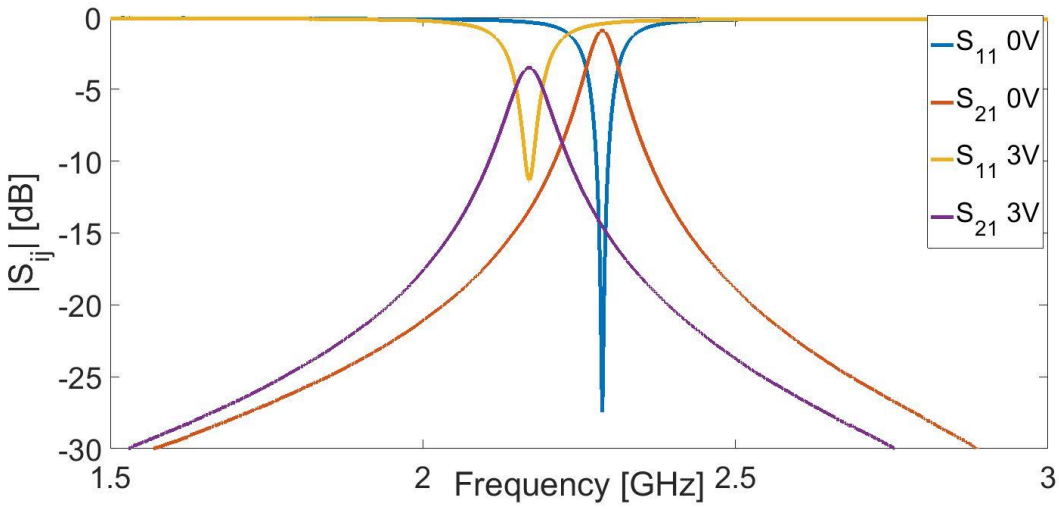

Figure 22: S parameters of the controlled resonator at 1 pF for two V_{GS} values

4.5 Conclusion

After a brief review of optical tunability methods, a little investigation of direct optical control has been made with the SIW resonator based on the metamaterial effect. Unfortunately, the photo sensitive material used has a relative permittivity difference between the dark and the illuminated state too low to observe a significant frequency shift for our application. Therefore the indirect control method has been explored.

Optically controlled RF switches based on the design in [7] with different characteristics (gate width, channel length and oxide thickness) were measured and an optimized configuration was found with insertion loss of 3.1dB for the ON state of four switches. In order to improve the S_{21} the option of body biasing was chosen since the current in the channel depends on the threshold voltage of the transistor. Unfortunately, the impact of this method is not significant enough and the insertion loss is the same as the low threshold voltage transistor: 1.35 dB for an applied voltage on the gate of 3V. Even though the ON state resistance is about 17Ω it is possible to simulate the concept of tunable filter with RF switches. Those results are for switches by applying a voltage to simulate the induced voltage of photodiodes since the photons cannot reach the silicon due to the silicide layer. As seen in Table 6 the tuning range is about 10% for a variation of capacitance from 0pF to 2pF for both structures (with and without the addition of the second level) in the simulation. The measurements with an 1pF capacitance confirm the good manufacturing and the concept of the whole structure since the measurements and simulation are very close each other with a 1pF capacitance. Other measurements need to be done with capacitance higher than 1pF in order to study more widely the tuning range and the evolution of the performance. The unloaded quality factor drops drastically to 51 with the use of those switches. Improving this feature means increasing the value of I_{DS} , SOI technology enables the channel length to be reduce. Therefore, the current is maximized and the insertion loss decrease at moderate costs. However, others solutions might be interested to study instead of using this technology. Indeed, it is possible to reduce the R_{ON} of switches by setting them in a parallel case in order to reduce the whole resistance and it is possible to imagine optimized layout with several integrated optical switches in a small area. But by doing that, the isolation could decrease, so it might be necessary to design a new chip with an enhanced configuration in order to find a good trade-off between, the size, the isolation and the $R_{ON.}$ Another feature could be added in

this compromise namely the power handling. Such an integrated system cannot handle a large amount of power since the size is a limiting factor, but it is built with CMOS elements which can handle power. So, at the end, this system could have a good power handling feature despite its size.

4.6 Bibliography

[1] B. Boyer, J. Haidar, A. Vilcot, and M. Bouthinon, “Tunable microwave load based on biased photoinduced plasma in silicon,” *IEEE Trans. Microw. Theory Tech.*, vol. 45, no. 8, pp. 1362–1367, Aug. 1997.

[2] Q. Chang, Q. Li, Z. Zhang, M. Qiu, T. Ye, and Y. Su, “A Tunable Broadband Photonic RF Phase Shifter Based on a Silicon Microring Resonator,” *IEEE Photonics Technol. Lett.*, vol. 21, no. 1, pp. 60–62, Jan. 2009.

[3] S. P. Chang, S. J. Chang, Y. Z. Chiou, C. Y. Lu, T. K. Lin, Y. C. Lin, C. F. Kuo, and H. M. Chang, “ZnO photoconductive sensors epitaxially grown on sapphire substrates,” *Sens. Actuators Phys.*, vol. 140, no. 1, pp. 60–64, Oct. 2007.

[4] B. Yuan, X. J. Zheng, Y. Q. Chen, B. Yang, and T. Zhang, “High photosensitivity and low dark current of photoconductive semiconductor switch based on ZnO single nanobelt,” *Solid-State Electron.*, vol. 55, no. 1, pp. 49–53, Jan. 2011.

[5] J. Sun, F.-J. Liu, H.-Q. Huang, J.-W. Zhao, Z.-F. Hu, X.-Q. Zhang, and Y.-S. Wang, “Fast response ultraviolet photoconductive detectors based on Ga-doped ZnO films grown by radio-frequency magnetron sputtering,” *Appl. Surf. Sci.*, vol. 257, no. 3, pp. 921–924, Nov. 2010.

[6] Z.-Q. Xu, H. Deng, J. Xie, Y. Li, and X.-T. Zu, “Ultraviolet photoconductive detector based on Al doped ZnO films prepared by sol–gel method,” *Appl. Surf. Sci.*, vol. 253, no. 2, pp. 476–479, Nov. 2006.

[7] J. M. Gonzalez, “Novel optically reconfigurable components for microwave applications,” Limoges, 2011.

[8] F. Dumas-Bouchiat, C. Champeaux, A. Catherinot, A. Crunteanu, and P. Blondy, “rf-microwave switches based on reversible semiconductor-metal transition of VO2 thin films synthesized by pulsed-laser deposition,” *Appl. Phys. Lett.*, vol. 91, no. 22, p. 223505, Nov. 2007.

[9] J. LEROY, “Caractéristiques électriques non-linéaires de la transition isolant-métal du dioxyde de vanadium (VO2) : Application à la conception de métamatériaux accordables dans le domaine térahertz,” thesis, Université de Limoges.

[10] A. M. Yurek, M. G. Li, C. D. Striffler, and C. H. Lee, “Modulation of millimeter-waves using diode laser illumination of a silicon waveguide,” *Int. J. Infrared Millim. Waves*, vol. 5, no. 10, pp. 1381–1388, Oct. 1984.

[11] M. Murata, T. Kitamura, and M. Geshiro, “Microstrip Filters with a Loaded Capacitance Containing a Light-Induced Plasma Region,” *IEEJ Trans. Electron. Inf. Syst.*, vol. 123, no. 3, pp. 397–400, 2003.

[12] O. Madelung, *Semiconductors: Data Handbook*. Springer Science & Business Media, 2004.

[13] J. M. Gonzalez, D. Baillargeat, N. Delhote, L. Roy, and S. McGarry, “Zero-bias optically controlled RF switch in 0.13 #x00B5;m CMOS technology,” in *Microwave Photonics, 2011 International Topical Meeting on Microwave Photonics Conference, 2011 Asia-Pacific, MWP/APMP*, 2011, pp. 441–444.

[14] F.-J. Huang and K. O, “A 0.5- mu;m CMOS T/R switch for 900-MHz wireless applications,” *IEEE J. Solid-State Circuits*, vol. 36, no. 3, pp. 486–492, Mar. 2001.

[15] K. Yamamoto, T. Heima, A. Furukawa, M. Ono, Y. Hashizume, H. Komurasaki, S. Maeda, H. Sato, and N. Kato, “A 2.4-GHz-band 1.8-V operation single-chip Si-CMOS T/R-MMIC front-end with a low insertion loss switch,” *IEEE J. Solid-State Circuits*, vol. 36, no. 8, pp. 1186–1197, Aug. 2001.

[16] IBM Technologies, “Design Kit and Technology Training CMOS8RF (CMRF8SF) V1700.” Oct-2010.

[17] A. S. Sedra and K. C. Smith, *Microelectronic Circuits*. Oxford University Press, 1998.

[18] T. Roy, A. F. Witulski, R. D. Schrimpf, M. L. Alles, and L. W. Massengill, “Single Event Mechanisms in 90 nm Triple-Well CMOS Devices,” *IEEE Trans. Nucl. Sci.*, vol. 55, no. 6, pp. 2948–2956, Dec. 2008.

[19] “RF SOI: Revolutionizing RF System Design | 2015-10-15 | Microwave Journal.” [Online]. Available: http://www.microwavejournal.com/articles/25255-rf-soi-revolutionizing-rf-system-design?v=preview. [Accessed: 30-Aug-2016].

[20] Gonzalez, J. M., Delhote, N., Baillargeat, D., McGarry, S.P. and Roy L. (2016), “Optically tunable filter based, on meshed CDS-polymer MIM capacitor”.Micrw.Opt.Technlo.Lett., 58:1926-1929

General conclusion

This thesis deals with the development of miniaturized modular optically tunable microwave components. Indeed, such a solution potentially simplifies the design, the realization and the complexity of tunable RF devices, because the control signal (optical) is uncorrelated with information signal (electromagnetic), removing the need for disruptive DC bias circuits in the RF parts compared to other tunable methods as seen in Chapter 1 such as: MEMS, Ferroelectric or magnetic materials.

A first resonator based on SIW technology combined with metamaterial effect has been in Chapter 2 to ensure a good performance and compactness. An interesting tuning range of 65% is reached, with added capacitances from 0pF to 5.6pF, with an unloaded quality factor of 116. With such features this structure has one of the best tradeoff between the size and the tuning range in the literature with the use of surface mounted capacitances. An added tuning level with a SMT capacitance was investigated to predict the impact of the second "floor" on the whole performances. Thanks to a suitable sealing process for our frequency band applications (S and L) the effects on the unloaded quality factor and the tuning range are very low. Based on these results, a "LEGO" like structure can be imagined and others levels with their own purpose can be added to form a compact, stacked, tunable and reconfigurable system. On top of that, it might be very interesting to think about designing a dual mode SIW resonator based on the previous metamaterial to create a new type of very compact SIW resonator.

However, in order to foresee the use of lossy RF switches, a new structure with higher Q_0 is designed and measured in the Chapter 3. Thanks to the cavity loading technique, a new Alumina based resonator manufactured with SLA (Stereolithogaphy) process is created with an interesting Q_0 of 600 for the OFF state and a tuning range of 29% (with added capacitances from 0pF to 7pF). By optimizing the effect of the capacitive post the whole size of this passive device was reduced by 34% to obtain at the end a compact resonator with a Q_0 of 303 with a respectively tuning range of 15% (with added capacitances from 0pF to 1.5pF), the tuning range increases up to 24% with a SMT capacitance of 4pF but the insertion loss are too high (>13 dB). The new comprise between Q_0 and the volume in terms of λ_g is one of the best compared with structures from literature. The reduction factor could be enhanced by increasing the height of the post. Based on this new elementary cell, higher order filters were investigated. Then a second order tunable filter has been designed with a simulated tuning

range of 15% and a variation of the bandwidth from 370MHz to 170MHz. A third order and fourth order filter with a BW of 1.3GHz and 0.75 GHz respectively have been simulated on HFSS. In spite of their simple topology, the inter resonator coupling of such high order filters becomes more complex and need a sustained design and optimized procedure

Chapter 4 is focused on optical tunability with direct and indirect control. The first category is depicted with photosensitive materials such as Cadmium Sulfide, Zinc oxide and Nano-cristallyne Silicon loaded polymer. An attempt is made by simulating the first material with the SIW based resonator previously created to shift the resonant frequency of the structure. However, since the change of the relative permittivity is too low (from 4 to 4.6) between the illuminated and the dark state the shift of f_0 is not significant enough four our application. Codevelopment of such materials can still be made to improve their properties. For example, for the nano-crystalline silicon, a higher doping in nano-particle might result in an increase of the relative permittivity. The main interest of optical control is that no conversion of the light signal is needed as the optically tunable part is directly included in the circuit.

The second part of the Chapter 4 is devoted to indirect control. The advantage of this method is that the control circuit and the electromagnetic one can be optimized separately, but the optical signal needs to be converted into a bias, using a photodiode in our case. This photosensitive device connected to the gate of the transistor and provides a low/high impedance path between drain and source by bringing the gate source voltage V_{GS} above or below the threshold voltage V_t. The technology chosen for this work has been the well-established commercially available 0.13µm CMOS process from IBM. Based on the work of J.M Gonzales, optically controlled RF switches have been measured to find an optimized configuration. The one with the highest value of the parallel plate capacitance between the gate and the channel has the best insertion loss of 3.1dB. A method called body biasing is used to improve this feature and reduces the resistance of the channel at the ON state. Unfortunately, the insertion loss does not improve significantly and are the same as the low threshold voltage configuration. But a concept of tunable resonator with those RF switches (implemented in the second level) with an ON state equivalent resistance of 17Ω has been simulated. The tuning range from 0pF to 2pF is the same as the resonator without this second "floor". The addition of the tuning system impacts only the unloaded quality factor which

drops from 580 to 51 in simulation. However, a measurement was made with capacitance of 1pF. The results are very close from the simulation and they are very promising because there is a significant difference between the ON and the OFF mode which is ,of course, relevant for a tunable element. Due to lack of time the system has not been measured with capacitance higher than 1pF but the previous conclusion makes us very confident about the close match between HFSS and the reality (for C>1pF). The insertion loss of such RF switches can be enhanced with the use of SOI manufacturing process in order to shrink the length of the channel and therefore maximize the drain source current. On top of that, with this technology, it is possible to create capacitor banks which will be useful to miniaturize the tuning pat of the system.

This thesis work has been focused on optical tunability of RF components in a stacked system composed of two specific levels: one for the elementary cell (resonators) and another for the tuning devices. But with the use of direct/indirect control we can imagine redesigning the whole system horizontally i.e. with the resonator and the optical tuning elements at the same level. For instance with the alumina based resonator, the RF switches can be reported on its top surface at dedicated positions. Of course we need to redesign the whole structure to avoid electrical problems such as bad ground connection, impedance matching, etc... Another idea to miniaturize the whole system is to integrate it in a structure where optical signal can be guided and optical source can be integrated. A technology proposed by IBM allows the manufacturing of a low loss and low cost silicon optical waveguide. So with the use of the proper elements for guiding light within this silicon guides for the actuation of the optical RF switches, an embedded miniaturized tunable filter with optical control can be thought. Of course the optical method needs more maturity to compete with current tunability methods such as MEMS and needs to be full characterized by quantifying the influence of the wavelength on the photodiodes with different optical sources (Broadband lamp, 650nm, 440nm laser and so on) and the needed power to activate the photodiode.

Abstract:

Researchers have demonstrated over the last decade the importance of tunability to reduce the complexity and the cost of telecommunication systems operating at multiple frequency bands and standards.

This work focuses on novel optically tunable filters for microwave applications and therefore proposes alternative solution to commonly used tuning methods such as MEMS or diodes. The thesis has investigated different resonators for having good candidates for the novel optically tunable system developed throughout this manuscript. Different technologies are used to design such components, namely: Substrate Integrated Waveguide (SIW) technology combined with metamaterial effect and cavity loading. All manufactured resonators are designed to be balanced between three features: the unloaded quality factor (Q_0), the tuning range (TR) and the size. The last part deals with the tuning system based on SMT capacitance and optically controlled RF switches based on Si CMOS technology. Several methods have been used to improve the insertion loss of manufactured switches and therefore the performance of the whole system, demonstrating the feasibility of this novel optically based tunable concept.

Keywords: [SIW, metamaterial, loaded cavity, optical switches, tuning range, High quality factor]

Résumé:

Au cours de ces dernières années, les chercheurs ont démontré l'importance de l'accordabilité dans les systèmes de télécommunications fonctionnant pour des multiples bandes de fréquences, afin de réduire leur complexité et leur coût.

Ce travail se focalise sur des filtres innovants accordables optiquement et propose ainsi une solution alternative aux méthodes plus classiques comme les MEMS ou les diodes. Cette thèse retrace la conception de trois résonateurs pouvant être de bons candidats à intégrer dans le système accordable optiquement développé au travers du manuscrit. Ces éléments sont conçus par le biais de différentes technologies comme : la technologie « Substrate Integrated Waveguide » combinée avec un effet dit métamatériau et la méthode de cavité chargée par un plot capacitif. Tous ces résonateurs ont été créés dans le but d'avoir des performances intéressantes pour trois critères : le facteur de qualité à vide (Q0), la plage d'accord (TR) et la taille. La dernière partie, quant à elle, se consacre au système d'accordabilité basé sur l'utilisation de capacité CMS et de switches RF contrôlés optiquement et fabriqués à l'aide de la technologie silicium CMOS. Plusieurs méthodes ont été utilisées afin d'améliorer les pertes d'insertion des switches RF et par conséquent les performances du système global, démontrant la faisabilité de ce concept innovant accordable optiquement.

Mots clés: [SIW, métamatériau, cavité chargée, switches optiques, plage d'accord, fort facteur de qualité]